Crystalline Phase-Change Materials:

Disorder, Medium-Range Order and Electrical Switching

Von der Fakultät für Mathematik, Informatik und Naturwissenschaften der RWTH Aachen University zur Erlangung des akademischen Grades eines Doktors der Naturwissenschaften genehmigte Dissertation

vorgelegt von

Diplom-Physiker

Philipp Johannes Merkelbach

aus Köln

Berichter: Universitätsprofessor Dr. Matthias Wuttig,
Prof. Dr. Theo Siegrist

Tag der mündlichen Prüfung: 25.11.2011

Diese Dissertation ist auf den Internetseiten der Hochschulbibliothek online verfügbar.

Contents

1. Introduction 1
   1.1. Phase-Change Materials 2
   1.2. Resonant bonding in crystalline Phase-Change materials 5
   1.3. Treasure Map of Phase-Change materials 8
   1.4. Crystal Structure and Disorder in Phase-Change Materials 12

2. Disorder Induced Localization 17
   2.1. Resistivity of solids 18
   2.2. Metal-Insulator Transition 19
      2.2.1. Ioffe-Regel condition 19
      2.2.2. Types of Metal-Insulator Transition 20
      2.2.3. Energy scales of MIT transitions 21
   2.3. Temperature dependance of the Resistivity in GeTe and $GeSb_2Te_4$ 24
   2.4. Low temperature measurements of $GeSb_2Te_4$ 28
   2.5. X-ray diffraction analysis of the MIT 31
   2.6. Transport parameter of GeTe and $GeSb_2Te_4$ 38
   2.7. Conclusions 48

3. Crystallographic Analysis of Disorder 49
   3.1. Neutron Pair Distribution Function technique 49
      3.1.1. Diffraction by disordered systems 50
      3.1.2. Pair distribution function 55
   3.2. Beamline D4 at Institut Laue-Langevin, Grenoble 57
      3.2.1. Sample geometry, data treatment, and data analysis 58
   3.3. Modeling of the short to medium range order in phase-change materials . . . 63

3.4. Structure of GeTe 65
3.5. Comparison of the structure of GeTe and $GeSb_2Te_4$ 68
3.6. Structure of $GeSb_2Te_4$ 71
3.6.1. Rhombohedral model for $GeSb_2Te_4$ 71
3.6.2. Displacement model from DFT calculations 72
3.7. Annealing effects on structure of $GeSb_2Te_4$ 78
3.8. Summary of Crystallographic Analysis of Disorder 81

4. Electrical Switching in Phase-Change Materials 83
4.1. Working principle of phase-change memory 84
4.2. Disorder encoded multi-level storage in phase-change memory 87
4.3. Phase-change memory cell preparation 88
4.4. Pulsed Electrical Tester 92
4.5. Electrical switching in GeTe 92
4.6. Summary of electrical switching in phase-change materials 98

5. Summary and Outlook 99

Appendix 102

A. New stoichiometric frontiers 103

B. Additional Plots 109

List of Figures

1.1. Property contrast between amorphous and crystalline phase of a covalent bonded material and a phase-change material. 4
1.2. Infrared reflectance spectra of Ge_2SbTe_4 film. 6
1.3. Resonant bonding in GeTe. 7
1.4. Resonant bonding vs. distortion. 9
1.5. Treasure map for phase-change materials. 11
1.6. EXAFS data of $GeSb_2Te_4$ measured at different temperatures. 15
1.7. EXAFS data of GeTe: amorphous vs. crystalline. 15
1.8. EXAFS data of $GeSb_2Te_4$: amorphous vs. crystalline. 16

2.1. Classification of metal and insulator. 18
2.2. Comparison of two metal-insulator transition concepts: Mott and Anderson. 23
2.3. Temperature dependent sheet resistance of GeTe and $GeSb_2Te_4$. 25
2.4. Effect of annealing on the resistivity and its temperature dependance for different GeSbTe alloys. 27
2.5. Low temperature resistivity of different annealed crystalline $GeSb_2Te_4$ films. . 29
2.6. Variable range hopping model fitted to $GeSb_2Te_4$. 30
2.7. Transport parameters of VO_2 as a function of temperature. 32
2.8. X-ray diffraction pattern of GeTe and $GeSb_2Te_4$. 33
2.9. Ge segregation in the grain boundaries of GeTe. 35
2.10. Changes of the FWHM of GeTe and $GeSb_2Te_4$ on annealing. 37
2.11. Summary of the transport parameters of GeTe and $GeSb_2Te_4$. 40
2.12. The Mott criterion applied to $GeSb_2Te_4$. 43
2.13. Disorder induced localization: Energy scales and Density of states. 44

2.14. Schematic presentation of the unique crystal structure and bonding situation in $GeSb_2Te_4$. 47

3.1. Differential scattering cross section per atom for a monoatomic system. . . . 55
3.2. Examples of real-space functions. 56
3.3. Instrument D4 at Institut Laue-Langevin. 59
3.4. Total structure factor and pair-distribution function of crystalline GeTe and $GeSb_2Te_4$. 61
3.5. Evolution of the pair distribution function G(r) with increasing q_{max}. 62
3.6. Effects of rhombohedral distortion and atomic displacement on the pair distribution function G(r). 64
3.7. Structure of GeTe. 66
3.8. Fit of a rhombohedral model to the total pair-distribution function of GeTe (range 2.5 - 20.5 Å). 67
3.9. GeTe: Short to medium range order PDF 68
3.10. Total pair disotributiuon function G(r) of GeTe and $GeSb_2Te_4$. 69
3.11. Comparison of the short to medium range order of GeTe and $GeSb_2Te_4$. . . . 70
3.12. Rhombohedral fit of the pair-distribution function G(r) for r = 2.5 - 20.7 Å for crystalline $GeSb_2Te_4$ annealed at 150 °C. 72
3.13. Comparison between the short to medium range order and the long range order in crystalline $GeSb_2Te_4$ annealed at 150°C. 73
3.14. Comparison of DFT data with the experimental data. 76
3.15. Displacement pattern in $GeSb_2Te_4$ calculated by DFT. 77
3.16. Annealing effect on short to medium range order Pair Distribution Function of $GeSb_2Te_4$. 79
3.17. Neutron PDF fit parameters of $GeSb_2Te_4$ on annealing. 80

4.1. Working principle of a PCRAM cell. 85
4.2. Threshold switch in $Ge_2Sb_2Te_5$. 86
4.3. Enabling multi-level PCRAM cells with a new approach. 88
4.4. PCRAM base wafer and single cell. 89
4.5. AFM image of the bottom electrode of a PCRAM cell. 91
4.6. SET window for switching GeTe. 93

4.7. Cell resistance after application of SET pulses with different amplitude and length. 94
4.8. Change of SET speed with initial RESET resistance. 97

A.1. Temperature dependent sheet resistance of different co-sputtered GeTe-Sb_2Te_3 samples. 104
A.2. X-ray diffractogramm of a co-sputterd GeTe-Sb_2Te_3 sample. 105
A.3. FT-IR spectra of a co-sputterd GeTe-Sb_2Te_3 sample 106

B.1. Resistivity at low temperatures of $GeSb_2Te_4$ samples annealed around the MIT.109
B.2. Comparison of the Neutron PDF data with the number of neighbors. 110

List of Tables

2.1. Transport parameter of GeTe and $GeSb_2Te_4$. 41

3.1. Fit parameters for a rhombohedral GeTe model. 67
3.2. Fit parameters for rhombohedral $GeSb_2Te_4$ model. 74
3.3. Linear fit parameters for annealing dependence of $GeSb_2Te_4$. 81

CHAPTER 1

Introduction

The methods of conveying and storing information are linked to the progression of human knowledge. From stone inscriptions and papyri to handwritten books, from cablegrams to the cloud, humans have always been on the lookout for innovative techniques to transfer and preserve knowledge, as such techniques are likely to open new paths into the pursuit of knowledge and understanding.

In the past decades the way of accessing information has changed drastically. To give an example, let me take you to the dining table at my parents' house. Fifteen years ago during our discussions, we would regularly have to check with the Brockhaus Encyclopedia. This changed with the wider distribution of laptops, probably around the year 2002. Instead of going to the bookshelf it was now faster to grab the laptop from behind, and instead of an Encyclopedia came Wikipedia[1]. Nowadays, we are no longer limited to the dining table - we just take a multi touch smart phone. The source of information is readily accessible at our fingertips wherever we are due to fast internet access via the cellular network.

This development is even accelerated by the availability of cloud based services [1] and synchronization via the cloud. People get used to having their documents, music and photos available wherever they are and on every device they own. This demands more and more data storage capacity both in the mobile devices and the cloud. The development of new data storage concepts with higher data densities and lower power consumption remains essential. Especially the development of fast non-volatile memories is important. A memory combining the speed of DRAM and the non-volatility of FLASH would simplify the daily

[1] http://www.wikipedia.org

usage of computers, while at the same time reduce the power consumption of them. With a non-volatile DRAM replacement the procedure of powering up the computer in the morning would take only a few seconds, as it is not necessary to write the information back to the DRAM. Nowadays the information stored in the DRAM has to be constantly refreshed, as DRAM can store information only on a µs time scale. This, of course, consumes energy even in idle. This technology could replace both FLASH and DRAM chips in mobile devices and allow for smaller sizes and longer battery time. One likely candidate to meet these requirements is Phase-Change Random Access Memory (PCRAM)[2]. In phase-change materials the optical and electrical property contrast of the crystalline and the amorphous phase is used to store information. This study analyzes aspects of phase-change materials that are of interest both scientifically and commercially. In this study the focus lies on the crystalline phase of phase-change materials. The crystalline phase has an exceptional high degree of disorder and is characterized by a unique bonding mechanism, resonant bonding. The degree of disorder in the crystalline phase is comparable with the degree of disorder found in amorphous metals. As the resistivity of crystalline phase will be analyzed, it will be shown that the conduction mechanism is governed by disorder. Especially the annealing dependency of the resistivity can be correlated to a disorder induced localization of the charge carriers. As disorder plays a decisive role for the resistivity, the structural properties of crystalline phase-change materials and distortions in the short to medium range order are studied in detail. To analyze the degree of disorder neutron pair distribution measurements of crystalline phase change materials will be analyzed and discussed. To round this up and give a more device oriented perspective, ideas for future generation phase-change memory technologies based on disorder induced localization will be presented. Along with this, the preparation and characterization of current state-of-the-art phase change memory cells is investigated. In this phase-change memory characterization, the limits of the switching speed are tested.

1.1. Phase-Change Materials

Phase-change materials are a class of materials with a unique portfolio of properties [3]. At ambient temperatures, they are stable in both the crystalline and the amorphous phase. However, if a suitable temperature profile is applied, phase-change materials can be switched reversibly between the two phases. There is a pronounced contrast between the properties of the two phases, both for the optical reflectivity and the electrical resistivity. This

contrast makes it possible to use phase-change materials as a means for non-volatile data storage. Concepts employing phase-change materials as optical non-volatile, rewritable memory in a commercially available product date back to the early 1990s [2], in particular the PCR with 500 MB storage capacity. The development has progressed via the rewritable CD (650 MB) and the rewritable DVD (9,4 GB) to the rewritable BluRay XL with 100 GB capacity, which Panasonic have announced recently [4]. The contrast in electrical resistivity can be used in non-volatile electrical data storage devices like PCRAM (Phase-Change Random Access Memory). The unique combination of both speed and non-volatility with a high storage density makes PCRAM a competitor for both Flash and DRAM.

Figure 1.1 contrasts the properties of a phase-change material such as GeTe with an ordinary covalent bonded material like SiO_2. For both materials, an amorphous and a crystalline phase exist at room-temperature, as the diffraction patterns in the top part of figure 1.1 show. The crystalline phase shows sharp Bragg reflexes corresponding to the existence of a long range order, whereas the amorphous phase has no sharp reflexes. The amorphous phase lacks long range order but has a rather well-defined local atomic arrangement. In figure 1.1, one can see no difference in physical appearance between the amorphous and the crystalline SiO_2 samples (fig. 1.1 (c)). In contrast, one can easily see a difference in reflectivity between the written amorphous part in the center and the unwritten crystalline part in the outer region of the phase-change material in the DVD-RAM (fig. 1.1 (d)). The measurement of the optical transmission for SiO_2 and the reflectivity for GeTe shown in figure 1.1 (e) and (f) support this observation. For SiO_2, the transmission in the visible spectra is the same for the amorphous and the crystalline sample, whereas GeTe shows an increase of reflectivity of 50 % on crystallization.

The outcome of these simple comparisons demonstrates that phase-change materials, unlike ordinary covalently bonded materials, change their properties on crystallization. Why GeTe and SiO_2 behave in such a different way needs further examination and explanation. In systems like SiO_2, the local structure of the amorphous and the crystalline phase do not change significantly. Studies using EXAFS (Extended X-ray Absorption Fine Structure) have demonstrated that with phase-change materials the local structures of the amorphous and the crystalline phase are quite different [5]. Ab initio calculations reproduce this change upon amorphization [6].

The different local atomic arrangements cause the optical contrast observed in phase-change materials. The physical origin of this contrast, however, is not evident. Fermi's golden

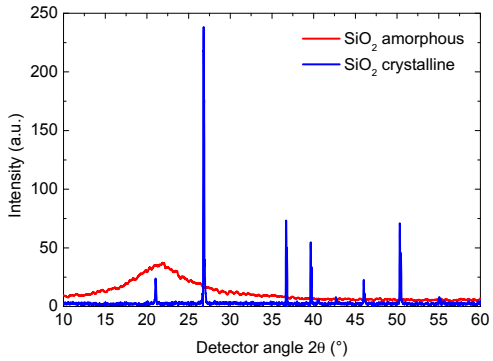

(a) X-ray diffraction pattern of SiO_2, amorphous and crystalline.

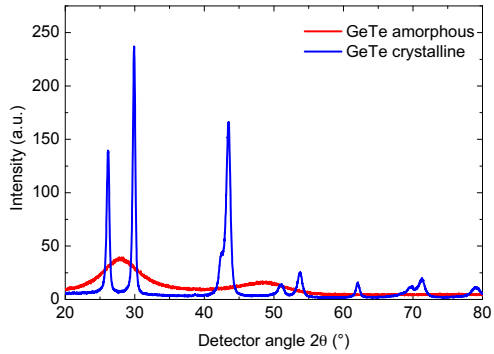

(b) X-ray diffraction pattern of GeTe, amorphous and crystalline.

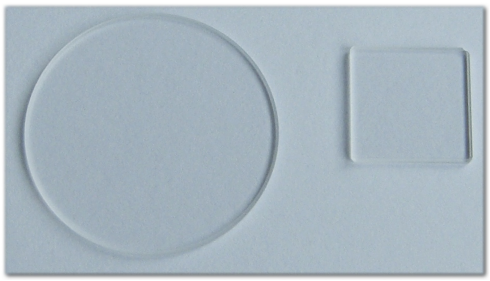

(c) Picture of SiO_2, amorphous and crystalline. There is no visible difference except for the shape. (the right one is crystalline)

(d) Picture of a DVD-RAM (picture taken by Dominic Lencer). The reflectivity contrast between the written (inner) and unwritten (crystalline) regions is obvious.

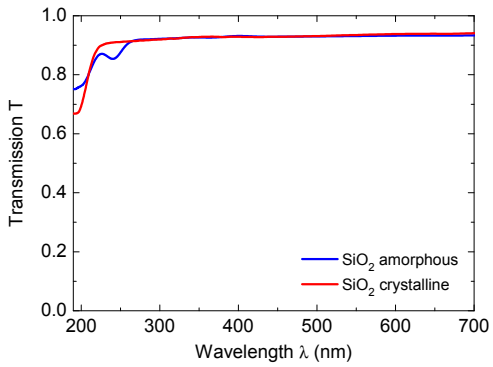

(e) Transmission of SiO_2, amorphous and crystalline.

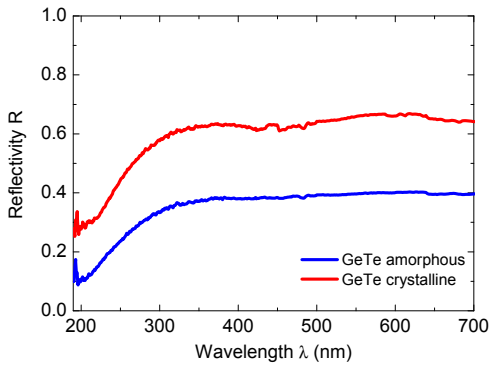

(f) Reflectivity of GeTe, amorphous and crystalline.

Figure 1.1.: Property contrast between amorphous and crystalline phase of a covalent bonded material and a phase-change material. For both SiO_2 and GeTe, an amorphous and a crystalline phase can be prepared, as can be seen by the x-ray diffraction patterns of SiO_2 (a) and GeTe (b). No difference between the amorphous and the crystalline SiO_2 can be seen in (c), while one can clearly distinguish between the amorphous and crystalline parts in the picture of the DVD (d). The observation of (c,d) is supported by the measurements of optical transmission and reflectivity for SiO_2 and GeTe (e,f), respectively.

rule gives a quantum mechanical picture of the probability of an optical transition. It states that a change in the joint density of states (JDOS) or in the transition matrix elements can cause a difference in the transition rate. Wełnic *et al.* [7] have shown that in phase-change materials a difference in transition matrix element is dominant for the optical contrast between the amorphous and the crystalline phase.

1.2. Resonant bonding in crystalline Phase-Change materials

Measurements of the reflectivity in the infrared to visible spectra of light were another key advance in the understanding of the characteristics of phase-change materials and the subsequent identification of design rules for phase-change materials. These measurements allowed the identification of a unique bonding mechanism, which is characterized by an extraordinary increase in electronic polarizability on crystallization [8]. Fourier transformed infrared spectroscopy (FTIR) has been performed on thin films of phase-change materials deposited on a metallic mirror. Figure 1.2 shows a measurement for Ge_2SbTe_4. The special sample design leads to interferences between the reflected light from the phase-change film and the reflected light from the metallic mirror. These interferences depend on the optical path. The distance of the minima is therefore inversely proportional to the product of the film thickness t and the refractive index n of the phase-change film. For the crystalline sample, the contribution of the free Drude electrons to the spectra is visible at low photon energies. The interference maxima are smaller in the crystalline phase due to subgap absorption in the crystalline phase. The most important difference in the spectra is the fact that the spacing of the interference minima is about 40 %. As the lowering in film thickness on crystallization of about 6 % would enlarge the spacing even more, the refractive index is about 50 % larger in the crystalline phase. The concomitant lowering of band gap on crystallization is as well visible in the data. For Photon energies larger than the band gap the oszillations strongly decrease.

The Clausius-Mossotti model [9] can calculate the optical dielectric constant of a compound from the atomic weights m_i and density n_i by assigning a polarizability α_i to each element. The optical dielectric constant can be calculated in this model from

$$\frac{\epsilon_\infty - 1}{\epsilon_\infty + 2} = \frac{\rho}{3\,\epsilon_0\,\sum_i n_i m_i} \sum_j n_j a_j \tag{1.1}$$

with the density ρ and the permeability of free space ϵ_0.

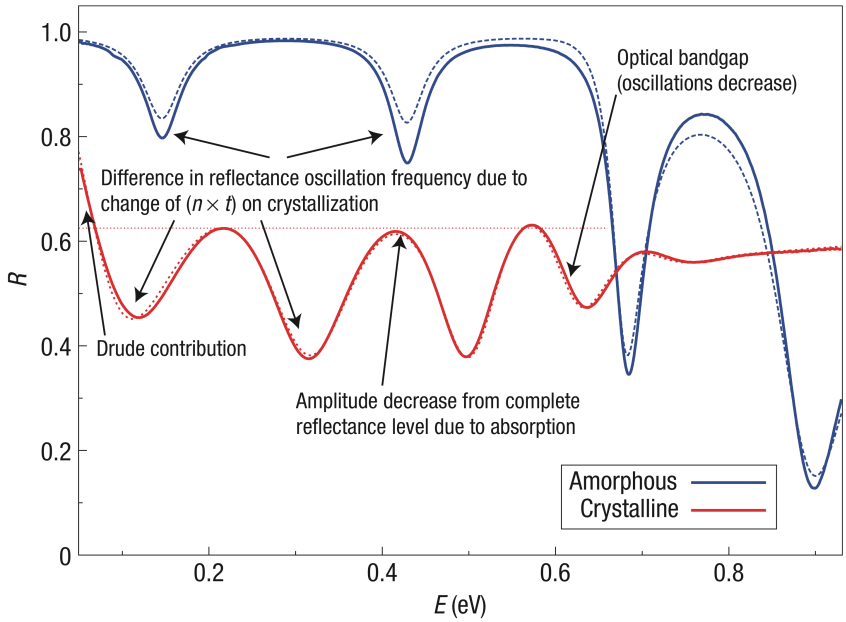

Figure 1.2.: Infrared reflectance spectra of Ge_2SbTe_4 film. The experimental data are shown in solid lines, whereas the dashed lines denote the simulation results. On crystallization, the thickness decreased from 0.53 to 0.50 μm. Arrows mark the contributions of different phase-change film properties to the reflectance curve [8].

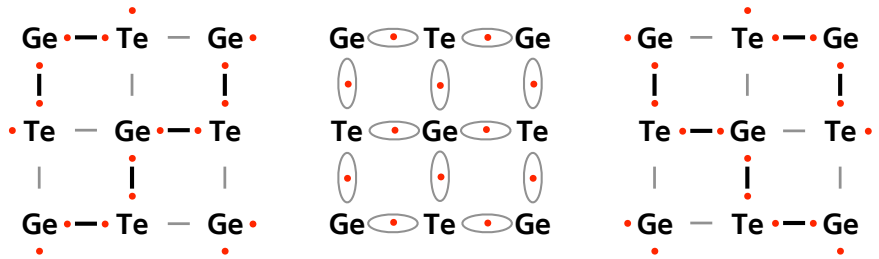

Figure 1.3.: Resonant bonding in GeTe. Two dimensional cut through the NaCl-like GeTe structure. On average, 3 p-electrons are available in the valence band of GeTe. Thus the material has two different configurations to form covalent bonds, depicted left and right. However, GeTe can lower its energy by forming a hybrid wavefunction, shown in the center pattern. This bonding mechanism, called resonant bonding, is responsible for the high electronic polarizability observed in crystalline phase-change materials.

The optical dielectric constant ϵ_∞ of the amorphous phase is in good agreement with the Clausius-Mossotti model, while it is off by about 30 % for the crystalline phase. This increase in polarizability can be attributed to a change in bonding configuration. Phase-change materials such as GeTe or $GeSb_2Te_4$ crystallize in a NaCl-like structure. The bonding is based on directional p-type bonds. As GeTe has 3 p-electrons in the valence band on average, two bonding configurations for covalent bonds would be possible. This situation is depicted in figure 1.3, left and right pattern. Chains of bonds form in both configurations. However, GeTe can minimize its energy by forming a hybrid wave function. This special bonding is described as resonant bonding. It is shown in the center pattern of figure 1.3. Each bond is occupied by only one electron on average, which leads to the observed high electronic polarizability. This unique bonding mechanism has been found to be a key characteristic of crystalline phase-change materials. The resonant bonding leads to a ordering and alignment of p orbitals on neighboring atomic sites [10]. This alignment has a strong effect on the optical matrix elements, which were previously identified to be responsible for the optical contrast [7]. Therefore, the alignment and ordering of the p orbitals caused by resonant bonding leads to an enhanced ϵ_∞. In the amorphous state, the lack of long range order impedes the formation of resonant bonds [10].

1.3. Treasure Map of Phase-Change materials

Since research on phase-change materials began, design rules have stimulated the field. Phase-change materials typically contain chalcogens, in particular Te, or pnicogens such as Sb, for example GeTe, $GeSb_2Te_4$, $Ge_2Sb_2Te_5$, and doped Sb or Sb_2Te. In 1991, Yamada *et al.* [11] identified numerous phase-change materials along the pseudo-binary line spanning from GeTe to Sb_2Te_3. These materials have since proved to be a rich playground for further discoveries. Once Shportko *et al.* [8] had identified resonant bonding as a fingerprint for phase-change materials, Lencer *et al.* [12] were able to derive a treasure map for phase-change materials by looking into the conditions needed for resonant bonding.

Prior to identification of resonant bonding it was already known that a characteristic of phase-change materials is an octahedral-like atomic arrangement in the crystalline state. The average number of s- and p-electrons per atom N_{sp} was identified as a measure to separate octahedral from tetrahedral atomic arrangement. Materials with values for N_{sp} well above four were identified as octahedrally coordinated [13]. In contrast tetrahedral semiconductors like Si, Ge, GaAs, GaN or $CuInS_2$ only have an N_{sp} value of four. This N_{sp} value makes sp^3-hybridization energetically favorable, leading to tetrahedral coordination[2]. For phase-change materials with more than four valence electrons, a hypothetic tetrahedral arrangement would lead to an occupation of anti-bonding sp^3-states, which is energetically unfavorable. Therefore bonding via p-states is dominant and leads to an octahedral-like atomic arrangement.

Most phase-change materials have three p-electrons per atom on average. The materials of the pseudo-binary-line between GeTe and Sb_2Te_3 crystallize in a meta-stable NaCl-like structure, with Te occupying one sublattice (anion site) and Ge/Sb and vacancies occupying the other sublattice (cation site). The number of vacancies per unit cell has to be taken into account when calculating the average number of p-electrons, thus the calculated average number of electrons is an average per atomic site. $GeSb_2Te_4$, for example, has four Tellurium atoms, two Antimony atoms, one Germanium atom, and one vacancy, thus $GeSb_2Te_4$ has on average three p-electrons; $(4 \cdot 4 + 2 \cdot 3 + 1 \cdot 2 + 1 \cdot 0)/8 = 3$. This calculation holds for all materials on the pseudo-binary line.

Figure 1.4 shows one possible route to endanger resonant bonding. The distortion for

[2] Note that the underlying concept of averaging breaks down if the atomic species are to different, that is for example CsCl, which has an N_{sp} of 4 but crystallizes in a cubic structure.dis

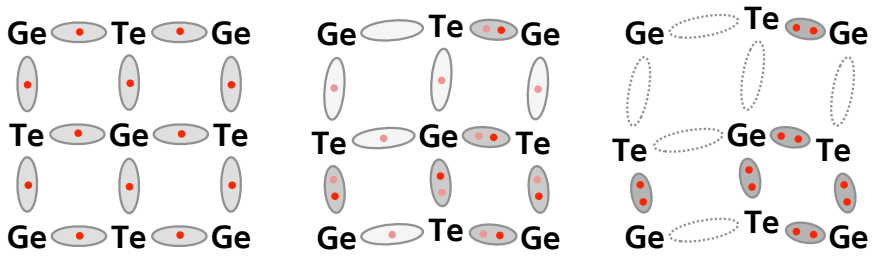

Figure 1.4.: Resonant bonding vs. distortion. An increase in distortion leads to a reduction of resonant bonding and consequently to a reduction of ϵ_∞

GeTe increases from left to right. As an undistorted case with perfect resonant bonding is gradually impaired by distortions, a splitting into three short and three long bonds occurs (in this 2-dimensional cut, only a 2+2 splitting can be seen). The splitting leads to a saturated p-type covalent bond of the valence electrons in the three short bonds. As a consequence, the high electronic polarizability of the resonant bonds is reduced. This splitting occurs especially if the system shows a tendency for hybridization of the bonds [14]. In addition, a strong degree of ionicity also leads to a reduced polarizability of the electrons around the cation site. The system therefore needs a combination of small hybridization and small ionicity to form resonant bonds.

As many phase-change materials have three p-electrons on average, they resemble the electron configuration of IV-VI compounds with equal amounts of anions and cations, like GeTe, GeS, GeSe or SnTe. Elements of group V have also three p-electrons. The structure and bonding of these materials has been studied in the past. A diagram well-suited to classify the bonding and the structure of these materials was proposed by Littlewood [15, 16]. He was able to draw a simple structure map that can predict the bonding type and therefore the crystal structure of a given stoichiometry by introducing two coordinates r'_σ and r_π^{-1}. The coordinates are defined as

$$r'_\sigma = r_p^A - r_p^B \tag{1.2}$$

$$r_\pi^{-1} = \left[\left(r_p^A - r_s^A\right) + \left(r_p^B - r_s^B\right)\right]^{-1}. \tag{1.3}$$

The valence radii of the s- and p-orbital are represented by r_s and r_p for atom A and B. These two coordinates provide a measure for the degree of ionicity (r'_σ) and the covalency (r_π^{-1}). Many phase-change materials are ternary or even quaternary alloys. So the coordinates

proposed by Littlewood [15] had to be generalized for alloys containing more than two elements. To this end, Lencer *et al.* [12] calculated an equivalent binary alloy for the ternary or quaternary alloys. This is done by calculating the stoichiometric average values for the anion and cation sites, respectively. For a material like $GeSb_2Te_4$, the anion site is simply Te, whereas for the cation site one Ge- and two Sb-atoms have to be averaged. The coordinates are calculated by weighting the corresponding orbital radii with the number of atoms n_i of the species i per formula unit. The average coordinates r'_σ and r_π^{-1} are defined as follows:

$$r'_\sigma = \underbrace{\left(\frac{\sum_i n_i r_{p,i}}{\sum_i n_i}\right)}_{\text{Anions}} - \underbrace{\left(\frac{\sum_j n_j r_{p,j}}{\sum_j n_j}\right)}_{\text{Cations}} \tag{1.4}$$

$$r'_\pi = \left\{\underbrace{\left(\frac{\sum_i n_i (r_{p,i} - r_{s,i})}{\sum_i n_i}\right)}_{\text{Anions}} + \underbrace{\left(\frac{\sum_j n_j (r_{p,j} - r_{s,j})}{\sum_j n_j}\right)}_{\text{Cations}}\right\}^{-1} \tag{1.5}$$

With these coordinates it was possible to draw the treasure map for phase-change materials shown in figure 1.5. Phase-change materials all lie in the region of small hybridization and small ionicity, as was to be expected from the deliberations above. Oxides, sulfides, selenides and tellurides are in close proximity within their group.

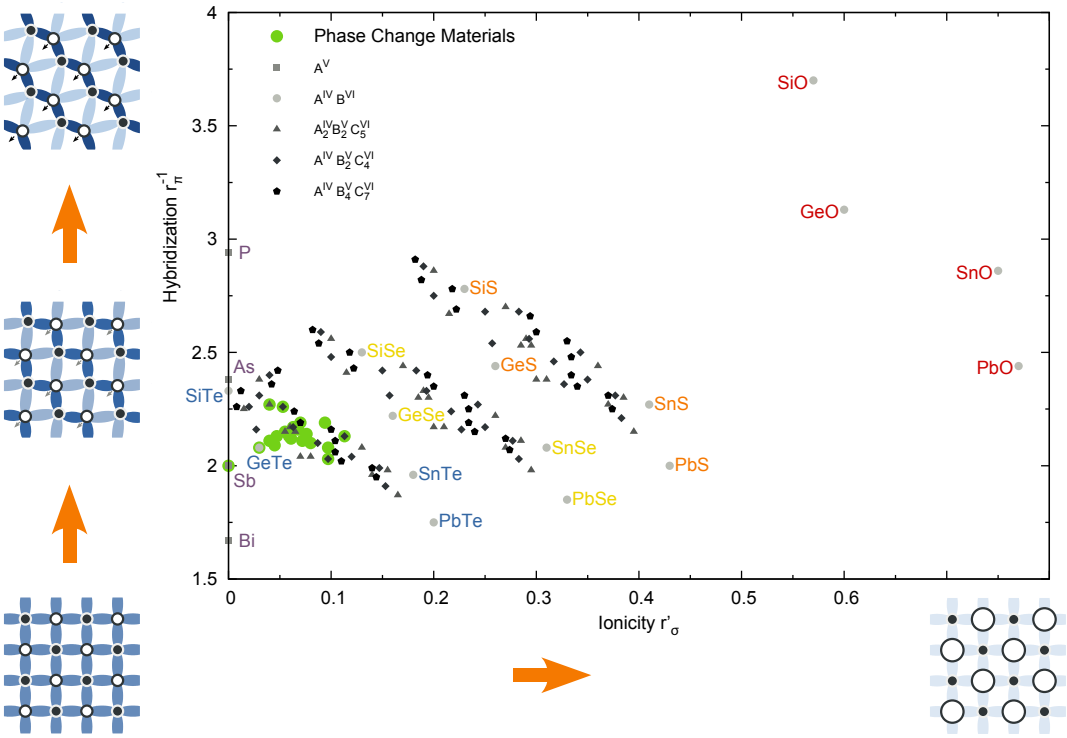

Figure 1.5.: Treasure map for phase-change materials. The tendency towards hybridization and ionicity is shown for many materials. Displayed are materials from group V elements (A^V), binary IV-VI compounds ($A^{IV}B^{VI}$) and ternary alloys with different stoichiometries ($A^{IV}{}_xB^V{}_yC^{VI}{}_z$). Phase-change materials all line up in the region of the lower left corner, whereas oxides, sulfides and selenides are shifted to higher values of both coordinates. Illustrations of the effect of both hybridization and ionicity are shown next to the equivalent axis. A higher degree of hybridization leads to more saturated bonds, and ionicity leads to a localization of the charge carriers at the ion cores. Both ionicity and hybridization lead to a reduction of the resonant character of the bonds. [12]

1.4. Crystal Structure and Disorder in Phase-Change Materials

The concept of the treasure map for phase-change materials can make predictions on the suitability of a material candidate as a phase-change material. The concept of the map assumes a rocksalt structure and calculates average values for the anion and the cation site each. Therefore characteristics of phase-change materials that are dependent on variations of atomic positions or the occupation cannot be predicted by the map. For example crystalline resistivity is strongly dependent on the amount of disorder, which will be shown later. Therefore we will now focus on the crystal structure of phase-change materials and the observed disorder.

Phase-change materials crystallize in a distorted cubic structure, stabilized by resonant bonding via p-orbitals. For the different possibilities of disorder $GeSb_2Te_4$ acts as an example material with a high degree of disorder. However also materials with less disorder, like GeTe, show for a crystalline material much disorder. $GeSb_2Te_4$ crystallizes in a meta-stable NaCl like structure. One sublattice is occupied by Tellurium, while the other is occupied by 50 % Antimony, 25 % Germanium and 25 % intrinsic vacancies. The Ge/Sb/Vac. sublattice is assumed to be randomly occupied [17]. On annealing to higher temperatures (above 250 °C) the meta-stable structure transforms to a stable hexagonal structure. Even though the structure changes from cubic to hexagonal phase, the bonding is still via p-orbitals, thus resonant bonding is maintained. In this stable structure the Ge, Sb and vacancies are ordered in layers [18]. As the hexagonal phase is layered, there has to be an ordering process of the vacancies into layers as well as an ordering process of Germanium and Antimony for this transformation. These two processes mark the first channels for disorder, chemical disorder on the Ge/Sb sublattice and vacancy ordering.

In the assumption of a perfect crystal symmetry all atoms are located on a Bravais lattice. The crystalline phase of phase-change materials are not fulfilling this for all atoms. Displacements for example of Germanium in $GeSb_2Te_4$ have been reported [19]. Also the displacement patterns of Germanium in GeTe is under discussion [20]. Displacements can be either a collective displacement as observed in the Peierls-like 3+3 splitting in GeTe or non-collective of single atoms. These non-collective displacements could be either correlated or non correlated. The reduction of collective displacements would increase the order in phase-change materials. For random orientated displacements, an increase in correlation of the displacement directions would as well increase the order

Different methods are available to determine the crystal structure and the amount of disorder prevalent in a crystalline material. In the following different methods to determine degrees of disorder as listed above will be reviewed. Also results already gained with them will be presented.

The first method that comes to ones mind to determine crystal structure of a solid is x-ray diffraction. Indeed measurements of x-ray diffraction of GeTe and $GeSb_2Te_4$ have been reported in literature [17, 21, 22]. As phase-change materials crystallize on a nanosecond time-scale they form small crystallites in the range of 15-50 nm with random crystal orientation [17]. These small grain sizes make an in depth analysis of x-ray diffraction data complicated, because the peak width is broad (i.e. about 1° for $GeSb_2Te_4$ and Cu K_α radiation). The peak broadening due to finite grain size can be calculated using the Scherrer-formula. Best results can be obtained by powder diffraction. Collective displacements as the Peierls-like 3+3 splitting of the Germanium atom found in GeTe can be detected [22]. For the meta-stable phase of $GeSb_2Te_4$ a cubic structure is observed, displacements or distortions are not resolved in powder diffraction data [17]. The Rietveld analysis [23] of these powder diffraction data have shown large Debye-Waller factors for the Ge/Sb site. Rietveld analyzes only the contribution of the Bragg peaks and not the diffuse scattering in between the peaks. A non-collective, random distortion of single atoms would average out in xrd [20]. There have been attempts to prepare samples with larger grain sizes. Two different approaches have been followed: growth of epitaxial thin films on GaSb [24] and preparation of bulk single crystals [25]. The epitaxial growth of thin films with stoichiometry close to $Ge_2Sb_2Te_5$ has shown Peierls distortion along [1 1 1] in both x-ray and RHEED measurements. The preparation of bulk single crystals seems only possible for stoichiometries on the pseudo-binary line between Sb_2Te_3 and GeTe for materials close to GeTe, like $Ge_7Sb_2Te_{10}$. These sample show as well streaks along [1 1 1] in HRTEM and SAED measurements. Effort has also been put into numerical calculations of the crystal structure of phase-change materials. Density functional theory (DFT) calculations have also evidenced the Peierls splitting [26] in $GeSb_2Te_4$. Calculations of the total energy by means of DFT have shown a displacement of single atoms away from their crystallographic position which depends on the local atomic arrangement, especially of the vacancies [14].

With extended x-ray absorption fine structure measurements (EXAFS) it is possible to probe the local atomic arrangement up to a distance of about 6 Å around one specific chemical element. This enables to determine bond length, coordination numbers and the

bonding elements. EXAFS measurements have been reported for different phase-change materials, like $GeSb_2Te_4$ [27], $Ge_2Sb_2Te_5$ [5] or $Ge_{15}Sb_{85}$ [28]. In the following the results for crystalline $GeSb_2Te_4$ will be discussed. In figure 1.6 the real space function χ(R) of crystalline $GeSb_2Te_4$ is plotted for measurement temperatures between 300 K and 10 K. The function χ(R) is a pseudo pair distribution function. Due to two reasons it is only a pseudo pair distribution function. First due to the phase shift of the photoelectron upon traveling across the non uniform inter-atomic potential one has to add about 0.2 Å to the distances plotted[3]. Second the peak height is correlated with the Debye-Waller factor and not the number of neighbors. The peak height is clearly increasing with decreasing measurement temperature. So the thermal motion, or thermal disorder, of the atoms is drastically reduced on cooling. This is observed for all solid state materials, but seldom in such an extreme way. One can also see the disappearance of the higher shells for temperatures above 10 K. These large thermal displacement are caused by the broad anharmonic potential of $GeSb_2Te_4$ [29]. Interestingly the Debye-Waller factors of $GeSb_2Te_4$ are larger in the crystalline phase than in the amorphous.

In figures 1.7 and 1.8 the real space functions χ(R) of the EXAFS spectra for GeTe and $GeSb_2Te_4$ are plotted for the amorphous and crystalline phase for all K-edges. All measurements were performed at 10 K by van Eijk *et al.* [27]. For GeTe in the amorphous phase a well defined local order and no medium or long range order is observed. In the crystalline phase one can see contributions of multiple shells. This is expected due to the long range order in the crystalline phase.

For $GeSb_2Te_4$ the data draw a different picture. Of course as expected for an amorphous phase, it shows no higher shells as expected as it has no long range order. The crystalline phase, however, also has only little contributions from higher shells. Only the data of the Te-edge show clear signatures of higher shells. Comparing the amorphous with the crystalline phase, one can see that the Germanium edge has the largest difference in nearest neighbor distance. Thus the bonding lengths around Ge changes the most. The peak height of the amorphous and crystalline phase differ. The peak height is correlated with disorder in atomic displacements. Normally these atomic displacements are due to the thermal motion of the atoms, or thermal disorder. As these measurements were performed at 10 K, thermal disorder can be excluded as an origin. Therefore static disorder must be responsible for the large displacements. Surprisingly the amorphous phase shows a higher first peak than

[3] Precise bond lengths can be obtained from a fit of the data.

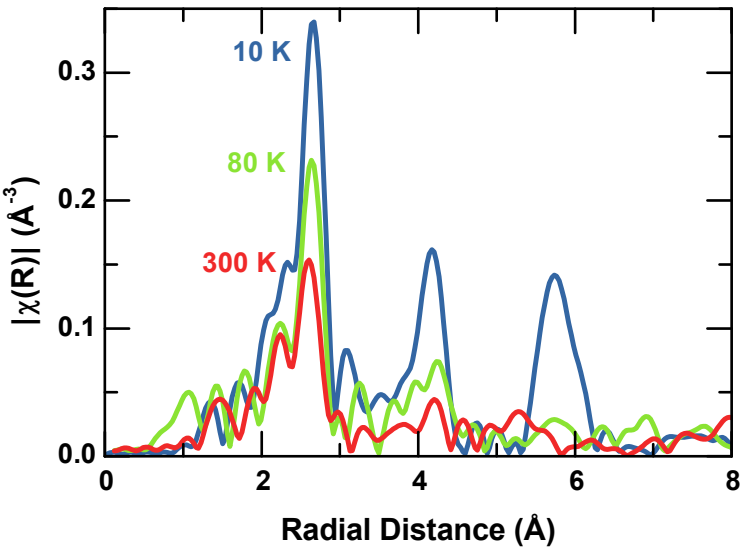

Figure 1.6.: EXAFS data of $GeSb_2Te_4$ measured at different temperatures. The EXAFS data were measured at the K-edge of Tellurium in crystalline $GeSb_2Te_4$ at temperatures between 10 K and 300 K. The information content of the data is obviously enhanced by cooling. For the 10 K data even contributions from the fourth shell around 6 Å are visible. The strong temperature dependence of the Debye-Waller factor can be seen by the increasing peak height for low temperatures. From [27].

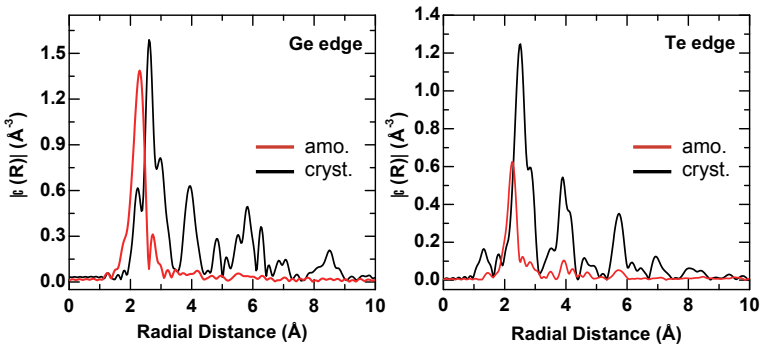

Figure 1.7.: EXAFS data of GeTe: amorphous vs. crystalline. EXAFS data, measured at 10 K, plotted in real space for Germanium and Tellurium K-edge. Due to the lack of long range order of the amorphous phase only the nearest neighbor distance is well defined. For the crystalline phase peaks corresponding to higher coordination shells can be seen. From [30].

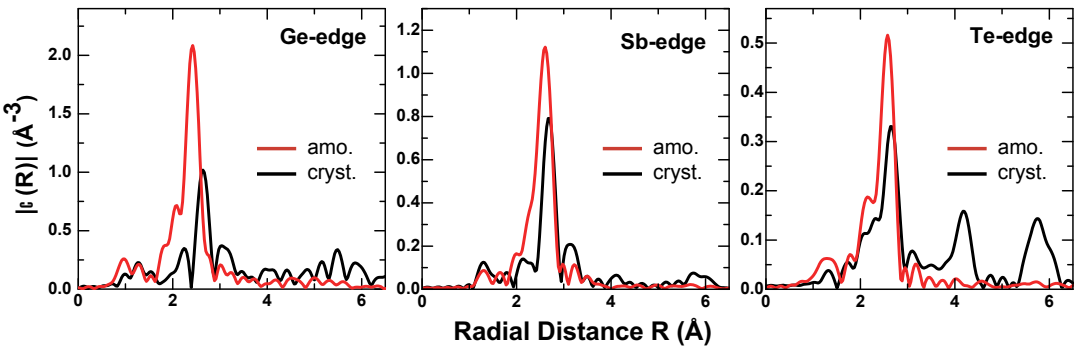

Figure 1.8.: EXAFS data of $GeSb_2Te_4$: amorphous vs. crystalline. EXAFS data, measured at 10 K, plotted in real space for Germanium Antimony and Tellurium K-edge. As for GeTe the amorphous phase is characterized by the lack of long range order. However in contrast to GeTe, $GeSb_2Te_4$ shows a higher nearest neighbor peak in the amorphous data. As the peak height is strongly correlated to the order, it can be concluded that the crystalline phase of $GeSb_2Te_4$ shows a less pronounced order in the nearest neighbor surrounding than in the amorphous phase. From [30].

the crystalline phase for all three edges. This implies that the amorphous phase has higher static order than the crystalline in the short range order.

Neutron pair distribution function (PDF) probes the local atomic arrangement in a range of about 50 Å around an average atom. Compared to EXAFS this large range is an advantage, whereas neutron PDF is not element specific. Measurements of the Pair distribution function G(r) have been performed for $Ge_2Sb_2Te_5$ [19, 31] as well as Sb rich $Ge_2Sb_2Te_5$ and $GeBi_2Te_4$ [32]. These measurements have shown displacements of individual atoms, especially Germanium, from the crystallographic positions. In the framework of this thesis neutron PDF measurements of GeTe and different annealing states of $GeSb_2Te_4$ have been performed. The theoretical background as well as the results will be discussed in chapter 3.

CHAPTER 2

Disorder Induced Localization

The concept of resonant bonding in phase-change materials opened up the possibility to develop the treasure map for phase-change materials [8, 12]. Despite the predictive power of the map, there are inherent limitations. In the map, the coordinates are calculated with average values for the cation and the anion site. Therefore effects that are not governed by an average but rather by a distribution cannot affect the map. Disorder, like vacancy ordering or displacements of single atoms, obviously are characteristics of phase-change materials that are not contained within the map. In this chapter the origin of the electrical conductivity of crystalline phase-change materials will be analyzed in detail. The tuning of the resistivity is of great interest for building electronic data storage devices. It actually opens up a new scientific playground for the study of electrical conductivity in disordered materials. As we look at the resistivity of crystalline phase-change materials, especially the annealing dependance, we might be inclined to deduce two classes of phase-change materials, one with an annealing independent resistivity and one with a distinct annealing temperature dependency of the resistivity. The analysis, however, will show that the difference between the two classes rather results from the amount of disorder present in the material. GeTe and $GeSb_2Te_4$ shall act as prototype materials for this study.

The detailed analysis of the conduction mechanism as presented here was possible thanks to a joint research project coordinated by Prof. M. Wuttig and Prof. T. Siegrist [33] [1].

[1] M. Woda and P. Merkelbach prepared the samples. Measurements were carried out by M. Woda (high-temperature R(T)), P. Merkelbach (X-ray) and H. Volker (low-temperature R(T), Hall effect). The custom-designed Hall set-up was developed by C. Schlockermann. Analysis of the data was carried out by P. Jost.

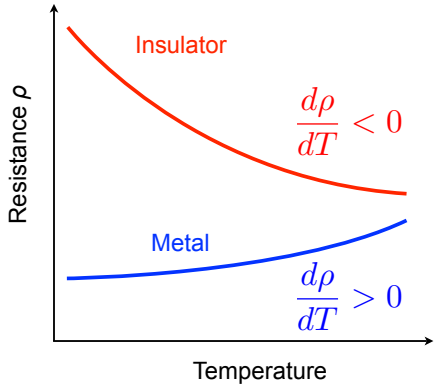

Figure 2.1.: Classification of metal and insulator. Differences of the temperature dependent behavior of the resistivity of insulators and metals. Insulators show a thermally activated charge-carrier transport, which leads to a negative slope ($d\rho/dT < 0$), whereas the resistivity of metals increases with increasing temperatures as a consequence of phonon scattering.

2.1. Resistivity of solids

Studies of the charge-carrier transport mechanism have stimulated scientific research and opened up new fields of solid state physics. Examples for such remarkable new insights are high T_C superconductivity [34] and Quantum Hall effect [35]. As the resistivity ρ of solids spans over more than 32 orders of magnitude [36] it has demonstrated its ability to characterize solids by a single value. From the viewpoint of a theoretician, this spreading of values can be classified into two separate groups by looking at the low-temperature limit of the resistivity. Materials showing a finite resistivity at T = 0 K are called metals; materials showing resistivity values going to infinity as T goes to 0 K are classified as insulators. From an experimentalist's point of view, T = 0 K cannot be reached and extrapolations from low temperature measurements have to be performed. As these extrapolations are not trivial, a different type of classification often employed is preferred in this study: namely the temperature coefficient of resistivity (TCR). The temperature coefficient of resistivity ($\mathrm{d}\rho/\mathrm{d}T$) separates metallic ($\mathrm{d}\rho/\mathrm{d}T > 0$) from insulating ($\mathrm{d}\rho/\mathrm{d}T < 0$) behavior. This classification is depicted in figure 2.1. The diagram also shows that the TCR criterion is usually compatible with the zero temperature limit. Materials undergoing the metal-to-insulator (MIT) transition and the underlying mechanisms will be discussed in the next chapter.

2.2. Metal-Insulator Transition

The classification of materials into metals and insulators raises the question if materials can be systematically changed from a metallic state to an insulating state and vice versa. Indeed various materials undergoing a metal to insulator transition (MIT) via different underlying mechanisms have been found. Examples are doped semiconductors like Si:P or transition-metal compounds like VO_2. Independent of the physical origin of the MIT, Ioffe and Regel derived an approach to give a measure for the occurrence of a metal-insulator transition.

2.2.1. Ioffe-Regel condition

Ioffe and Regel studied the impact of scattering for electronic transport [37]. They assumed electronic transport via extended Bloch states, with scattering modeled by a finite mean free path λ_e in the limit of weak scattering. For mean free paths λ_e shorter than the electron wavelength λ_F, the concept of Bloch *wave* breaks down. As long as the product of Fermi wave vector and electronic mean free path is larger than one ($k_F\lambda_e > 1$), metallic transport via Bloch states can be expected. For values of $k_F\lambda_e < 1$ insulating behavior [37, 38] is observed. The Ioffe-Regel condition therefore gives an indicator for the occurrence of an MIT, that is the point where $k_F\lambda_e = 1$. Gunnarsson *et al.* [39] have shown that the Ioffe-Regel condition can be derived quantum mechanically if one assumes non-interacting electrons and if one assumes the bandwidth of the relevant band W to be significantly larger than the thermal energy $k_B T$. The model of Ioffe and Regel is built independently of the scattering mechanism, and is therefore independent of the origin of the MIT. As for the observation of an MIT a small product of $k_F\lambda_e$ is needed, it is possible to decrease either k_F or λ_e. The Fermi wave vector can be calculated from charge carrier density n by

$$k_F = \left[3\pi^2 \frac{n}{M}\right]^{1/3}, \tag{2.1}$$

with M being the multiplicity of the relevant valence band maximum. Therefore the value of the Fermi wave vector is reduced with the charge carrier density $n^{1/3}$. The mean free path of the charge carriers can be reduced by an increase of scattering, that can result from crystallographic defects and phonons.

2.2.2. Types of Metal-Insulator Transition

Metal to insulator transitions (MIT) are often a consequence of a change in crystallographic long-range order [40]. In VO_2, a transition takes place between a tetragonal high-temperature phase and a monoclinic low-temperature phase [41, 42]. At this transition point the charge carrier density changes by more than 5 orders of magnitude, leading to a change in conductivity by about 4 orders of magnitude. A change in crystallographic phase for an MIT is not mandatory. There are two well-known concepts of an MIT without a change in crystallographic phase, namely the Mott [43] and the Anderson [44] transition.

In figure 2.2, a schematic is drawn for both Mott and Anderson type MIT. In the Mott picture, metallic conduction is present above a critical carrier concentration n_c. For this concentration, there is an interaction between neighboring charge-carriers, which leads to metallic transport. A decrease of the carrier concentration below n_c leads to insulating behavior. The critical carrier concentration n_c can be calculated with the isotropic Bohr radius a_H^* from

$$n_c^{1/3}\, a_H^* = 0.26. \tag{2.2}$$

The isotropic Bohr radius a_H^* itself depends on the effective mass and the static dielectric constant ($a_H^* = 0.53\,\text{Å}\,\epsilon_{st}\,\mathrm{m_e}\,/\,\mathrm{m}^*$). In a Mott MIT, the interplay of two different parameters is important, namely carrier concentration and isotropic Bohr radius.

However, in an Anderson metal-to-insulator transition, it is not the number of carriers which is varied. Instead, disorder leads to a localization of the free electrons. This can be either disorder of the location of the electronic states as depicted in figure 2.2 or disorder in the energy eigenvalues of the electrons. From a certain level onwards, both types of disorder lead to a localization level that no longer allows electronic transport.

The schematic pictures in figure 2.2 show perfect order of the charge-carriers for the Mott case and a constant number of charge-carriers for the Anderson case. This, of course, cannot be realized in an experiment. If the charge-carrier density is varied by way of doping, some positional disorder of the doping atoms will come into play. Therefore a true Mott-like transition is not achievable in an experiment.

A well-studied MIT is the Si:P system. It shows an MIT upon increasing the phosphorus doping concentration [45–47]. Due to the positional disorder of the phosphorous atoms, Si:P has been discussed as an example for an Anderson type MIT [48–50]. As doping of semiconductors shows aspects of both Mott and Anderson, they cannot be associated with

one of them alone. A solid showing only Anderson-like features without Mott-like features has not yet been identified.

2.2.3. Energy scales of MIT transitions

To further distinguish between Mott and Anderson metal-to-insulator transitions, a closer look at the relevant energy scales is enlightening. The Hamiltonian H_0 for a periodic system is extended by a non-periodic potential V_{np} and a term for the electron-electron correlation H_{ee}.

$$H = \underbrace{\frac{p^2}{2m} + V_p}_{H_0} + V_{np} + H_{ee} \tag{2.3}$$

with V_p being the periodic potential. The question is which part the Hamiltonian dominates in what situation. If both the non-periodic potential and the electron-electron (Coulomb) term are negligible, the system can be described, text-book like with energy eigenvalues $E = \frac{\hbar^2 k^2}{2m^*}$. For a Mott-like case the electron-electron correlation energy or Coulomb energy (E_C) is in the same order as the Fermi energy, and the non-periodic potential is much smaller than that. When the non-periodic potential is of the order of H_0 and the electron electron correlation much smaller than both, it is a disorder controlled system, or Anderson case.

For the Mott case the relevant electron-electron correlation energy is the Coulomb energy, whereas for the Anderson case, the mobility edge E_μ is relevant. These energies have to be set in relation to the Fermi energy E_F.

The Mott MIT is governed by electron correlation; therefore, a localization of the charge-carriers is at play as long as the Coulomb energy E_C of the charge-carriers is larger than the Fermi energy E_F [40, 50–52]. These energies can be calculated from the charge-carrier density n, the static dielectric constant ϵ_{st}, the degeneracy of the valence band maximum M and the effective mass m^*:

$$E_C = \frac{e^2}{4\pi\epsilon_0\epsilon_{st}} n^{1/3} \quad \geq \quad E_F = \frac{\hbar^2 (3\pi^2 n/M)^{2/3}}{2m^*}. \tag{2.4}$$

Due to an increase in the carrier concentration n, the Fermi energy is shifted towards the Coulomb energy, passing it at the Mott MIT.

In the case of an Anderson transition, the comparison of the mobility edge E_μ and the Fermi energy E_F is relevant. The non-periodic potential V_{np} causing the localization can have its origin in two different causes. Either the energy eigenvalues of the different atomic

sites can be varying or the transfer matrix element between adjacent sites. The Hamiltonian in a single band approximation [38] can be written as

$$H = \sum_i \epsilon_i n_i + \sum_{i \neq j} J_{ij} c_i^\dagger c_j \tag{2.5}$$

The energy eigenvalues ϵ_i are diagonal and therefore this case is often referred to as *diagonal* Anderson. The second sum is due to the creation and annihilation operators acting on different atomic sites, hence it is off-diagonal. Systems that are dominated by a varying transfer matrix elements are thus called *off-diagonal* Anderson localization. The mobility edge E_μ separates the localized from the delocalized states. As long as the Fermi energy E_F lies within the region of localized states no metallic transport is possible (shaded region in figure 2.13). Therefore disorder has to be reduced for metallic transport until the mobility edge is lifted above the Fermi energy:

$$|E_\mu| > |E_F|. \tag{2.6}$$

It can be concluded that the comparison of the Coulomb energy E_C and mobility edge E_μ with respect to the Fermi energy E_F is crucial to the determination of the prevalent mechanism, Mott or Anderson.

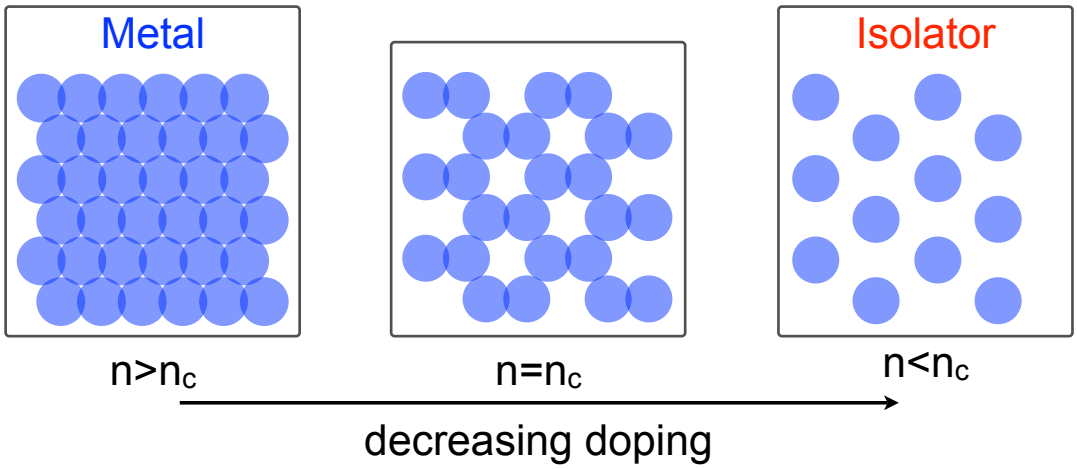

(a)

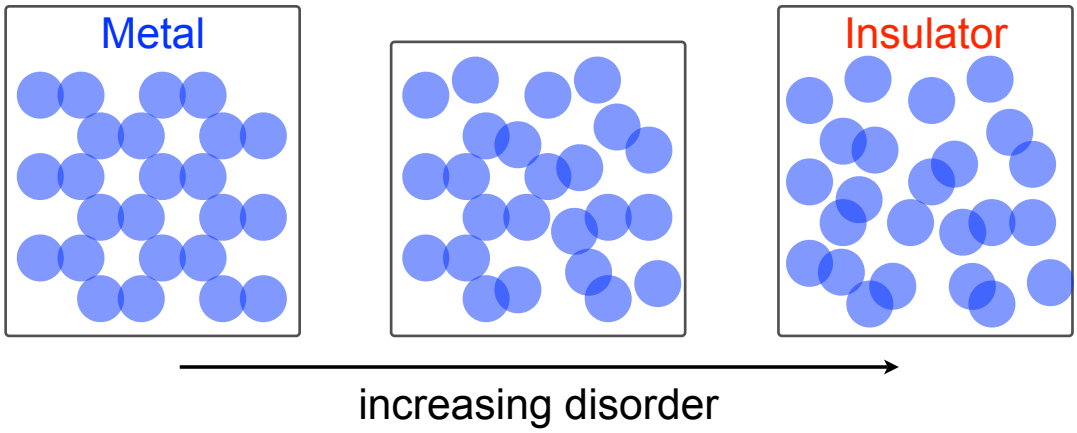

(b)

Figure 2.2.: Comparison of two metal-insulator transition (MIT) concepts: Mott and Anderson. Two different routes for an MIT are prominent: one via changing the carrier concentration (Mott), the other via changing the degree of disorder (Anderson). **(a)** A Mott MIT is induced by a change in carrier concentration n. With a carrier concentration n above a critical concentration n_c, the system shows metallic behavior. Below this critical concentration the system is insulating. **(b)** An Anderson MIT is driven by increasing disorder, leading to a localization of the charge-carriers. Via this change in order, the material changes from metal to insulator. Note that the charge-carrier concentration is constant.

2.3. Temperature dependance of the Resistivity in GeTe and $GeSb_2Te_4$

Figure 2.3 shows the sheet resistance of thin film samples of GeTe and $GeSb_2Te_4$ with film thicknesses of 80 nm and 100 nm respectively. The as deposited amorphous films were heated at a rate of 5 K/min. They were then held at the annealing temperature for 30 min and subsequently cooled down to room-temperature. Both materials lower their amorphous resistance upon heating. As this lowering is reversible, it can be concluded that the amorphous phase shows a thermally activated transport mechanism. The resistance drops significantly when the crystallization temperature is reached. From this point onward, GeTe and $GeSb_2Te_4$ show a different behavior.

For GeTe, the resistance drop on crystallizing to the rhombohedral phase is very steep. Within an interval of just 6 °C (186 - 192 °C), the sheet resistance drops by more than four orders of magnitude. The resistance only decreases by a factor of two on further heating to 300 °C. A strong annealing dependence of the resistivity in the crystalline phase can therefore be excluded. The subsequent cooling down to room-temperature reveals the metallic conduction mechanism of crystalline GeTe. This can be seen in the positive slope of the temperature dependent resistance data (TCR > 0). The room-temperature resistance has decreased by more than six orders of magnitude between the as deposited amorphous and the crystalline phase.

The measurements in figure 2.3 for $GeSb_2Te_4$, however, show a rather complex behavior of the sheet resistance once the crystallization temperature has reached the cubic phase. The step-like decrease of the sheet resistance on reaching the crystallization temperature is not as steep as for GeTe. The drop in sheet resistance for the first crystallization is only about two orders of magnitude over a range of 15 °C (143 - 158 °C). On further heating to 325 °C, the resistance decreases continuously by another two orders of magnitude. On subsequent cooling to room-temperature, $GeSb_2Te_4$ shows metallic behavior for high annealing temperatures only. It is worth noting that the transition to the hexagonal phase is not evident from the R (T) plot.

Step annealing was performed for $GeSb_2Te_4$ with steps of 25 °C in oder to analyze the continuos decrease in resistance of the crystalline phase. These annealing steps are also shown in figure 2.3, marked by the area with the dotted line, where no annealing is done to the sample. In this region the sample is being cooled down to room temperature and is lower than the maximum temperature the sample was exposed to. The region of the dotted

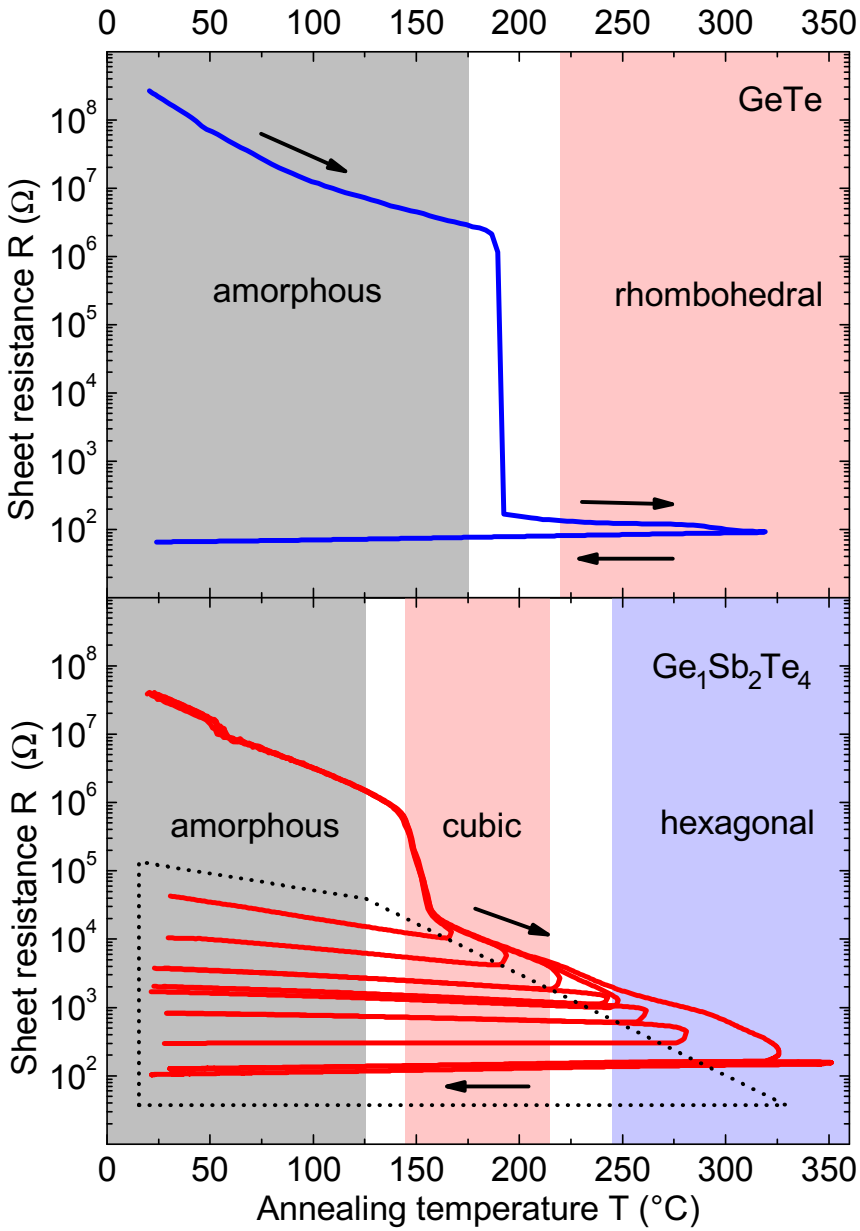

Figure 2.3.: Temperature dependent sheet resistance of GeTe (80 nm thick) and $GeSb_2Te_4$ (100 nm thick). Beginning in the amorphous semiconducting phase, both materials crystallize, which results in a reduction of the resistance by at least three orders of magnitude. One material (GeTe) does not change its metallic resistance with further annealing, while the resistance of the other ($GeSb_2Te_4$) is continuously lowered with annealing. The reduction of the crystalline sheet resistance is accompanied by a change in slope from negative (semiconducting) to positive (metallic) values. Measurements performed by Woda [53]

line confirms the continuos lowering of the room-temperature resistance by more than two orders of magnitude on annealing. Along with this lowering, the slope also changes continuously from negative values to positive ones, showing a transition from non-metallic to metallic behavior for $GeSb_2Te_4$.

Further measurements with other pseudo-binary materials were performed to deepen the understanding of the continuos change in resistance and slope on annealing of $GeSb_2Te_4$. Figure 2.4 shows measurements for 100 nm thick films of $GeSb_4Te_7$, $GeSb_2Te_4$,$Ge_2Sb_2Te_5$ and $Ge_3Sb_2Te_6$. Only data on cooling to room-temperature are shown in order to decouple annealing effects from temperature dependent behavior. The data shown in 2.4 are the same as the data marked by the dotted region in figure 2.3. It is remarkable to see that all four different GeSbTe alloys show qualitatively and quantitatively the same behavior on step annealing. They all show a non-metallic behavior at the lowest crystallization temperature. Both the slope and the room-temperature value of the materials change continuously, almost like parallel lines, which leads to a change from non-metallic to metallic behavior. The boundary separating metallic from non-metallic behavior is at a critical resistivity $\rho_C = 2-3$ mΩcm for all materials.

This behavior of four different GeSbTe alloys is a first indication for a generic metal-to-insulator transition in a group of phase-change materials. As discussed above (see 2.2.2) up to now no MIT has been observed, which could be identified as a pure Anderson type MIT. Phase-change materials are known to have an unusual degree of disorder in the crystalline phase (see 1.4) and the driving force for the MIT seem to be a thermally induced relaxation process. Therefore it is in the nature of a scientist to perform further measurements to gain insight into the underlying mechanisms of this MIT. Thereby the frontier in the field of physics can be pushed to widen the knowledge. With step annealed samples of GeTe and $GeSb_2Te_4$ measurements were taken on low temperature resistivity, Hall, Fourier transformed infrared spectroscopy (FTIR) and X-ray diffraction. The results will be discussed in the following sections.

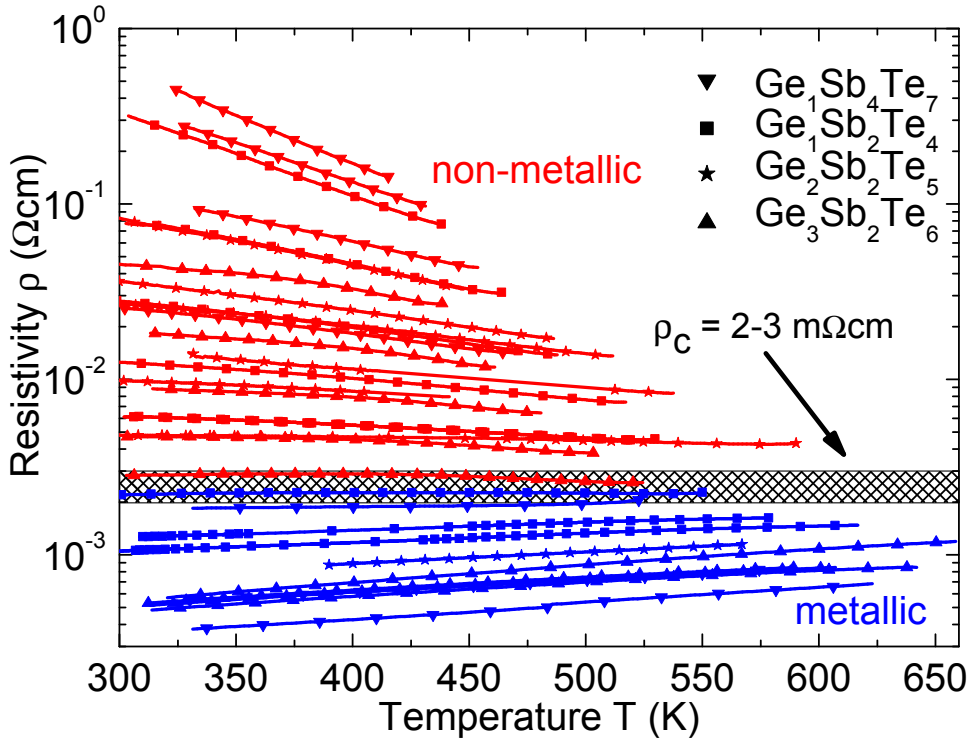

Figure 2.4.: Effect of annealing on the resistivity and its temperature dependance. A systematic change of resistivity and slope (TCR) is observed for four different GeSbTe alloys. Only data on cooling are shown (see marked region in Fig. 2.3) in order to exclude annealing effects. The conduction mechanism changes at a critical value of 2-3 mΩcm from non-metallic ($d\rho/dT < 0$) to metallic behavior ($d\rho/dT > 0$). The both qualitative and quantitative equal behavior for the different alloys supports the generic MIT on annealing. Measurements performed by Woda [53]

2.4. Low temperature measurements of $GeSb_2Te_4$

To verify the existence of the MIT at low temperatures and to verify the consistency of the TCR criterion with the low temperature limit of the resistivity, low temperature resistivity measurements were performed. The van der Pauw technique [54] was applied in combination with a liquid helium glass cryostat (measurements performed by Volker [55]).

In figure 2.5, resistivity data down to 5 K are shown for samples annealed between 150 °C and 325 °C. For samples annealed to temperatures lower than 275 °C, a negative slope is observed, which indicates non-metallic behavior. The most pronounced increase in resistivity is observed for the sample annealed to 150 °C. In the low temperature regime from 5 to 70 K, this sample can be fitted by a variable range hopping model of the conductivity $\sigma = \sigma_0 \exp[-(T_0/T)^{1/4}]$ [56, 57]. In the Mott variable range hopping model electrical conduction via hopping is assumed [58]. The hopping probability is dependent on the spatial separation of the states as well as there energy mismatch. Therefore the variable range hopping model is valid especially for systems that are governed by disorder. The extrapolation of this model yields a freeze-out of the conductivity for T→0 K. The good agreement of the data with this model solidifies the existence of an MIT in phase change materials. The samples annealed to 275 °C show a vanishing slope that is maintained down to 5 K. For samples annealed above 275 °C, the slope changes to positive, consistent with a metallic transport mechanism. With respect to figure 2.4, it is worth noting that both the metal-to-insulator transition is maintained in the entire measurement range from 5 K to 600 K, and the critical resistivity value also remains constant at 2.7 mΩcm. To clarify the origin of the MIT observed here, XRD, Hall, and FTIR measurements were performed with the step annealed samples of $GeSb_2Te_4$. XRD measurements are carried out to determine changes in crystallographic phase and grain size effects. $GeSb_2Te_4$ is known to change its crystallographic phase from a meta-stable NaCl-like phase to the stable hexagonal phase [17]. Therefore it is important to study the transition temperature of the change in crystallographic phase. The combination of Hall and FTIR measurements are used to deduce the annealing dependend transport parameters for electrical transport, that is the conductivity σ, the carrier concentration n, the mobility μ, the scattering time τ, the effective mass m^*, the Fermi wave-vector k_F, the Fermi energy E_F, the mean free path λ_e and the resistivity ratio r_σ.

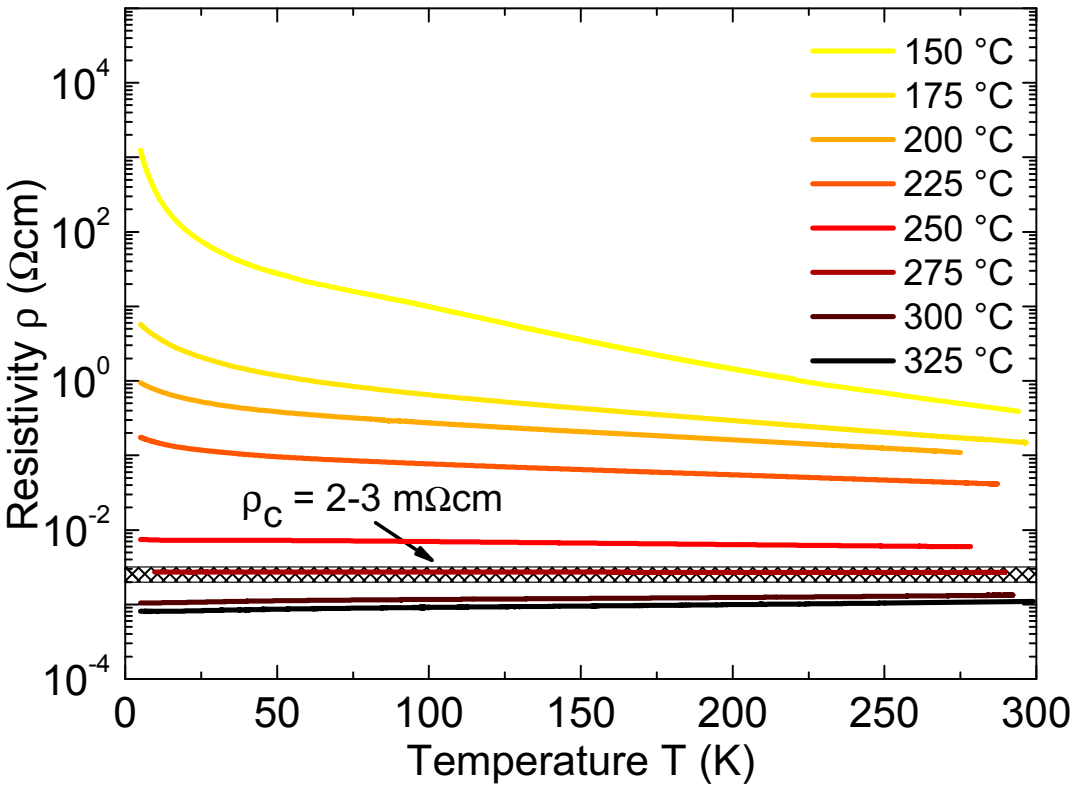

Figure 2.5.: Low temperature resistivity of different annealed crystalline $GeSb_2Te_4$ films. Resistivities between 5 and 300 K are shown for eight samples annealed in the range from 150 to 325 °C. The non-metallic character of the TCR for annealing temperatures lower than 275 °C is preserved down to 5 K (compare Fig. 2.4). This implies a charge-carrier freeze-out at zero temperature. The resistivities of the samples annealed to temperatures higher than 275 °C remain metallic (TCR>0) throughout the range. It is noteworthy that the critical boundary resistivity between metallic and non-metallic behavior observed in Fig. 2.4 is valid throughout the temperature range. See also Fig. B.1 (Data taken by Volker [55].)

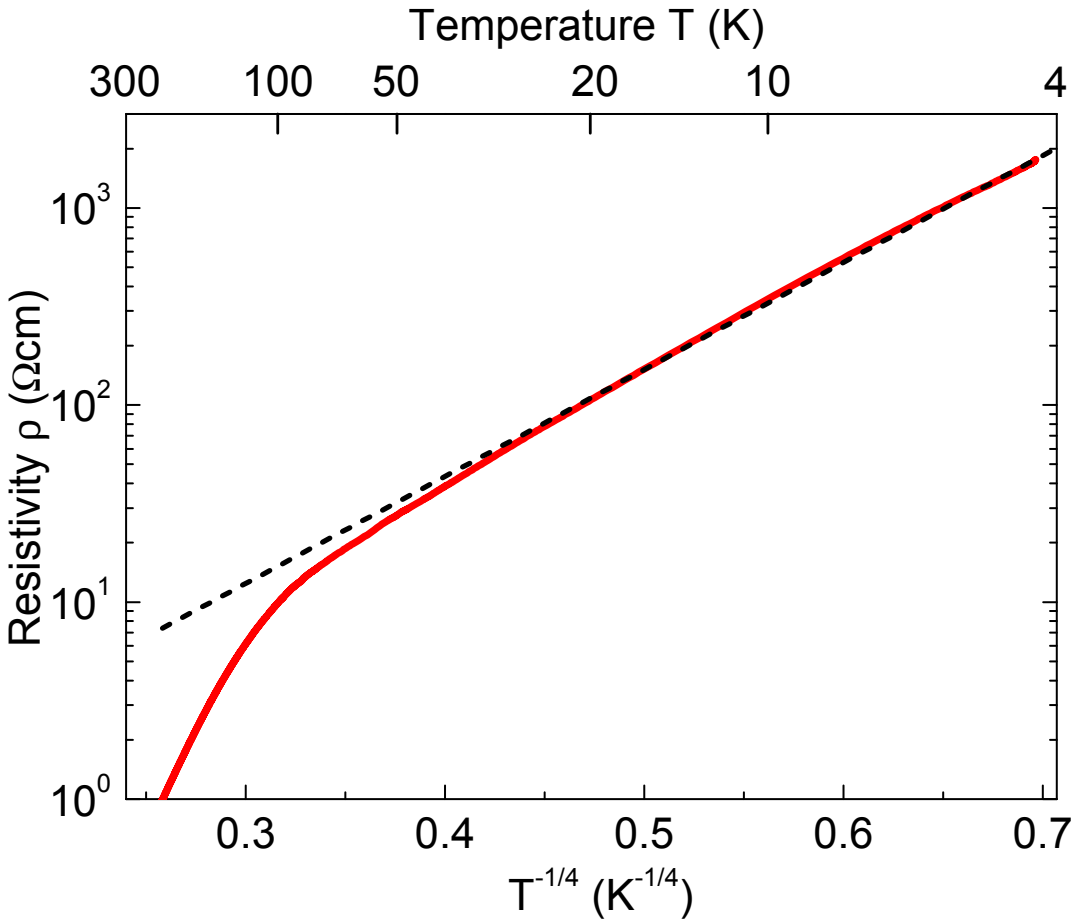

Figure 2.6.: Variable range hopping model fitted to $GeSb_2Te_4$. For low measurement temperatures - between 5 and 70 K - the resistivity of the $GeSb_2Te_4$ sample annealed at 150 °C can be fitted with a variable range hopping model. This supports the assumption of a freeze out in conductivity as T goes to 0 K.

2.5. X-ray diffraction analysis of the MIT

An MIT has been observed in VO_2, for example, with a change in crystallographic phase. VO_2 undergoes at 340 K a change from an insulating monoclinic phase (below 340 K) to a metallic rutile structure [41]. Temperature dependent changes of resistivity, as well as charge carrier density, and mobility is plotted in fig. 2.7. Accompanied with this change in crystal structure at 340 K the resistivity is lowered by about four orders of magnitude [41]. Hall measurements reveal an increase of the carrier concentration at the transition temperature of more than 5 orders of magnitude to values higher than one carrier per V atom [42]. As the carrier mobility hardly changes, it can be concluded that the structural change of VO_2 leads to an increase of the carrier concentration and this leads to a change from non-metallic to metallic behavior.

As can be seen from VO_2, the determination of the crystal phase and the transport parameters were the key elements to clarify the origin of the MIT. To see if the MIT observed for $GeSb_2Te_4$ is related to the known structural transition from cubic to hexagonal phase in a similar way, x-ray diffraction (xrd) was carried out on step annealed films of GeTe and $GeSb_2Te_4$. Changes in the crystallographic phase and grain size effects can be analyzed with these measurements. Following this section Hall and FTIR measurements will be discussed.

X-ray diffraction measurements were performed using Copper K_α x-rays with a wavelength $\lambda = 1.5418$ Å in an x-ray diffractometer from PANalytical[2]. All measurements were performed in gracing incidence geometry [61] with the identical thin film samples that had already been used for the FTIR experiments. In figure 2.8, the corresponding diffraction patterns for step-annealed GeTe and $GeSb_2Te_4$ are shown.

GeTe crystallizes into a rhombohedral phase with a lattice constant of a = 4.29 Å and a rhombohedral angle $\alpha = 58.5°$ on annealing to 225 °C. Further annealing does not change the crystallographic phase, but at 250 °C a peak corresponding to pure Germanium appears at $2\theta = 27.35°$ in the diffraction pattern, indicating phase segregation. On further annealing, this Germanium peak sharpens, but the peak area remains constant. Therefore, it is very likely that Germanium was present alongside the GeTe structure. High resolution TEM analysis supports this assumption. Laptyeva [63] has shown that GeTe films crystallized at 250 °C show a Ge excess within the grain boundaries of GeTe crystallites. Figure 2.9 shows these TEM measurements. In the bright field image (BF) a grain boundary can be seen,

[2] http://www.panalytical.com/

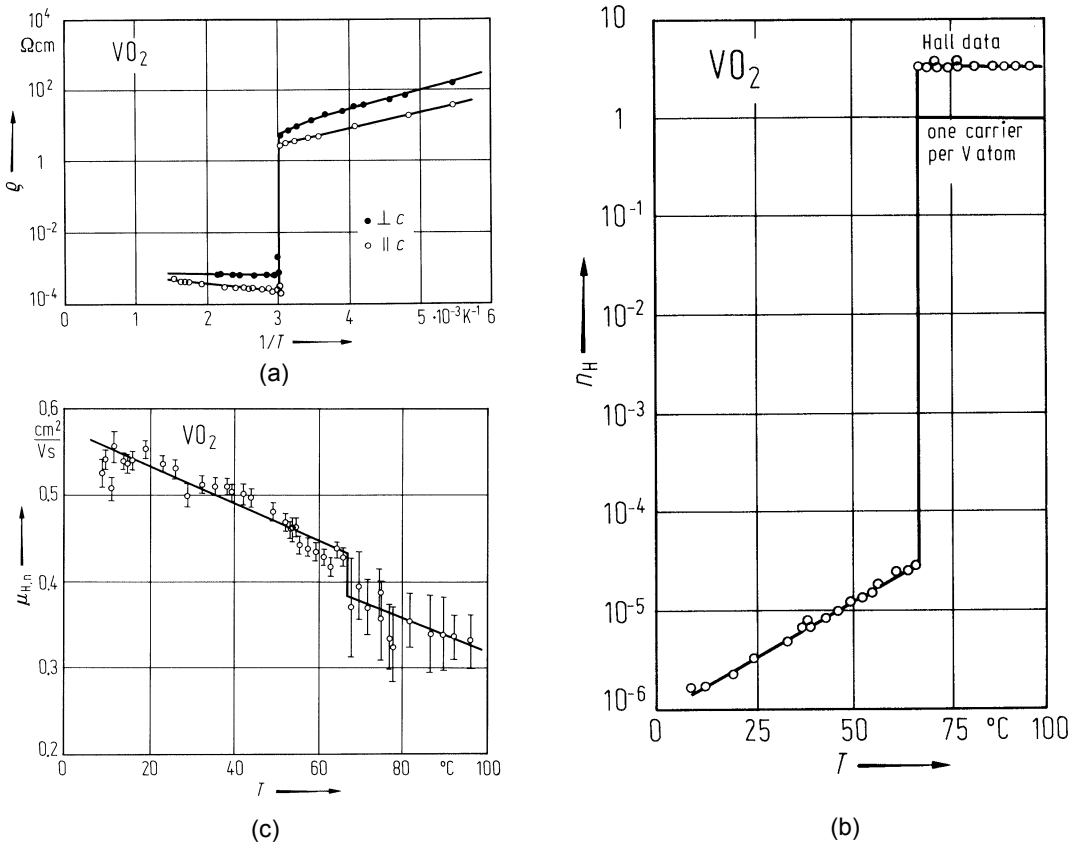

Figure 2.7.: Transport parameters of VO_2 as a function of temperature. (a) The resistivity measurement of VO_2 shows a step-like transition from non-metallic to metallic behavior at 340 K [41, 59]. At the transition point, the carrier concentration increases by five orders of magnitude **(b)**, while the mobility is showing only a small change [42, 60].

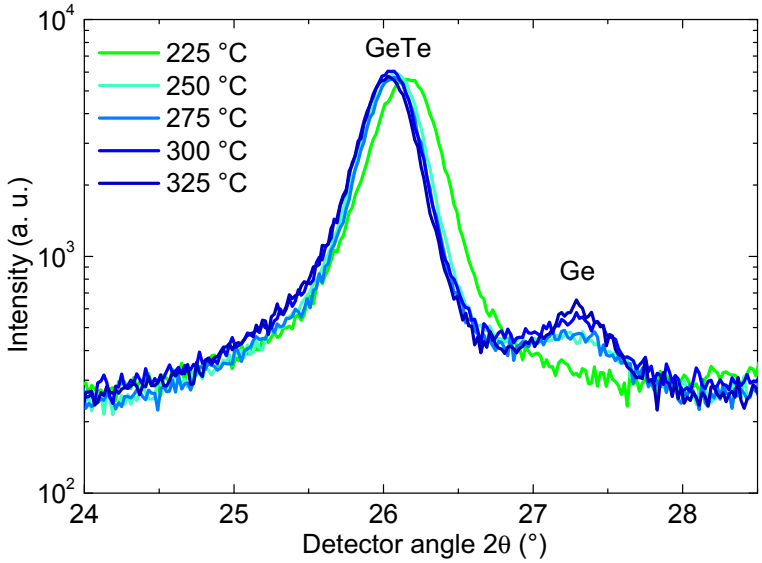

(a)

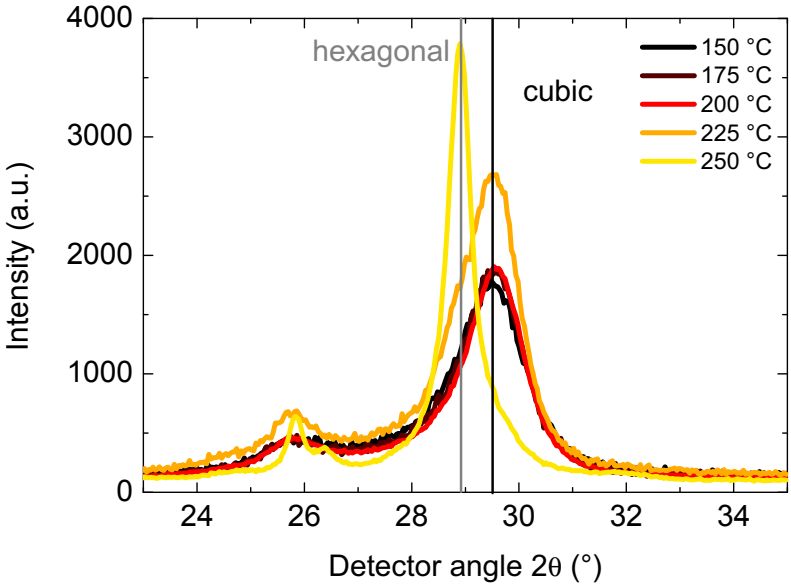

(b)

Figure 2.8.: X-ray diffraction pattern and its evolution on annealing of GeTe and $GeSb_2Te_4$. **(a)** Annealing effect on X-ray diffraction pattern of GeTe. GeTe crystallizes in the rhombohedral α phase at 225 °C. On further annealing, a small fraction of Ge is segregated from the GeTe lattice and crystallizes as pure Germanium, visible as a peak at $2\theta = 27{,}35°$. This is consistent with the crystallization temperature of pure Ge of 250 °C [62]. **(b)** $GeSb_2Te_4$ crystallizes into an NaCl-like cubic structure on annealing to 150 °C. Further annealing to 175 °C and 200 °C does not render visible differences in the XRD spectra. At 225 °C, the diffraction pattern changes and consequently, at 250 °C, the final transition leads to the hexagonal phase.

going from the upper left corner to the lower right corner. The element specific images for Ge and Te show a lower Te concentration within the grain boundary compared to the rest of the image, whereas the Ge-elemental map shows an enhanced Ge concentration within the grain boundary. The segregation of Ge clusters into the grain boundary is also compatible with the finding of Ge empty lattice sites in GeTe [30].

The situation expected for $GeSb_2Te_4$ is more complex than the one for GeTe, as $GeSb_2Te_4$ shows a strong annealing dependence of the conductivity along with the observed MIT. In figure 2.8, the diffraction patterns of step-annealed samples are shown. At 150 °C, $GeSb_2Te_4$ crystallizes into an NaCl-like structure, which is preserved up to 200 °C. On annealing to 225 °C, the diffraction pattern shows both peaks of the cubic and the hexagonal phase. This transition to the hexagonal phase is completed at 250 °C. On first sight, one might consider to link this phase transition to the observed MIT. However, the transition temperatures of crystallographic transition at 225 °C and MIT at 275 °C are not compatible with each other. In contrast to VO_2, where a gap at the Fermi energy opens due to a change in local bonding, the p-type bonding in $GeSb_2Te_4$ does not change with the transition from cubic to hexagonal. The transition is dominated by an ordering of Ge, Sb and vacancies into layers. The bond length and bond angles however do not change significantly (see section 3.7). Therefore in contrast to VO_2 the relevant band is not changed.

The change in conductivity and the MIT observed in $GeSb_2Te_4$ on annealing could be attributed to changes in grain size and grain boundary. Such a model has, indeed, been proposed by Prokhorov *et al.* [64]. However, there are a number of reasons why this is not the case in $GeSb_2Te_4$. In order to evaluate the possible effects of grain growth, figure 2.10 shows the evolution of the full width at half maximum (FWHM) of the cubic (200) reflex for $GeSb_2Te_4$ and GeTe. The FWHM reduces for both materials on annealing, but even for $GeSb_2Te_4$ the change is less than a factor of two. As the FWHM is inverse proportional to the grain size [65], the change of the FWHM by less than a factor of two would lead to a similar change in grain sizes. The grain size can be estimated to change from 150 Å to about 300 Å. This change in grain size is not expected to alter the conductivity to such an extent as observed here. Especially when comparing the grain size to the mean free paths calculated from Hall measurements (see section 2.6). The mean free paths for $GeSb_2Te_4$ and GeTe is for all annealing stages smaller than 25 Å(in the order of four unit cells), thus more than 1 order of magnitude smaller than the grain size. In granular metals, like Al or Ni-SiO_2 [66], hopping transport with scattering at the grain boundaries was observed. Therefore a modification of

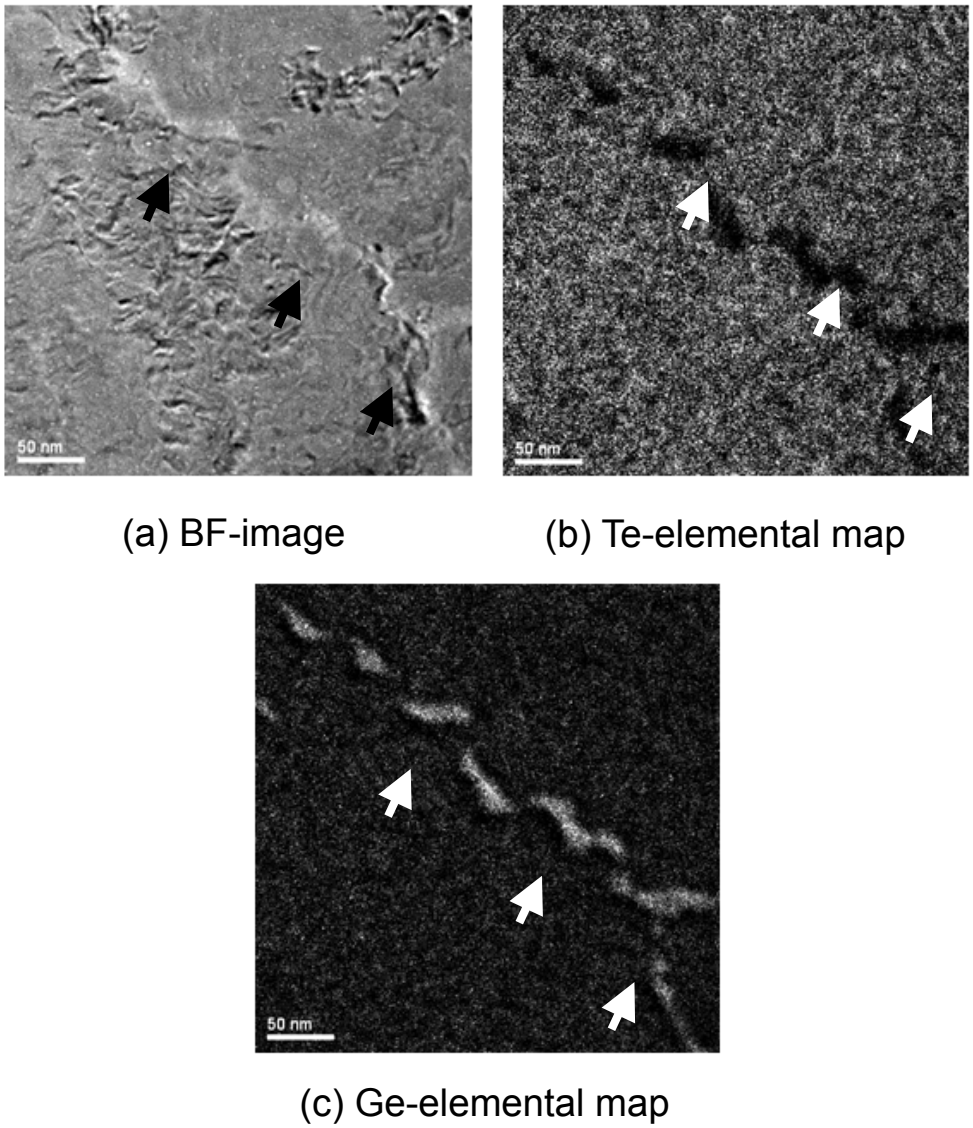

(a) BF-image (b) Te-elemental map

(c) Ge-elemental map

Figure 2.9.: Ge segregation in the grain boundaries of GeTe. (a) The bright field image (BF) shows a grain boundary in crystalline GeTe across the image. The elemental maps of Te (b) and Ge (c) reveal a higher Ge concentration and a lower Te concentration within the region of the grain boundary as compared to the rest of the sample [63]. A crystallization of Ge segregated into the grain boundaries can therefore be a likely explanation for the Ge peak seen in figure 2.8.

the grain boundaries in $GeSb_2Te_4$ could also be relevant. This can, however, be excluded as a cause for the change in conductivity. Measurements of the conductivities via the van der Pauw method and calculated values from the FTIR fits agree with each other (see 2.1). In the FTIR model no grain boundaries are incorporated [67], and therefore the agreement of the two methods excludes grain boundaries as dominant origin of the conductivity.

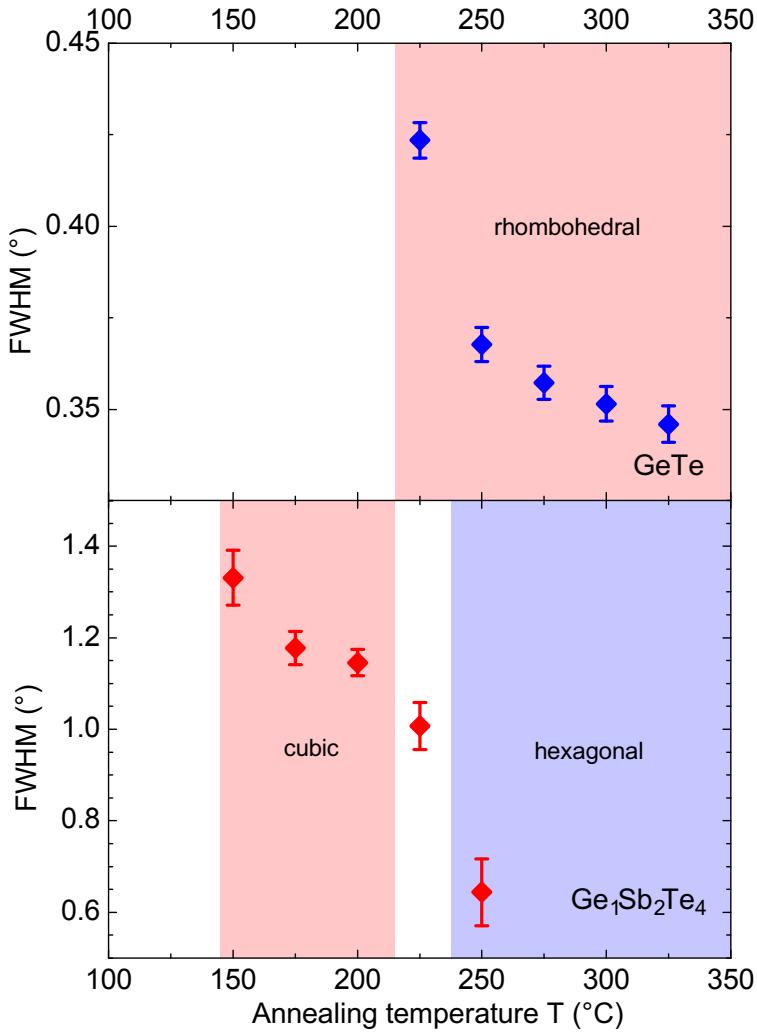

Figure 2.10.: Changes of the FWHM of GeTe and $GeSb_2Te_4$ on annealing. Full width at half maximum (FWHM) of the cubic (200) diffraction peak of GeTe and $GeSb_2Te_4$ as a function of annealing temperature. The spectra were measured with Cu K_α radiation in grazing incidence geometry (ω=1°). For both materials, the FWHM decreases continuously with higher annealing temperatures. GeTe crystallizes into the rhombohedral phase after annealing to 225°C. The decrease of the FWHM is accompanied by Ge segregation at 250°C (Fig. 2.8). $GeSb_2Te_4$ crystallizes at 150°C into the meta-stable cubic phase. Subsequent annealing results in the transition to the hexagonal phase at 225°C.

2.6. Transport parameter of GeTe and $GeSb_2Te_4$

In the following, the transport parameter will be studied in detail to identify the origin of the MIT found in phase-change materials. Hall, FTIR, and X-ray diffraction measurements were performed with the step-annealed samples of GeTe and $GeSb_2Te_4$. The charge-carrier density n and the charge-carrier mobility μ can be calculated from Hall and van der Pauw data. The FTIR data were analyzed using a semiconductor model (Tauc-Lorenz oscillator) with a free electron Drude contribution. From this, the scattering time τ and the, by the effective mass m* modified, charge-carrier density $\tilde{n} = n m_e / m*$ can be calculated.

The transport parameters are determined in the framework of a degenerately doped semiconductor with the Fermi level located within the valence band [68]. The multiplicity M of the valence band maximum must be taken into account when calculating the Fermi wave vector or related quantities. In literature, the relevant valence band maximum for IV-VI compounds (GeTe[69, 70], PbTe[69, 71]) is given at the L-point, with a fourfold degeneracy. The same fourfold multiplicity (M=4) is assumed in all calculations both for GeTe and step-annealed $GeSb_2Te_4$. Therefore the transport parameters are calculated by the following equations:

$$\text{Fermi wave vector} \quad k_F = \left[3\pi^2 \frac{n_{\text{Hall}}}{M}\right]^{1/3} \tag{2.7}$$

$$\text{effective mass} \quad \frac{m^*}{m_e} = \frac{n_{\text{Hall}}}{\left[n \cdot \frac{m_e}{m^*}\right]_{\text{FTIR}}} \tag{2.8}$$

$$\text{Fermi energy} \quad E_F = \frac{\hbar^2 k_F^2}{2\, m^*} \tag{2.9}$$

$$\text{Fermi velocity} \quad v_F = \hbar \frac{k_f}{m^*} \tag{2.10}$$

$$\text{mobility} \quad \mu = \frac{\sigma_{\text{vdP}}}{e\, n_{\text{Hall}}} \tag{2.11}$$

$$\text{mean free path} \quad \lambda = \frac{\hbar}{e^2}\, \sigma_{\text{vdP}} \left[\frac{3\pi^2}{n_{\text{Hall}}^2\, M}\right]^{1/3} \tag{2.12}$$

$$\text{Conductivity ratio} \quad r_\sigma = \sigma_{\text{measured}} \,/\, \sigma_{\text{min}} = \sigma_{\text{measured}} \cdot \rho_{\text{max}} \tag{2.13}$$

The values of the transport parameters determined with the model of a degenerately doped semiconductor are displayed in figure 2.11 and table 2.1, both for GeTe and $GeSb_2Te_4$. As mentioned above, no strong annealing effect is expected for GeTe. Indeed, the conductivity σ changes only by about 30 % between annealing temperatures of 225 °C and 325 °C. This holds true for values determined by van der Pauw measurements and for values calculated from the FTIR spectra. The changes of the carrier concentration n and the carrier mobility μ gained from Hall measurements show that the change in conductivity is due to a change in carrier mobility by 30 %. The resistivity ratio r_σ is above 1 for all annealing temperatures indicating metallic transport. This is in line with the assumption of GeTe to be a degenerated semiconductor [72]. The resistivity ratio value of four in crystalline GeTe is still very close to the MIT.

As $GeSb_2Te_4$ shows a strong annealing effect of the resistivity, the evaluation of the transport parameter is expected to change more strongly with annealing than for GeTe. Figure 2.11 top shows a change in room-temperature conductivity by more than a factor of 400 on annealing between 150 °C and 325 °C (values also listed in table 2.1). Even though the conductivity changes so much, the carrier concentration n increases only by a factor of 3. The carrier mobility, however, changes by a factor of more than 100. This indicates that this change is the cause both for the change in conductivity and for the MIT itself.

With the Ioffe-Regel condition, we can estimate the minimum metallic conductivity predicted by Mott [73], using $1/\sigma = \rho = 3\pi^2\hbar/e^2k_F^2\lambda_e M$ (see section 2.2.1). The product $k_F\lambda_e$ is one at the MIT. The minimum metallic conductivity can be calculated with the fourfold degeneracy of the valence band maximum (M=4) using:

$$1/\sigma_{min} = \rho_{max} = 3\pi^2\hbar/4e^2k_F. \tag{2.14}$$

The Fermi wave vector k_F can be calculated from the carrier concentration n by

$$k_F = (3\pi^2 n/M)^{1/3} \tag{2.15}$$

(table 2.1). For $GeSb_2Te_4$ the minimum metallic conductivity calculated is $\sigma_{min} = 37$ S/cm, equalling a maximum metallic resistivity of $\rho_{max} = 2.7$ mΩcm. This agrees with the measured critical resistivity observed in all GeSbTe alloys, see figure 2.4. Note that these two values have been determined independently, one is calculated from the carrier density measured with Hall, the other is determined by the change in TCR.

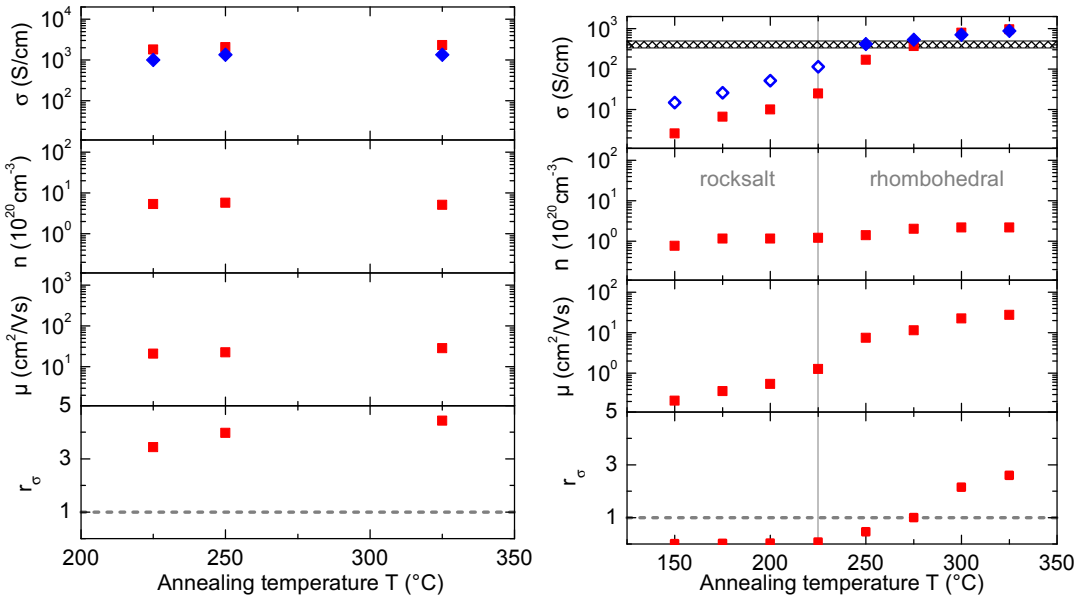

(a) **GeTe.**

(b) **$GeSb_2Te_4$.**

Figure 2.11.: Summary of the transport parameter of GeTe and $GeSb_2Te_4$. Displayed from top to bottom are electrical conductivity σ , carrier density n, mobility μ and resistivity ratio $r_\sigma = \rho_{max}/\rho_{measured}$. Electrical-measurement values (Hall and van der Pauw) are shown as red squares; optical measurements (FTIR) are shown as blue diamonds. Open diamonds indicate that the Drude parameters (τ and n m_e /m) cannot be decoupled. **(a)** Almost no annealing temperature dependence of the transport parameters can be observed except for the small effect caused by Ge segregation (occurring) between 225 and 250 °C (Fig 2.8). The conductivity ratio r_σ for degenerate semiconductors is significantly larger than 1, as expected. **(b)** Optical and electrical conductivities show a pronounced increase on annealing, whereas the Hall carrier density is almost constant, evidence that this effect is caused by a mobility increase. The transition of the resistivity ratio r_σ from values smaller than one to values larger than one is indicative of a transition from localized to delocalized charge-carriers. This is in line with the change in sign of the TCR (see figures 2.3 and 2.4).

Table 2.1.: Transport parameter of GeTe and $GeSb_2Te_4$. Listed are: conductivity measured with van der Pauw geometry σ_{vdP}, conductivity determined by FTIR σ_{FTIR}, charge-carrier density n determined by Hall and FTIR ($nm_e/m*$), charge-carrier mobility μ, scattering time τ, effective mass $m*/m_e$, Fermi wave vector k_F and Fermi energy E_F, mean free path λ_e, resistivity ratio r_σ, temperature coefficient of resistivity TCR and the crystallographic phase. All values were calculated using a model of a degenerated semiconductor with a fourfold degeneracy of the valence-band maximum. This model breaks down for low annealing temperatures of $GeSb_2Te_4$ as the resistivity ratio r_σ shows. The un-physically low mean free paths, lower than the atomic spacing, also demonstrate the breakdown of the model.

Material	**GeTe**		
Annealing temp.	**225 °C**	**250 °C**	**325 °C**
σ_{vdP} (S/cm)	1799	2074	2319
σ_{FTIR} (S/cm)	1012	1339	1352
n (10^{20} cm^{-3})	5.3	5.7	5.1
n m_e/m^* (10^{20} cm^{-3})	14.7	19.5	20.2
μ (cm^2/Vs)	21.1	22.5	28.3
τ (fs)	2.5	2.4	2.4
m^* / m_e	0.4	0.3	0.3
k_F (10^7 cm^{-1})	1.58	1.62	1.56
E_F (eV)	0.26	0.34	0.37
λ_e (Å)	21.9	24.0	29.0
$r_\sigma = k_F\lambda$	3.46	3.89	4.52
TCR = ΔR/R / ΔT/T	$2.53\cdot10^{-5}$	$2.59\cdot10^{-5}$	n.a.
Crystalline phase	rhomb.	rhomb.	rhomb.

Material	**$GeSb_2Te_4$**							
Annealing temp.	**150 °C**	**175 °C**	**200 °C**	**225 °C**	**250 °C**	**275 °C**	**300 °C**	**325 °C**
σ_{vdP} (S/cm)	2.6	6.7	10.1	24.8	170	370	794	962
σ_{FTIR} (S/cm)	15	26	52	114	414	531	711	885
n (10^{20} cm^{-3})	0.8	1.2	1.2	1.2	1.4	2.0	2.2	2.2
n m_e/m^* (10^{20} cm^{-3})	> 0.5	> 0.9	> 2.3	3.2	4.4	5.2	5.0	5.8
μ (cm^2/Vs)	0.2	0.4	0.5	1.3	7.5	11.4	22.6	27.5
τ (fs)	< 1.0	< 1.0	< 0.8	1.3	3.4	3.6	5.1	5.5
m^* / m_e	< 1.5	< 1.2	< 0.5	0.4	0.3	0.4	0.4	0.4
k_F (10^7 cm^{-1})	0.83	0.95	0.95	0.96	1.01	1.14	1.17	1.17
E_F (eV)	0.02	0.03	0.07	0.09	0.12	0.13	0.12	0.14
λ_e (Å)	0.11	0.23	0.34	0.81	5.0	8.6	17.5	21.3
$r_\sigma = k_F\lambda$	0.01	0.02	0.03	0.08	0.51	0.98	2.05	2.49
TCR = ΔR/R / ΔT/T	$-9.37\cdot10^{-5}$	$-3.48\cdot10^{-5}$	$-2.24\cdot10^{-5}$	$-1.33\cdot10^{-5}$	$-2.85\cdot10^{-5}$	0.00E+00	$2.59\cdot10^{-5}$	$3.55\cdot10^{-5}$
Crystalline phase	rocksalt	rocksalt	rocksalt	trans.	hex.	hex.	hex.	hex.

The occurrence of the MIT at annealing temperature of 275 °C is therefore supported by three criteria:

- the change of the sign of TCR at the MIT
- the zero temperature limit of the resitivity
- the maximum metallic resistivity

With these clear indications for the existence of the MIT, the question of its origin is still to be answered. Edwards *et al.* [40] have shown for the electron correlation driven case (Mott MIT) that the critical carrier concentration derived by Mott [43]

$$n_c^{1/3} a_H^* = 0.26 \tag{2.16}$$

is a valuable measure for a large range of materials. The Mott criterion can be understood as well in the framework of the energy arguments, discussed earlier. At the Mott transition the Coulomb energy E_C exceeds the Fermi Energy E_F and therefore the electron-electron correlation can no longer be neglected. The Bohr radius a_H^* of the donor/acceptor state is calculated from the effective mass and the static dielectric constant ϵ_{st} as

$$a_H^* = 0.53 \mathring{A}\, \epsilon_{st} \frac{m_e}{m^*}. \tag{2.17}$$

The isotropic Bohr radius is 130 Å for $GeSb_2Te_4$ with an effective mass of 0.4 and a static dielectric constant of 98 [74]. This results in a critical charge-carrier concentration of $n_C = 8.0 \cdot 10^{15}$ cm^{-3}. The charge-carrier concentration determined by Hall measurements at the MIT is $2.0 \cdot 10^{20}$ cm^{-3}, which leads to a difference of more than a factor of 25,000. Such a strong deviation from the Mott criterion is not known in any other solid.

The degree of violation of the Mott criterion can be seen in figure 2.12. Edwards *et al.* [40] have shown the predictive power of the Mott criterion for a large range of materials. The criterion fails completely for $GeSb_2Te_4$ excluding electron correlation effects as the driving force of the observed MIT. The failure of an electron-electron interaction approach as an explanation for the MIT could be also understood from the energy criterion discussed above.

In section 2.2.3, the differences between Fermi energy, Coulomb energy, and mobility edge were considered as instruments to decide wether correlation or disorder is at play. These energies will be discussed now. In equation 2.4, the Coulomb energy depends on

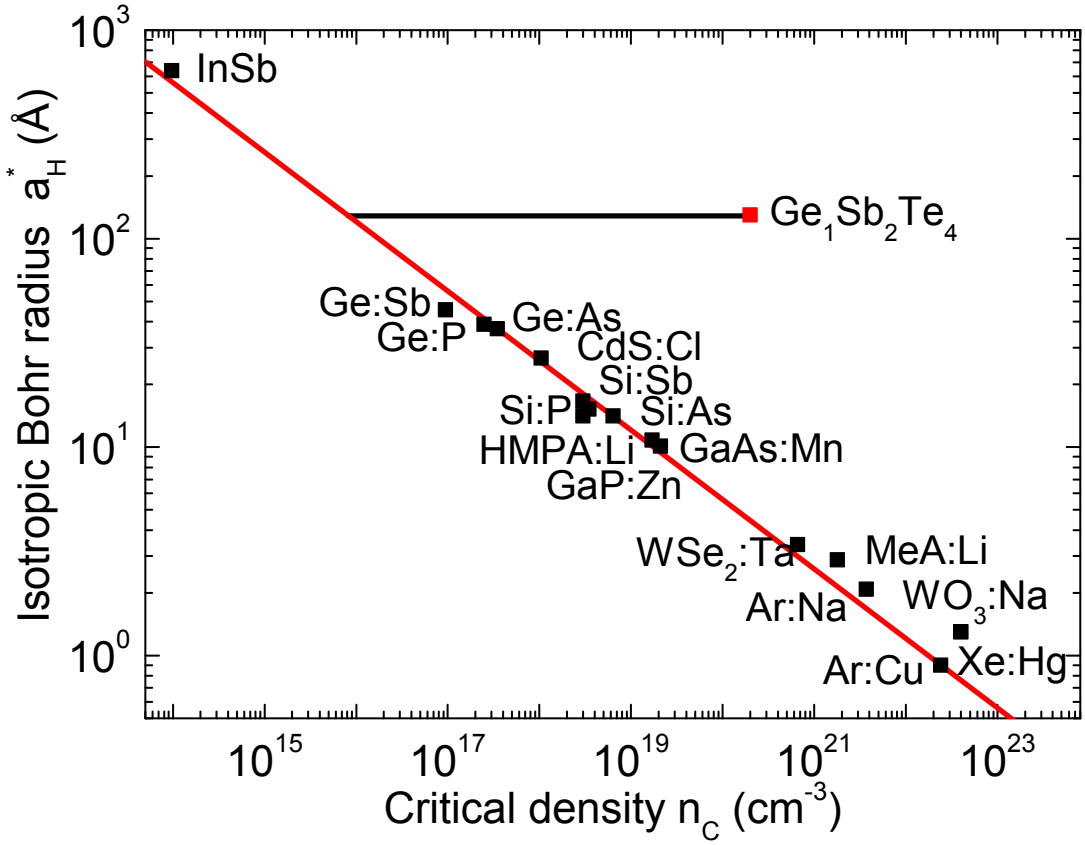

Figure 2.12.: The Mott criterion applied to $GeSb_2Te_4$. The Mott criterion ($n_C^{1/3} a_H^* = 0.26$) predicts the critical carrier density where doped semiconductors turn from insulating to metallic behavior. Data points to the left of the line are insulators, metals are to the right of the Mott line. The predictive power has been shown for many materials over a range of more than 8 orders of magnitude (redrawn from [75]). For $GeSb_2Te_4$ however the Mott criterion fails. Consequently, the MIT in $GeSb_2Te_4$ cannot be a classical Mott transition governed by electron-correlation effects.

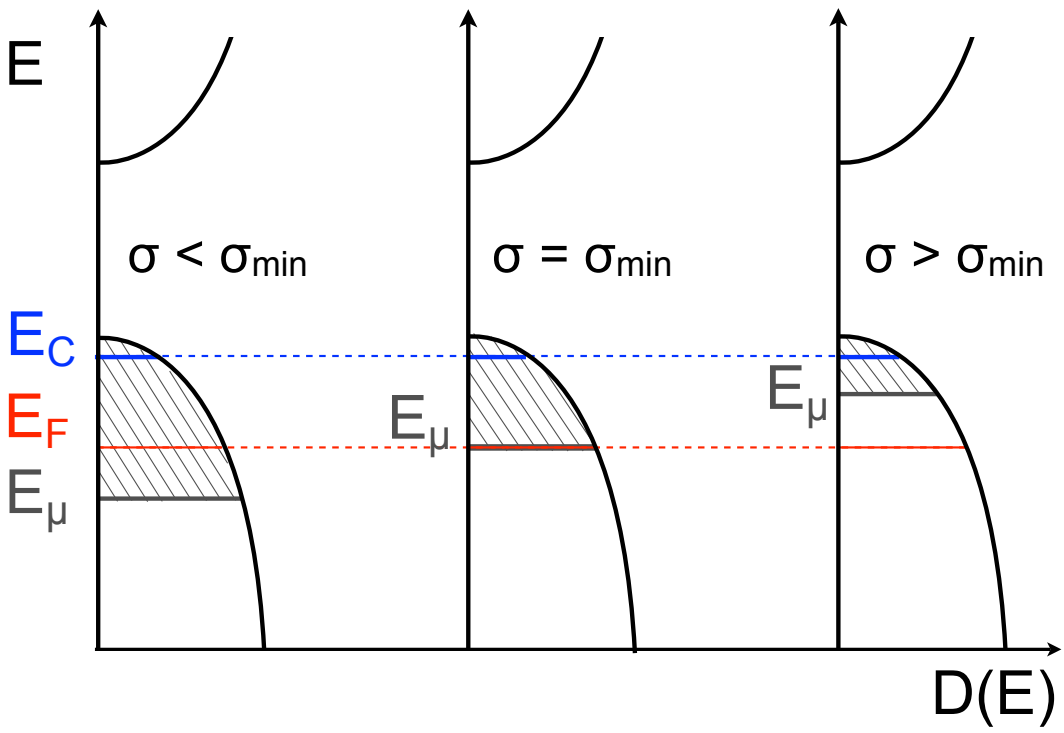

Figure 2.13.: Disorder induced localization: Energy scales and Density of states. As long as the Fermi energy E_F lies within the localized states (shaded regions) the system is insulating (left). With reduction of disorder due to annealing the mobility edge E_μ rises up to the Femi energy. At this point (centre) the 'Anderson like' transition to metallic behavior (right) occurs. The graph showing the Coulomb energy EC is designed so as to allow a comparison with E_F.

the charge-carrier density and the static dielectric constant, whereas the Fermi energy is calculated from the charge-carrier density and the effective mass. At the MIT, the values of table 2.1 lead to energies of E_F = 130 meV. The static dielectric constant of ϵ_{st} = 98 leads to a small value of the Coulomb energy of E_C = 8.6 meV. The origin of the large value for the static dielectric constant can be seen in the effective screening due resonant bonding in phase-change materials. As the Coulomb energy is much smaller than the Fermi energy, electron correlation effects can be excluded as origin of the MIT. Table 2.1 shows that all three parameters relevant for the Coulomb and Fermi energy (n, m^* and ϵ_{st}) are almost annealing independent. Thus for all annealing temperatures the Coulomb energy is much lower than the Fermi energy. This results in a situation for $GeSb_2Te_4$ that is compatible with the situation sketched in figure 2.13.

The origin of the MIT observed in $GeSb_2Te_4$ must be an intra-grain effect that is not governed by electron correlation. One pronounced difference between $GeSb_2Te_4$ and an ordinary sp^3 bonded semiconductor is the high degree of disorder. In the following the different aspects of disorder present in GeTe and $GeSb_2Te_4$ are discussed.

As seen in section 2.5, GeTe and $GeSb_2Te_4$ crystallize in a distorted NaCl phase. Te atoms form an initial fcc sub-lattice in the fast crystallization process [17, 18]. Due to the short time of the crystallization a randomly distributed occupation result on the other sub-lattice with Ge, Sb, and vacancies. Figure 2.14 sketches the bonding situation in $GeSb_2Te_4$ in a 2-dimensional cut. Tellurium occupies one sub-lattice of the NaCl structure. Germanium, Antimony, and empty lattices sites occupy the other sub-lattice, thus opening up multiple possibilities for disorder, as will be shown in the following. Ge, Sb, and vacancies are randomly distributed on the one sub-lattice in the simplest assumption of the $GeSb_2Te_4$ structure. The random occupation of the Ge/Sb/vacancy site will lead to different electronic potentials for the conduction electrons. Therefore it can be attributed to a diagonal Anderson localization. It is conceivable that some ordering mechanism of Ge, Sb, or vacancy will lead to a reduction of disorder within the sub-lattice, either with respect to themselves or to each other. This ordering process is very likely to start already within the NaCl-like phase. With the transition from the NaCl-like phase to the hexagonal phase the ordering of the empty lattice sites into layers has been completed to such an extent that the cubic symmetry is no longer maintained. A step-like ordering is not compatible with the continuously change in r_σ. As the transition is expected to be a continuous, it will not be completed at the point of the transition observed in the xrd diffraction pattern. Further ordering and

reduction of anti-sites between the Ge, Sb and vacancy layers will take place. These ordering processes would therefore reduce the diagonal Anderson localization. In literature such an ordering has already been discussed, but only with respect to the cubic-to-hexagonal transition [17].

Static displacements of individual atoms away from their ideal crystallographic positions is another possible disorder mechanism. A displacement of single atoms leads to a change of the transfer matrix element, and thus to an off-diagonal Anderson localization effect. In this situation the displacements could be lowered on annealing, which would lead to a reduction of disorder. A collective displacement of one sub-lattice with respect to the other, or else a displacement depending on the local enviroment of the atom are further options. A distortion of the cubic cell to a rhombohedral cell is also possible. However this would lead to additional peaks in the XRD diffraction pattern, for example a splitting of the (111) reflex. This is not observed in $GeSb_2Te_4$ and therefore limits this type of structural change to small distortions that would lead to a small peak broadening, rather than a splitting. A larger rhombohedral local distortions could be possible, if it would average out in the long range order and therefore would not be visible in the XRD measurements.

The bonding has a high degree of directionality due to resonant bonding via p-orbitals in crystalline phase change materials. The system is therefore very sensitive to changes in bond angles and lengths. In $GeSb_2Te_4$, the crystal structure undergoes small changes on annealing. These subtle changes will consequently affect in resonant bonding, resulting in changed electronic properties. We may therefore deduce that the pronounced disorder in $GeSb_2Te_4$ is the underlying cause of the observed MIT in $GeSb_2Te_4$. GeTe shows annealing independent metallic conduction it is, however, not far away from the MIT. The low values of r_σ shows that the conductivity of GeTe is influenced by disorder as well.

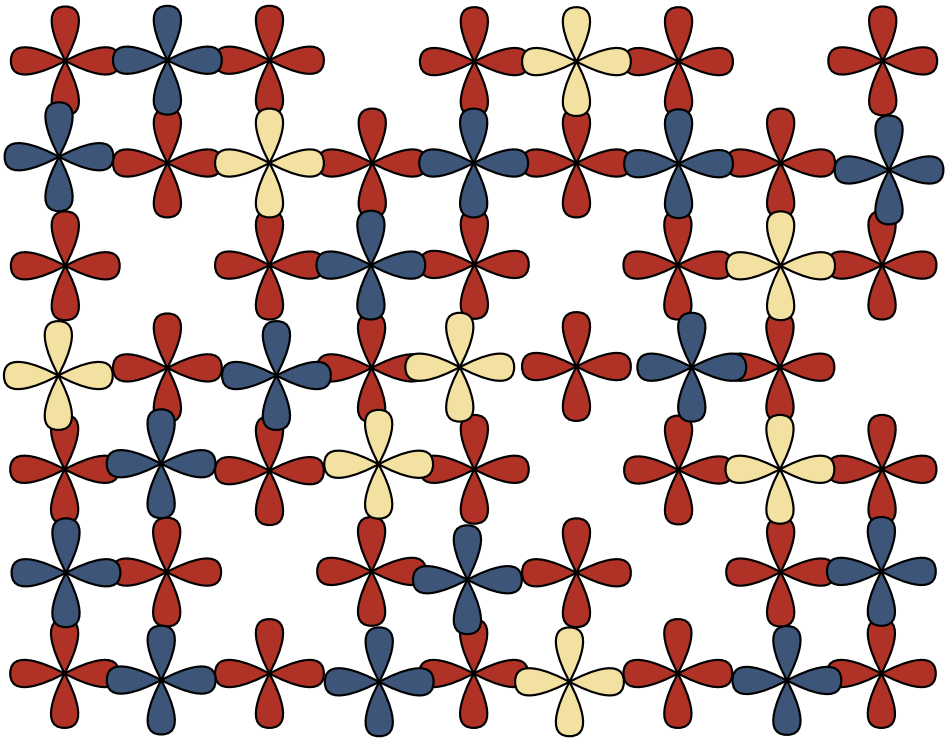

Figure 2.14.: Schematic presentation of the unique crystal structure and bonding situation in $GeSb_2Te_4$. Two-dimensional cut sketching the bonding situation in the rock-salt-like structure of $GeSb_2Te_4$. The anion sub-lattice is occupied with Te atoms (red) whereas the cation sub-lattice is randomly occupied with Ge atoms, Sb atoms (light yellow and blue, respectively) and empty lattice sites. It is evident that the random occupation in combination with distortions leads to tremendous variations of the atomic orbital overlap, thus giving rise to pronounced disorder-related effects on the band structure. These effects are reinforced by the strong directionality of the resonant p bonds, which makes the overlap more sensitive to distortions than in sp^3-bonded systems.

2.7. Conclusions

In this chapter the conduction mechanism of different phase-change materials has been studied. In phase-change materials like $GeSb_2Te_4$ the conductivity within the crystalline phase is strongly dependent on annealing. The room temperature value of the conductivity in crystalline $GeSb_2Te_4$ can be varied between 2.6 S/cm and 962 S/cm on annealing to temperatures between 150 °C and 325 °C. Not only does the conductivity itself vary, but the conduction mechanism also changes from a non-metallic to a metallic behavior (fig. 2.3). This metal-to-insulator transition (MIT) was verified for multiple phase-change materials on the pseudo-binary line (fig. 2.4). The critical minimum metallic resistivity observed for $GeSb_2Te_4$ turns out to be constant over a temperature range from 5 K to 600 K (fig. 2.5). The transport parameters derived from Hall, van der Pauw, and FTIR measurements support the observation of the MIT. These parameters exclude electron correlation (Mott) as the origin of the MIT. The characteristic bonding mechanism in crystalline phase-change materials - resonant bonding - leads to a high static dielectric constant. This results in an effective screening of the electron-electron interaction and thus correlation. Even though disorder is the dominating origin of the MIT, x-ray diffraction measurements do not give a clear hint which disorder is responsible. Therefore a more detailed analysis of the crystallographic phase of GeTe and $GeSb_2Te_4$ will be undertaken next, along with an analysis of the annealing dependent changes in the structure of $GeSb_2Te_4$.

CHAPTER 3

Crystallographic Analysis of Disorder

As described in the previous chapter 2, the conductivity of phase-change materials shows two different annealing dependencies. GeTe and $GeSb_2Te_4$ can be treated as prototype materials for these two behaviors. Both crystallize in a distorted rock salt like structure with GeTe showing an annealing independent metallic behavior, whereas $GeSb_2Te_4$ changes its conduction mechanism from non-metallic (insulating) to metallic on annealing. The difference in behavior is attributed to the larger degree of disorder in $GeSb_2Te_4$ compared to GeTe. The focus will now be set on the crystallographic differences of these two materials and the annealing dependent changes in $GeSb_2Te_4$.

3.1. Neutron Pair Distribution Function technique

A conventional scattering experiment, e.g. x-ray or neutron diffraction, seems a suitable means to analyze the crystal structure of solids. However, there are two reasons why such an approach is not likely to contribute significantly to the understanding of the metal insulator transition (MIT) observed in $GeSb_2Te_4$. Firstly, the grain sizes of crystalline phase-change materials are quite small. These small grain sizes lead to a broadening of the diffraction peaks, which hinders a detailed analysis. A small splitting of a peak, for example, is much harder to detect for a broad peak. Secondly, the origin of the disorder induced localization is expected to be a change in short to medium range order rather than in long range order[1], as a disorder induced localization of charge carriers will depend on

[1] In this study, the usage of the terms *short*, *medium* and *long* range order are defined by the following distances: *short* range order equals the nearest neighbor distance (r = 2.5 - 3.5 Å), *medium* range order extends up to

the local atomic arrangement. A change in long range order is not mandatory for this change in local arrangement. Moreover, experiments like x-ray diffraction only probe the average structure when analyzed with for instance the Rietveld [23] method. In addition Rietveld analyzes only the data at the position of the Bragg peaks. In contrast, neutron pair-distribution function (PDF) is a local probe analyzing both Bragg and diffuse components of the scattering together. For example displacements of single atoms that are not correlated would average out in XRD, but can be detected in a PDF analysis. For these reasons, the neutron PDF technique was chosen to study effects in the short to medium range order [76]. This local probing method has demonstrated its strength in analyzing the structure of complex materials such as nano-crystalline materials and nano-particles. With grain sizes below 20 nm and local distortions, phase-change materials seem to be a material class well suited for this method probing in a range of up to 50 Å
around an average atom.

3.1.1. Diffraction by disordered systems

In the following section, the diffraction of neutrons by disordered systems will be presented in a generalized formalism for both neutron and x-ray diffraction. The scattering centers will be treated as point-like. The results can, however, be generalized for the case of extended scattering centers by superimposing the extended scattering centers at each point of the point-like scattering centers. The formalism presented here is adapted from [77].

The incident beam is considered as monochromatic, and the distance from the source is assumed large enough to treat the incident beam as plane waves. For the incident amplitude at the point $\vec{r}$ this results in

$$\Psi_{inc} = \psi_{inc} e^{i[\vec{k}_0 \cdot \vec{r} - \omega_0 t]} = \psi_0(t)\, e^{i\vec{k}_0 \cdot \vec{r}} \tag{3.1}$$

where $\vec{k}_0$ is the incident wave vector of magnitude $k_0 = 2\pi/\lambda_0$. The scattering is treated elastically. Thus the incident and diffracted wavelength are the same, and multiple scattering is not taken into account. This is often referred to as kinematic approximation. For a single scattering center i at the origin of the coordinates, the scattered wave is a spherical wave

$$\Psi_{scatt,1} = \frac{-\psi_o b_i}{R} e^{i k_f R}, \tag{3.2}$$

where k_f is the magnitude of the final wave vector $\vec{k}_f$, and R the distance from the scattering center. The time dependency of the incident and the scattered wave has been factored out

the cubic lattice constant (r = 3.5 - 6 Å) and whatever exceeds (r > 6 Å) is called *long* range order.

and incorporated into the ψ_0 term. The constant b_i is the scattering length in the case of neutrons or the atomic form factor in the case of x-rays for scattering center i. As x-rays scatter from the extended electron cloud of an atom which is in the same dimension as the wavelength of the x-rays, the atomic form factor is dependent on the scattering angle. Neutrons scatter at the atomic nucleus, which is five orders of magnitude smaller than the wavelength. Therefore neutron scattering at the nucleus can be treated as point like scattering. The scattering length for neutrons is a dimensionless length, and is in general a complex value. The magnitude and the sign of b_i depend on the properties of the interaction between the scattering center and the scattered quantum. It is possible to distinguish two types of nucleus from their scattering behavior. For the first type the scattering length is complex and dependends on the neutron energy. For those nuclei the scattering is associated with the formation of a compound nucleus, consisting of the original nucleus and the neutron, with energies close to an excited state. Examples of nuclei of this type are ^{103}Rh, ^{113}Cd, ^{157}Gd, and ^{176}Lu [78]. The imaginary part of the scattering lengths materials of this type is large, corresponding to an absorption of neutrons. The majority of nuclei belong to the second type of nuclei. For those the absorption and therefore the imaginary part of the scattering length is small and the real part is mainly independent of the neutron energy. The materials investigated in this study, Ge, Sb, and Te have coherent scattering length of 8.185 fm, 5.71 fm, and 5.8 fm, respectively. Only ^{73}Ge has a non neglectable incoherent scattering length, but ^{73}Ge has only a natural abundance of 7.8 %. Therefore in the following the scattering length will be treated to be a real quantity. By convention, the scattering length is positive for a repulsive scattering potential in neutron scattering. This results in the negative sign in equation 3.2.

For scattering centers at a position $\vec{r}_i$ instead of at the origin, an additional phase shift of $\vec{q}\cdot\vec{r}_i$ can be deduced, where $\vec{q} = \vec{k}_0 - \vec{k}_f$ is called the wave vector transfer. This is valid for $R \gg r_i$. The scattered wave of a sample comprising N point-like scattering centers i with scattering lengths b_i is given by

$$\Psi_{scatt,N} = \frac{-\psi_0}{R} \mathrm{e}^{ik_f R} \sum_{i=1}^{N} b_i \mathrm{e}^{i\vec{q}\cdot\vec{r}_i} \tag{3.3}$$

at a distance $\vec{R}$ parallel to $\vec{k}_f$. At the distance R, a detector is placed with an area $\mathrm{d}S \ll R^2$ covering a small solid angle $\mathrm{d}\Omega = \mathrm{d}S/R^2$ with respect to the sample.

The differential scattering cross-section is defined by

$$\frac{\mathrm{d}\sigma}{\mathrm{d}\Omega} \stackrel{\text{def}}{=} \frac{\text{number of quanta scattered per second towards the detector into } \mathrm{d}\Omega}{\Phi \mathrm{d}\Omega}, \tag{3.4}$$

with the incident flux Φ. With $\mathrm{cm}^{-2}\mathrm{s}^{-1}$ being the unit for the flux and steradian (str) for $\mathrm{d}\Omega$, the unit of $\mathrm{d}\sigma/\mathrm{d}\Omega$ becomes $\mathrm{cm}^2/\mathrm{str}$. Instead often the unit barn/str is used, with 1 brn = 10^{-24} cm^2. For a single scattering center at the origin the differential scattering cross section can be written as:

$$\left.\frac{\mathrm{d}\sigma}{\mathrm{d}\Omega}\right|_1 = \frac{|\Psi_{scatt,1}|^2\,\mathrm{d}S}{|\Psi_{inc}|^2\,\mathrm{d}\Omega} = \frac{(\psi_0^2|b_i|^2/R^2)(R^2\mathrm{d}\Omega)}{\psi_0^2\mathrm{d}\Omega} = |b_i|^2 \qquad \text{or} \qquad b_i^2. \tag{3.5}$$

The result is as expected isotropic scattering. For a sample with N scattering centers the differential scattering cross section becomes

$$\frac{\mathrm{d}\sigma}{\mathrm{d}\Omega}(\vec{q}) = \overline{\left\langle \left| \sum_{i=1}^{N} b_i \mathrm{e}^{i\vec{q}\cdot\vec{r}_i} \right|^2 \right\rangle} = \left\langle \left| \sum_{i,j}^{N} \overline{b_i b_j^*} \mathrm{e}^{i\vec{q}\cdot\vec{r}_{ij}} \right|^2 \right\rangle \tag{3.6}$$

with $\vec{r}_{ij} = \vec{r}_i - \vec{r}_j$ being the vector for the relative position of scattering centers i and j. The brackets $\langle\rangle$ denote a thermal average, as the positions of the scattering centers are not fixed over time due to thermal motion.

The intensity $I(\vec{q})$ measured in counts-per-seconds by the detector for a solid angle $\mathrm{d}\Omega$ can be derived from equation 3.4 to

$$I(\vec{q}) = \Phi \frac{\mathrm{d}\sigma}{\mathrm{d}\Omega}(\vec{q})\,\mathrm{d}\Omega \tag{3.7}$$

The measured intensity is only dependent on the wave vector transfer $\vec{q}$. As $\vec{q}$ is dependent on both the wavelength λ and the detector angle θ by

$$q = 2k_0\,\sin\theta = \frac{4\pi}{\lambda_0}\sin\theta, \tag{3.8}$$

one can either vary the wavelength λ, the scattering angle θ or both to measure a diffractogram.

We will now consider the scattering by a monoatomic sample and derive the structure factor $S(\vec{q})$ for it. We will see, that is it possible to decompose the differential scattering cross section into different parts. Two different ways will be presented in the following. In the first, the introduction of the interference function $H(\vec{q})$ will lead to a distinct part, which is correlated to the interference between different atomic sites and a self part, containing the isotropic scattering from single sites. The second, more commonly route, is to decompose the scattering into a coherent and an incoherent part. This is done by introducing the structure factor $S(\vec{q})$. It will be seen that both the interference function $H(\vec{q})$ and the structure factor $S(\vec{q})$ contain the same physical information. We will see as well, that

these function are independent of the radiation type used for the scattering and are only dependent on the atomic structure of the material under investigation.

A monoatomic sample consist of different isotopes due to the natural abundance of elements. As neutron scatter at the nucleus, the scattering length depends on the isotope. For a monoatomic system one, therefore, has to calculate the weighted average of the different scattering lengths with the natural abundance as weight. We will assume no correlation between the scattering lengths and the position of different scattering centers. The average scattering length can then be calculated as

$$\overline{b} = \sum_i c_i b^i \tag{3.9}$$

and

$$\overline{|b|^2} = \sum_i c_i \left| b^i \right|^2 \tag{3.10}$$

with $c_i = N_i / N$ the concentration of the isotop i. The average in equation 3.6 can thus be calculated as

$$\begin{aligned}
\overline{b_i b_j^*} &= \left|\overline{b}\right|^2 (1-\delta_{ij}) + \overline{b}^2 \delta_{ij} && (3.11)\\
&= \left|\overline{b}\right|^2 + \left(\overline{|b|^2} - \left|\overline{b}\right|^2\right)\delta_{ij} && (3.12)\\
&= \left|\overline{b}\right|^2 + \overline{\left|b-\overline{b}\right|^2}\delta_{ij} && (3.13)
\end{aligned}$$

Therefore we can consider two cases for each term in the summation of equation 3.6:

$$\begin{aligned}
\overline{b_i b_j^*} &= \overline{b_i b_i^*} = \overline{b^2} && i = j \text{ (same site)}, && (3.14)\\
\overline{b_i b_j^*} &= \overline{b_i b_j^*} = \overline{b}^2 && i \neq j \text{ (different site)}, && (3.15)
\end{aligned}$$

leading to a differential scattering cross section of

$$\begin{aligned}
\frac{\mathrm{d}\sigma}{\mathrm{d}\Omega}(\vec{q}) &= \overline{b}^2 \left\langle \sum_{i,j\neq i}^{N} \mathrm{e}^{i\vec{q}\cdot\vec{r}_{ij}} \right\rangle + N\overline{b^2} && (3.16)\\
&= \overline{b}^2 \left\langle \sum_{i,j}^{N} \mathrm{e}^{i\vec{q}\cdot\vec{r}_{ij}} \right\rangle + N\left(\overline{b^2} - \overline{b}^2\right)
\end{aligned}$$

The differential cross section is separated in the first line of the equation into a 'distinct' term for the diffraction interference from different atomic sites and a 'self' term for the isotropic

diffraction from individual atomic sites. By introducing the dimensionless interference function $H(\vec{q})$ as

$$H(\vec{q}) \stackrel{\text{def}}{=} \frac{1}{N}\left\langle \sum_{i,j\neq i}^{N} \mathrm{e}^{i\vec{q}\cdot\vec{r}_{ij}} \right\rangle \tag{3.17}$$

which for a disordered system is converging to 0 for $q \to \infty$, one can write the differential scattering cross section per atom as

$$\begin{aligned} \frac{1}{N}\left[\frac{\mathrm{d}\sigma}{\mathrm{d}\Omega}(\vec{q})\right] &= \frac{1}{N}\left[\frac{\mathrm{d}\sigma}{\mathrm{d}\Omega}(\vec{q})\right]^{\text{distinct}} + \frac{1}{N}\left[\frac{\mathrm{d}\sigma}{\mathrm{d}\Omega}(\vec{q})\right]^{\text{self}} \\ &= \overline{b}^2 H(\vec{q}) + \overline{b^2}. \end{aligned} \tag{3.18}$$

This equation explicitly shows that the differential scattering cross section is only dependent on $\vec{q}$.

Another route, which is more commonly used, is to decompose $\mathrm{d}\sigma/\mathrm{d}\Omega$ into a coherent and an incoherent part. This separation is already be done in equation 3.16, second line. The coherent part takes diffraction from all atomic sites into account. This includes self scattering from a single atom and is independent of the distribution in scattering lengths. In contrast the incoherent part depends only on the distribution of scattering lengths present in the sample and is independent of the spatial correlation of the atomic sites. It therefore leads to an isotropic diffraction. The coherent and incoherent scattering lengths are thereby defined as

$$b_{\text{coh}} \stackrel{\text{def}}{=} \overline{b} \qquad \text{and} \qquad b_{\text{incoh}}^2 \stackrel{\text{def}}{=} \left(\overline{b^2} - \overline{b}^2\right) = \overline{\left|b - \overline{b}\right|^2}. \tag{3.19}$$

The coherent scattering length is defined as the average and the incoherent as the standard deviation of the sample's scattering length distribution. Values of b_{coh} and b_{incoh} for both natural isotopic compositions and single isotopes are given in [79].

The structure factor $S(\vec{q})$ is introduced as

$$S(\vec{q}) \stackrel{\text{def}}{=} \frac{1}{N}\left\langle \sum_{i,j}^{N} \mathrm{e}^{\mathrm{i}\vec{q}\cdot\vec{r}_{ij}} \right\rangle = H(\vec{q}) + 1. \tag{3.20}$$

It is dimensionless and converges to 1 for $\vec{q} \to \infty$. The differential scattering cross section per atom can be rewritten with the structure factor for a monoatomic system:

$$\begin{aligned} \frac{1}{N}\left[\frac{\mathrm{d}\sigma}{\mathrm{d}\Omega}(\vec{q})\right] &= \frac{1}{N}\left[\frac{\mathrm{d}\sigma}{\mathrm{d}\Omega}(\vec{q})\right]^{\text{coh}} + \frac{1}{N}\left[\frac{\mathrm{d}\sigma}{\mathrm{d}\Omega}(\vec{q})\right]^{\text{incoh}} \\ &= \overline{b}^2\, S(\vec{q}) + \left(\overline{b^2} - \overline{b}^2\right) \\ &= b_{\text{coh}}^2\, S(\vec{q}) + b_{\text{incoh}}^2 \end{aligned} \tag{3.21}$$

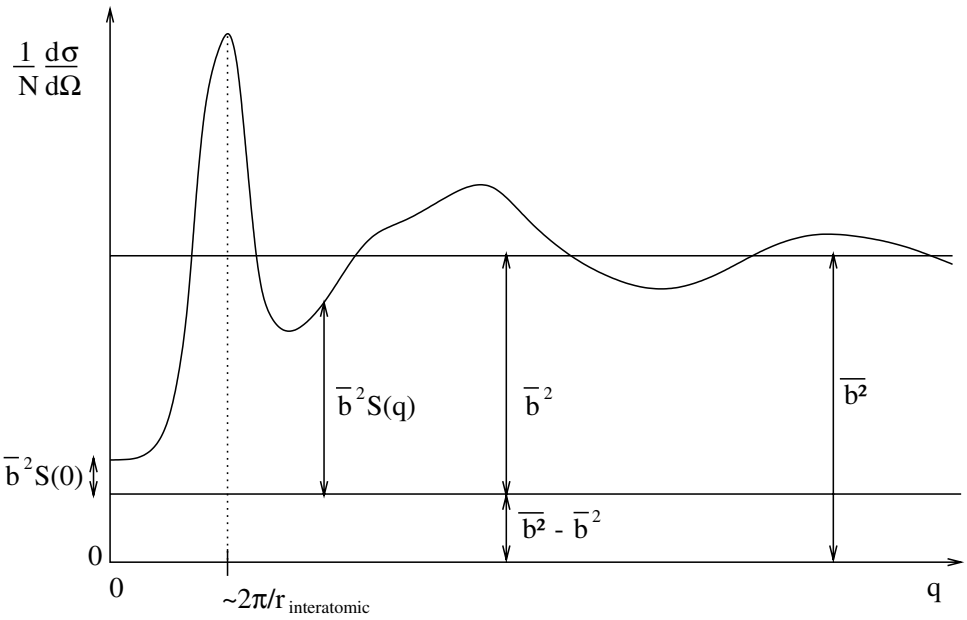

Figure 3.1.: Differential scattering cross section per atom for a monoatomic system. Different quantities that are directly linked to the shape of the differential scattering cross section per atom $(1/N)\ \mathrm{d}\sigma/\mathrm{d}\Omega = \overline{b}^2 S(\vec{q})n + (\overline{b^2} - \overline{b}^2)$ are marked. The interatomic distance $r_{\text{interatomic}}$ can be calculated from the position of the first peak. Taken from [77].

From this equation it can be seen that in the differential cross section per atom only the coherent scattered quanta show a dependency on $\vec{q}$, while the incoherent scattered quanta are isotropic.

3.1.2. Pair distribution function

After deriving the structure factor $S(q)$, a function in reciprocal-space, the focus will now lie on the pair-distribution function (PDF), a real-space function. It describes how many other atoms are located around an average atom and at what distances they are located. Three different real-space functions often associated with PDF are plotted in figure 3.2. They all can be calculated via a Fourier transformation of the measured total structure factor S(q). They differ by the pre-factors. The pair-distribution function g(r) and the structure factor

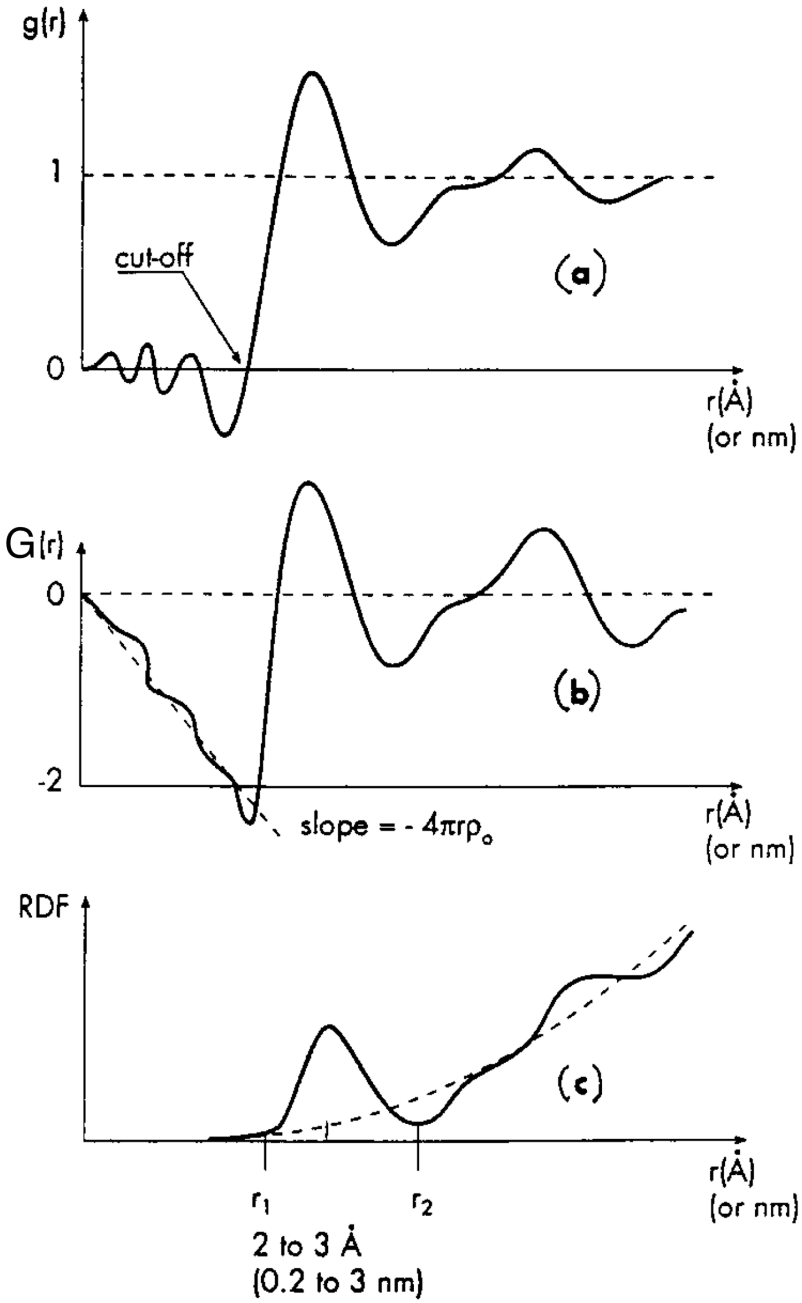

Figure 3.2.: Examples of real-space functions. From top to bottom: (a) pair-distribution function g(r), (b) pair-distribution function G(r) and (c) radial distribution function RDF(r). The different functions can be transformed into each other by changing the pre-factor. Therefore the physical information encoded in the three functions is the same. Due to the different pre-factors the weighting is different. In the g(r) function small distances are weighted more than in the function G(r). In the Radial distribution function RDF(r) the integral from r_1 to r_2 gives the absolut number of atoms between these two distances. Figure adapted from [80]

S(q) are transformed into each other by

$$S(q) - 1 = \frac{4\pi\rho_0}{q} \int_0^\infty r\,[g(r) - 1] \sin(qr)\, dr \tag{3.22}$$

$$g(r) - 1 = \frac{1}{2\pi^2 r \rho_0} \int_0^\infty q\,[S(q) - 1] \sin(qr)\, dq, \tag{3.23}$$

with ρ_0 being the density, q the momentum transfer, and r the distance. The pair-distribution function G(r) is defined as

$$G(r) = 4\pi r\, \rho_0\, [g(r) - 1] = \frac{2}{\pi} \int_0^\infty q\,[S(q) - 1] \sin(qr)\, dq. \tag{3.24}$$

This definition explains why in figure 3.2 the slope for r-values below the inter-atomic distance is proportional to the density. The radial distribution function can be calculated as follows

$$\mathrm{RDF}(r) = 4\pi r^2\, \rho_0\;\, g(r). \tag{3.25}$$

Both the slope and the damping of the oscillations are different for g(r), G(r), and RDF(r), but the information that can be gathered from them is the same. The g(r) function shows small oscillations around zero below the minimum bonding length (r_1). At values higher than r_1 the oscillations are associated with neighboring atoms. For $r \to \infty$ the value of g(r) converges to one. G(r), however, has a negative slope proportional to the density below r_1. The oscillations for $r > r_1$ vanish slower than the oscillations of g(r) and converge to zero. The radial distribution function RDF(r) increases proportionally to r^2, as it is proportional to the absolute number of neighboring atoms found at a distance r.

3.2. Beamline D4 at Institut Laue-Langevin, Grenoble

The Institut Laue-Langevin[2] (ILL) in Grenoble, France, is an international research center. Its high-flux reactor provides the most intense continuous neutron flux ($1.5 \cdot 10^{15}$ n/(s cm^2)) in the world. The ILL provides beam-time to visiting scientists at 40 different beamlines.

The data analyzed in this study were taken under the proposal No. 6-05-839 at beamline D4. This beamline is optimized for measuring non-crystalline and nano-crystalline materials in detail. A large Q-range and a stable and low background are essential for successful measuring. A sketch of the diffractometer is shown in figure 3.3. D4 is a two-axis diffractometer using short-wavelength neutrons from the hot source. The neutrons are being

[2] http://www.ill.eu

monochromated with a Cu single crystal monochromator. The monochromated beam is collimated, and slits ensure that only the cylindrical sample is illuminated. The detector bank is mounted around the sample with 9 position sensitive detectors. Gaps in between the detector are not covered due to the geometry of the detectors. Therefore the entire detector bank has to be moved around the sample to cover those gaps and to obtain a complete diffraction pattern. For the experiments in this thesis a wavelength of 0.5 Å was chosen because this wavelength allows a Q-range of up to 25 $Å^{-1}$.

3.2.1. Sample geometry, data treatment, and data analysis

The samples were prepared by sputtering from a compound target with the desired stoichiometry. After sputtering, the films were scratched off the glass substrates and filled into thin walled silica capillaries. This procedure yielded cylindrical samples with a diameter of 2 mm and a height of about 60 mm. The total sample mass in the beam was 250 - 300 mg. Only 20 mg of the sample container were enclosed in the beam as the wall thickness was just 0.01 mm. This excellent ratio of sample to container mass facilitates subsequent processing of the data.

Still, it requires some effort to obtain a structure factor that contains no more than the sample itself. Fischer *et al.* [77] offer an excellent introduction to the underlying theory and to the treatment of the data in their review paper. Further measurements were needed in order to subtract the background and for normalization: empty instrument, empty sample container, a known Nickel and a known Vanadium sample. Nickel was used to calibrate the wavelength and Vanadium was used to normalize the diffraction intensities to a known scattering cross section. Vanadium has the advantage of an almost completely incoherent and therefore isotropic cross section [77].

For multiple scattering and absorption correction of the data, the following sample parameters are necessary: stoichiometry, density, packing fraction, and Hydrogen concentration within the sample. Density was taken from X-ray reflectivity measurements (XRR). The packing fraction was calculated from the sample mass, its density, and the measured volume. The Hydrogen concentration was adjusted by fitting the Placzek falloff. This falloff is very strong for light atoms like H because of their to the strong inelastic scattering. This effect is shown in Figure 5 of [77] for light water (H_2O), heavy water (D_2O), and a 1 : 1 mixture of both. For the different samples, the H concentration was 1.6 % and 2.6 % for GeTe and $GeSb_2Te_4$, respectively. With these parameters and with the help of the program

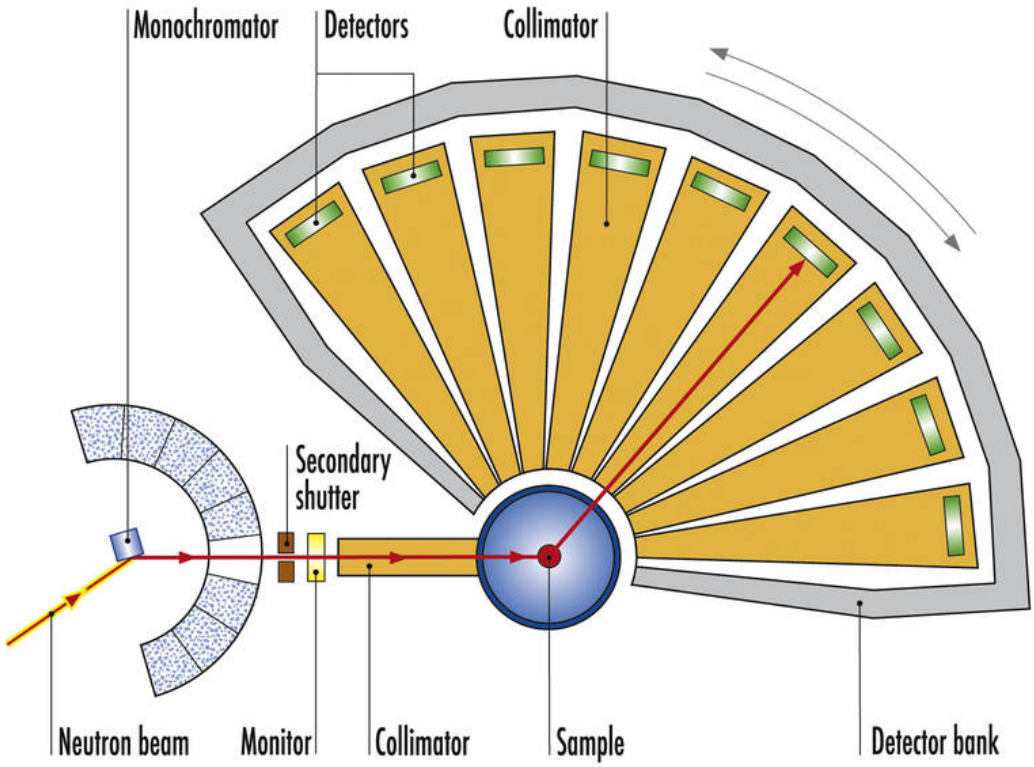

Figure 3.3.: Instrument D4 at Institut Laue-Langevin. D4, a two-axis diffractometer, uses short-wavelength neutrons from the hot source and measures diffraction patterns over a large Q-range. This feature allows characterization of local atomic order of non-crystalline and nano-crystalline materials with excellent accuracy. The gaps in between the large array of microstrip detectors make it necessary to move the detector bank during the measurement so as to cover these gaps. Adapted from [81]

package *correct* from the ILL, the total structure factors S(q) were calculated. The structure factors and pair-distribution functions of GeTe and $GeSb_2Te_4$, annealed at 225°C and 150°C respectively, are displayed in figure 3.4.

As within the framework of this thesis the short to medium range order is of interest, the real space pair-distribution function G(r) needs to be calculated from the structure factor S(q). The data have therefore to be Fourier transformed (see 3.22). A comparison of the total structure factor S(q) and the resulting total pair-distribution function G(r) is given in figure 3.4.

The data are Fourier transformed up to a maximum value q_{max}. This value is correlated to the resolution of the pair-distribution function G(r). The minimum peak width in the G(r) scales with $2\pi/q_{max}$. Fourier transforming the data only to the first peak in S(q) results in a sine function in G(r). The peak broadening leads to a damping of this sine with higher r-values. Every peak in S(q) leads to a sine in the G(r), and therefore the G(r) is composed of a superposition of these different damped sine functions. Figure 3.5 shows the evolution of G(r) with an increasing value of q_{max} for GeTe. At first only one sine is visible, but with extended q-range more and more structure can be seen in the pair distribution function G(r). For example, the 3+3-type splitting of the nearest neighbor at 3 Å is only visible at high q_{max} values.

The peak width σ_{ij} of a single G(r) peak contains contributions from thermal and zero point displacement as well as from static displacement. The isotropic thermal displacement u_{iso} of the atoms leads to a width σ'_{ij}. The correlation of the atomic motion of two different atoms is highly dependent on their distance. The motion is uncorrelated for large distances r, but a strong correlated motion is expected for small distances r. This correlation leads to a sharpening of the first peak(s) in the PDF. The final width σ_{ij} is modeled by two parameters, δ_2 and Q_{broad}

$$\sigma_{ij} = \sigma'_{ij}\sqrt{1 - \frac{\delta_2}{r_{ij}^2} + Q_{broad}^2 r_{ij}^2}. \tag{3.26}$$

The correlated motion of neighboring atoms is corrected by the parameter δ_2, the peak broadening caused by the finite q resolution of the diffractometer is corrected by Q_{broad}.

Limited q resolution of the diffractometer also results in an exponential dampening of the PDF peak height $B(r)$. This dampening envelope is modeled by the parameter Q_{damp} of the form

$$B(r) = \mathrm{e}^{-\frac{(r\ Q_{damp})^2}{2}}. \tag{3.27}$$

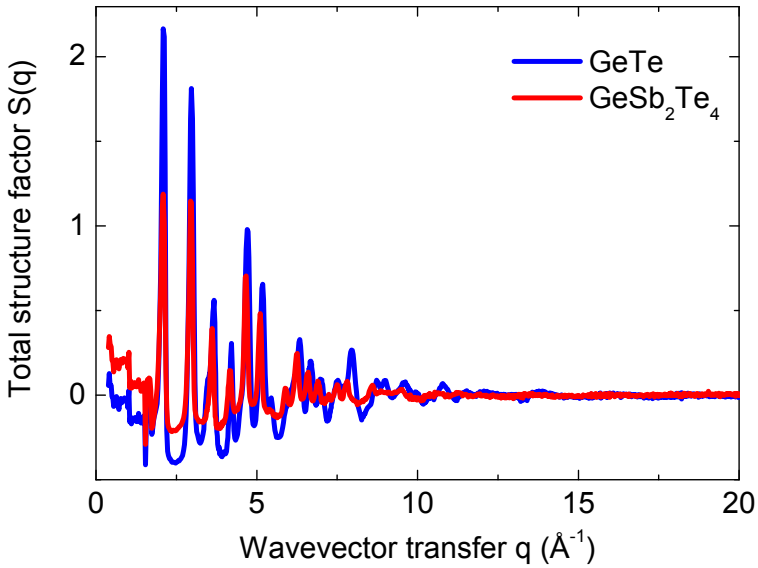

(a)

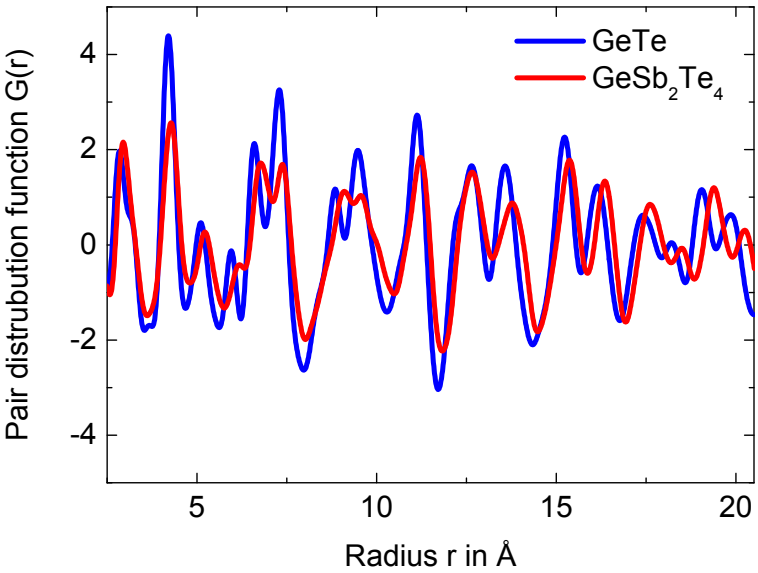

(b)

Figure 3.4.: Total structure factor and pair-distribution function of crystalline GeTe and $GeSb_2Te_4$. (a) Total structure factor S(q) of GeTe and $GeSb_2Te_4$. The Bragg peaks are broadened because of the the finite q-resolution of the diffractometer D4. By Fourier transforming from the reciprocal space to real space one obtains the pair distribution function G(r) **(b)**. Data was collected on beamline D4 at the Institut Laue-Langevin with neutrons with a wavelength $\lambda = 0.5$ Å. The annealing temperatures were 225 °C for GeTe and 150 °C for $GeSb_2Te_4$.

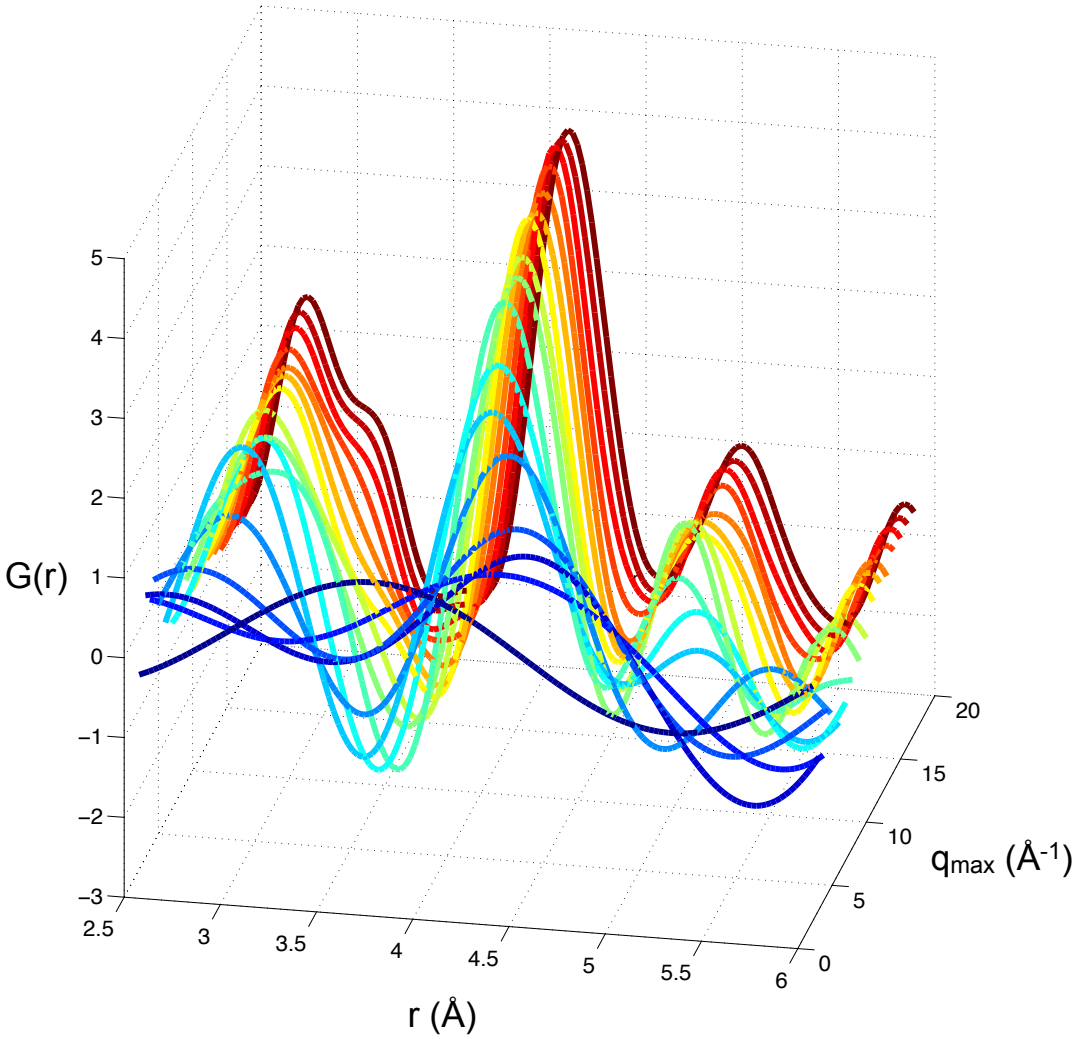

Figure 3.5.: Evolution of the pair distribution function G(r) with increasing q_{max}. To illustrate the effect of an increasing maximum wave vector transfer q_{max}, the total structure factor S(q) of GeTe is Fourier transformed with different values of q_{max}. For low q_{max} values, the G(r) is composed only of one sine. With every Bragg peak in the S(q) that contributes to the G(r) one more sine is added. This leads to a beating of many sines. At high q_{max} values, the first peak at 3 Å develops into a double peak.

3.3. Modeling of the short to medium range order in phase-change materials

In the following section, the total pair-distribution G(r) of GeTe and $GeSb_2Te_4$ will be analyzed with respect to the short to medium range order. As in chapter 2, GeTe acts as a reference phase-change material. The program package PDFgui was used to perform fits to the G(r) so as to model the structure of the short-to-medium range order. PDFgui is a graphical user interface to the program package PDFfit2. The programs were developed by Farrow *et al.* [82]. The aim of PDFgui is real-space refinement of crystal structures, without imposing symmetry, based on pair-distribution functions. The basic input values are box dimensions and fractional coordinates of atoms placed in a box that is continued with periodic boundary conditions.

As for both GeTe and $GeSb_2Te_4$ a distorted NaCl-like structure is assumed [17, 21, 22, 83], a rhombohedral unit cell was chosen as a box with one Te atom at (0, 0, 0) and a Ge/Sb/vacancy at (0.5, 0.5, 0.5). A rhombohedral cell resembles an NaCl structure at a rhombohedral angle α of 60°. Therefore it has the advantage to be valid for both an NaCl structure and, of course, a rhombohedral structure. Figure 3.7 shows the resemblance of the rhombohedral cell to an NaCl cell. The main fitting parameters in this model are the rhombohedral lattice parameters (lattice constant a and angle α) and a static atomic displacement of the Ge/Sb site along the [1 1 1] direction, referred to as **A**tomic **D**isplacement **P**arameter (ADP). From long range order measurements it is known that GeTe shows a Peierls-like 3+3-type splitting of the nearest neighbors into three shorter and three longer bonds. This splitting can be modeled successfully with the ADP parameter along [1 1 1].

If we fit a rhombohedral cell to the short and medium range order, both alone and combined, we may compare the results gained for those two regions. We may also compare the results with the values obtained from measurements of the long range order.

To visualize the effects of a change in the rhombohedral model on the G(r), a GeTe rhombohedral structure is taken to simulate the corresponding G(r) (figure 3.6). Two parameters are varied, the rhombohedral angle α and the atomic displacement along [1 1 1]. The lowering of the rhombohedral angle α yields a shortening of some Te-Te bonds to lower values. The shortened Te-Te distance is plotted as a dotted line in the schematics in figure 3.6. As not all Te-Te distances change on rhombohedral distortion, a shoulder of the peak at the undistorted position is visible. A displacement of the Ge site along [1 1 1] (ADP) results in

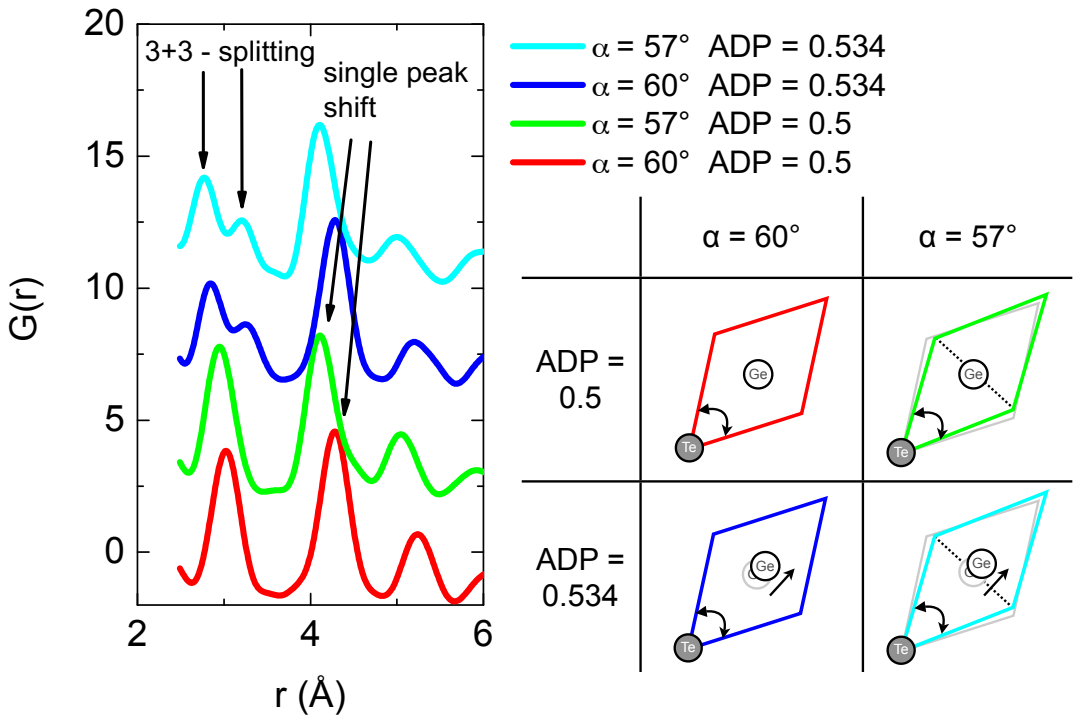

Figure 3.6.: Effects of rhombohedral distortion and atomic displacement on the pair distribution function G(r). To study the effects of a change in rhombohedral angle α and the atomic displacement along [1 1 1] (ADP) pair distribution functions G(r) are plotted for different values of α and ADP. The starting point is the undistorted rhombohedral angle $\alpha = 60\ ^\circ$ and an atomic displacement of ADP = 0.5. A change in angle α leads to a shift of the peak around 4.2 Å. This is due to a shortening of the Te-Te distance indicated by the dotted line. Displacing the Ge atom along [1 1 1] leads to a splitting of the 6 nearest neighbor distances into three shorter and three longer ones. This can be seen in the splitting of the first peak.

a splitting of the first peak into a double peak. The six nearest neighbors of Ge change on displacement to three shorter and three longer bonds. A combination of a rhombohedral distortion of α = 57° and an atomic displacement of APD = 0.534 enhances the 3+3-type splitting.

3.4. Structure of GeTe

We know from x-ray diffraction measurements of the long range order that GeTe crystallizes into a rhombohedral α phase. Goldak *et al.* [21] have determined the lattice parameters to a = 4.240 Å, α = 58.8° with an atomic displacement along [1 1 1] ADP = 0.526. More recent measurements determined the lattice parameters to a = 4.281 Å, α = 58.30° and ADP = 0.52 [22][83]. These measurements differ in sample preparation: Goldak *et al.* [21] used mixed stoichiometric powder with subsequent melting, whereas [22] and [83] used powder from sputtered samples. The samples for this study were prepared by sputtering, so their values are expected to be closer to [22] and [83] .

To test the validity of the rhombohedral model of the short to medium range order in GeTe, fits with different r-ranges were performed. Three different fitting ranges were selected, whole range (r = 2.5 - 20-5 Å), short to medium range (r = 2.5 - 6 Å), and long range order (r = 6 - 20.5 Å). Fitting only the short range (r = 2.5 - 3.6 Å) order was possible, but the errors increased by another order of magnitude compared to the short to medium range.

The resulting parameters are listed in table 3.1. In figures 3.8 and 3.9 data, fits, and the corresponding residuum are plotted for the whole range and the short to medium range respectively. The values determined for the different r-ranges differ only within their error margin. The static displacement of the Te within the rhombohedral cell along [1 1 1] leads to a Peierls-like splitting of the octahedral bonded atoms in three shorter (2.83 Å) and three longer (3.19 Å) bonds. This splitting is visible in figure 3.9 showing the short to medium range fit of GeTe. A double peak is visible around 3 Å confirming the well-ordered displacement in GeTe. These values are also compatible with the literature values determined for the long range order. It may be concluded that the structure of GeTe can appropriately be described with a rhombohedral model and a static displacement along the [1 1 1] direction. This model holds for the short, the medium, and the long range order.

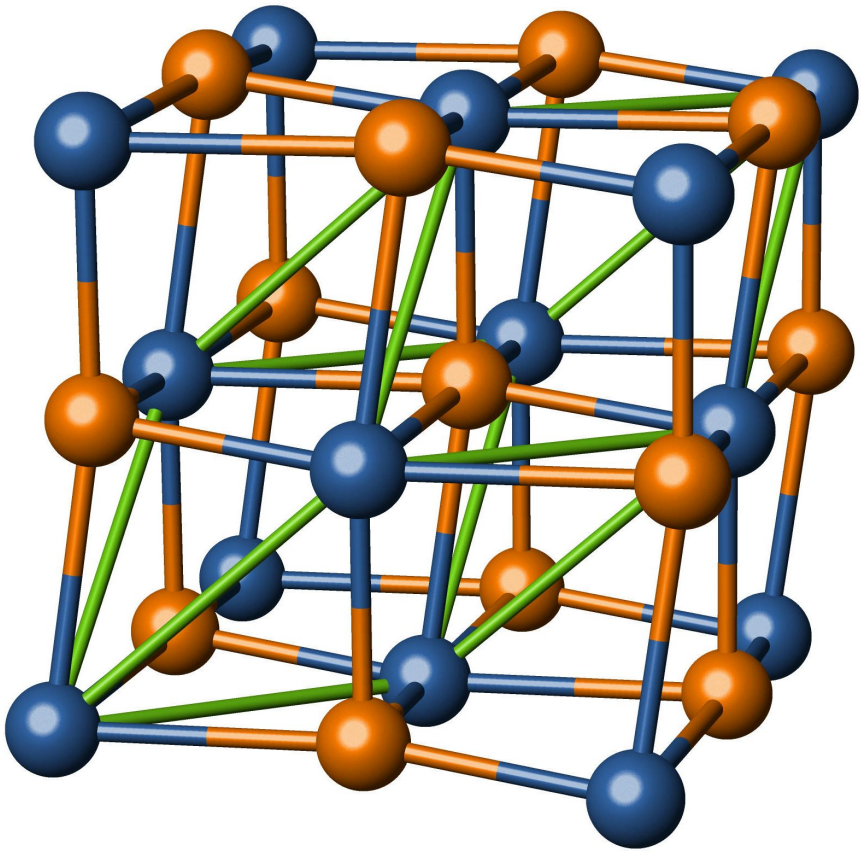

Figure 3.7.: Structure of GeTe. GeTe crystalizes in a distorted rhombohedral structure (space group R3m). The rhombohedral cell is made visible by the green lines (lattice constant a = 4.291 Å, angle $\alpha = 58.49°$). One sub-lattice is occupied by Ge atoms (blue), while the Te atoms occupy the other sub-lattice. The Ge sub-lattice is shifted half a space diagonal in respect to the Te sub-lattice. GeTe shows a Peierls-like distortion pattern along the [1 1 1] direction (displacement x = 0.529), which leads to a splitting of the bonds into three longer (3.19 Å) and three shorter (2.83 Å) ones (values determined by Neutron Pair Distribution technique see chapter 3.1, fit is shown in figure 3.8). The resemblance of the rhombohedral cell to an NaCl structure is easy to recognize.

Table 3.1.: Fit parameters for a rhombohedral GeTe model. The fit has been performed with different ranges. Listed are the lattice constant a, rhombohedral angle α, displacement parameter ADP, and R_w value of the fit. A variation of the fitting range does not lead to a significant change of the fit parameters. All values confirm the literature data, and thus support the approach to fit the pair-distribution function with a crystalline model.

r-range	2.5 - 20.5 Å	2.5 - 6 Å	6 - 20.5 Å
lattice constant a (Å)	4.291 ± 0.005	4.270 ± 0.032	4.291 ± 0.007
angle α (°)	58.49 ± 0.10	58.88 ± 0.65	58.48 ± 0.01
ADP	0.529 ± 0.001	0.528 ± 0.001	0.531 ± 0.002
R_w	0.2024	0.153	0.215

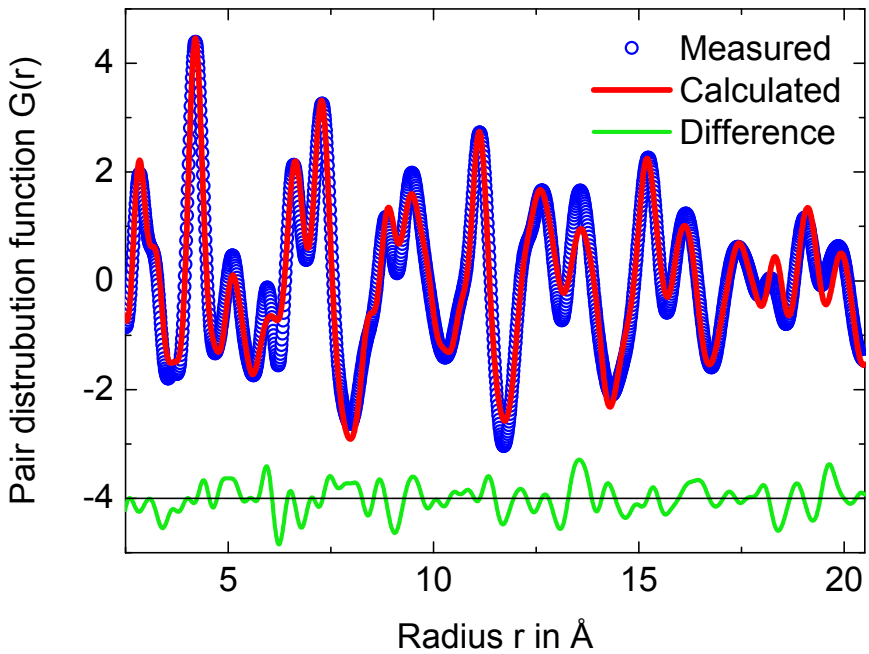

Figure 3.8.: Fit of a rhombohedral model to the total pair-distribution function of GeTe (range 2.5 - 20.5 Å). Space group R3m, Ge occ 0.97 at (0, 0, 0) Te occ 1 at (0.5, 0.5, 0.5), lattice constant 4.291 ± 0.005 Å, rhombohedral angle α = 58.49 ± 0.10°, displacement parameter 0.5293 ± 0.0011

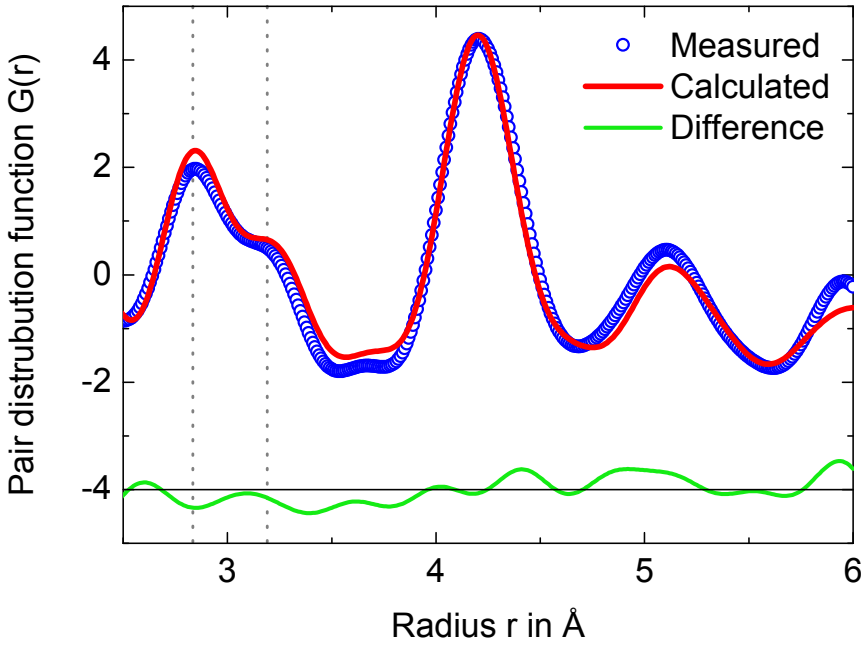

Figure 3.9.: PDF of short to medium range order of GeTe. Peierls-like splitting of the nearest neighbors into 3 shorter (2.83 Å) and three longer (3.19 Å) bonds is indicated by the dotted lines.

3.5. Comparison of the structure of GeTe and $GeSb_2Te_4$

As the pair-distribution technique has shown its capabilities for a well-understood structure such as GeTe, it is time to move to new frontiers and see what can be learned from applying this method to a more complex material such as $GeSb_2Te_4$. The pair-distribution functions of GeTe and $GeSb_2Te_4$ are compared in figures 3.10 and 3.11. They both show a similar pattern of peaks in the G(r) indicating a strong similarity of the structure. Some details, however, do show differences. Especially in figure 3.11, the clear Peierls-like splitting of the first neighbor peak is absent in $GeSb_2Te_4$. However, the peak is broad and therefore represents a range of distances. To deepen the understanding of this behavior, the structure and the static displacement in $GeSb_2Te_4$ will be analyzed in detail in the following section.

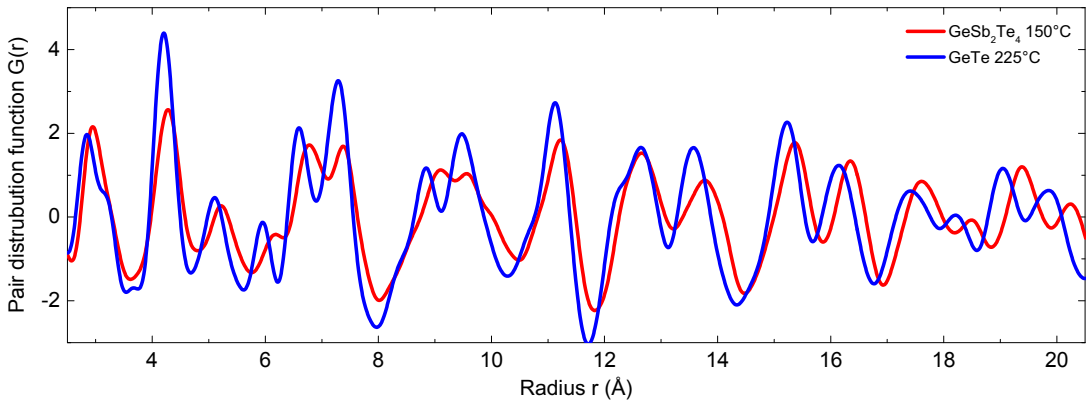

Figure 3.10.: Total pair-distribution function G(r) of GeTe and $GeSb_2Te_4$. In the overview from short to long range order of the total pair-distribution function for GeTe and $GeSb_2Te_4$ the general similarity of the structure of the two materials can be seen. All basic features seen in GeTe can also be found in $GeSb_2Te_4$. This overview already shows a better ordering of GeTe as it has sharper and higher peaks in the PDF. Compare as well with B.2.

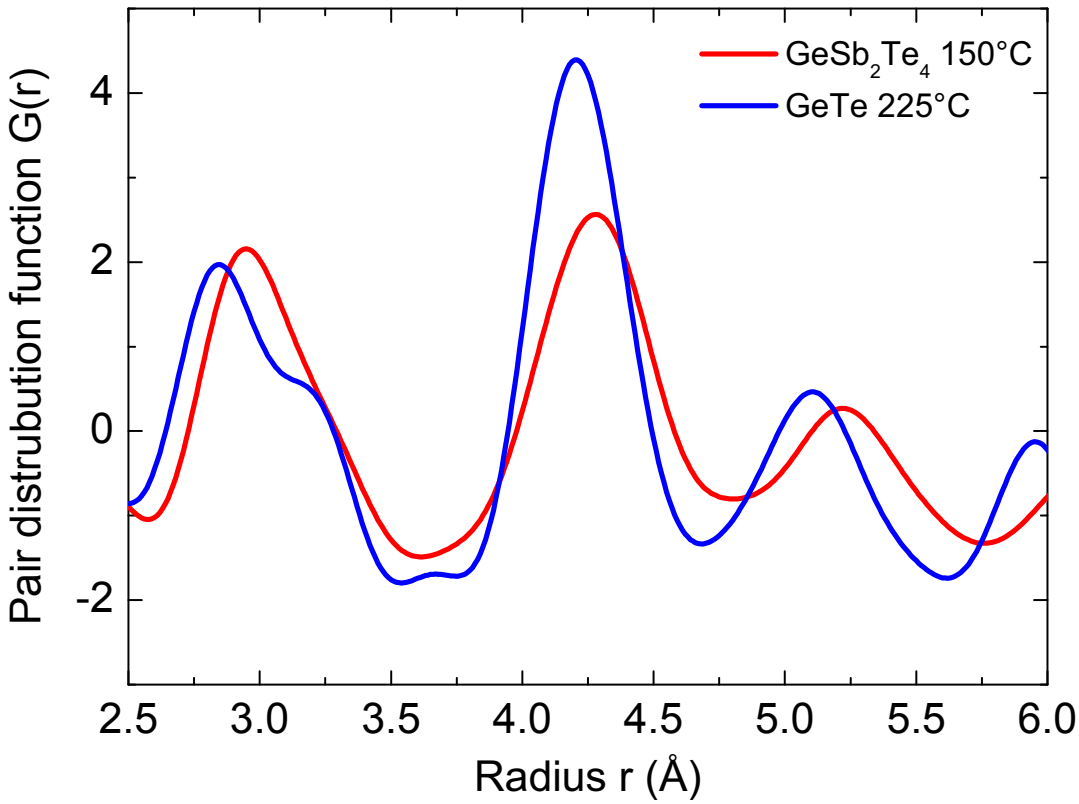

Figure 3.11.: Comparison of the short to medium range order of GeTe and $GeSb_2Te_4$. GeTe and $GeSb_2Te_4$ show similar distances. A clear Peierls-like splitting of the first neighbors can be seen for GeTe. $GeSb_2Te_4$ shows a broadening of the nearest neighbor. It is not evident how many distances are causing this broadening. However, the distribution of the distances is narrow enough to exclude tetrahedral coordinated Ge, with a Ge-Te distance of 2.6 Å, as proposed by Liu *et al.* [84]. For the second nearest neighbor, a sharper peak is observed for GeTe, which indicates a higher degree of order in the crystalline phase. The annealing of $GeSb_2Te_4$ shows only slight changes in the PDF. Compare as well with B.2.

3.6. Structure of $GeSb_2Te_4$

$GeSb_2Te_4$ has been described as an NaCl-like cubic structure [17] with a lattice constant a = 6.043 Å. In the NaCl structure, two fcc sub-lattices are shifted along the [1 1 1] direction by half a space diagonal. One sub-lattice is occupied with Te atoms while the other is randomly occupied with 25% Ge, 50 % Sb, and 25 % vacancies.

3.6.1. Rhombohedral model for $GeSb_2Te_4$

A rhombohedral model can be applied to an NaCl structure, see figure 3.7. This has the advantage of fewer free parameters. Starting from the GeTe model, the Germanium atoms have to be replaced by 25% Germanium, 50 % Antimony, and 25% empty lattice sites. This is done by occupation factors for Ge and Sb of 0.25 and 0.5 respectively. Just as in the model for GeTe, a static displacement of the Ge/Sb atoms along the [1 1 1] direction is introduced (ADP). For a rhombohedral model, the value from Matsunaga & Yamada [17] converts to a = 4.273 Å and α = 60°.

As for GeTe (see chapter 3.4), fits with different r-ranges were performed for $GeSb_2Te_4$. A fit of the whole data range (r = 2.5 - 20.7 Å) is displayed in figure 3.12. The fit shows good agreement with the data, especially in the long range order. With lattice parameters of a= 4.286 ± 0.013 Å and α = 59.67° ± 0.28°, the model also agrees with the literature findings. The Peierls-like displacement has an atomic displacement parameter ADP = 0.52 for all the fitting ranges, that is a bit lower than for GeTe.

Fits of the data for short to medium range order (r = 2.5 - 6 Å) and long range order (r = 6 - 20.7 Å) are displayed in figure 3.13. Both fits show an excellent agreement with the data. However, the values determined for these two regions differ from each other (see table 3.2). Fitting the long range order leads to the same values within the error bar as fitting the whole range. In the short to medium range order both the angle α and the lattice constant a differ significantly from the one determined for the long range order. As the long range order and the whole range order values are similar, the whole range fit is dominated by the long range data. The change of α for the local to medium range indicates a difference in local arrangement compared to the long range data, which is averaged out for the long range order. The deviation of the rhombohedral angle α in the short to medium range order can already be seen in the second peak around 4.2 Å, which is not perfectly fitted (compare fig. 3.12 and 3.6).

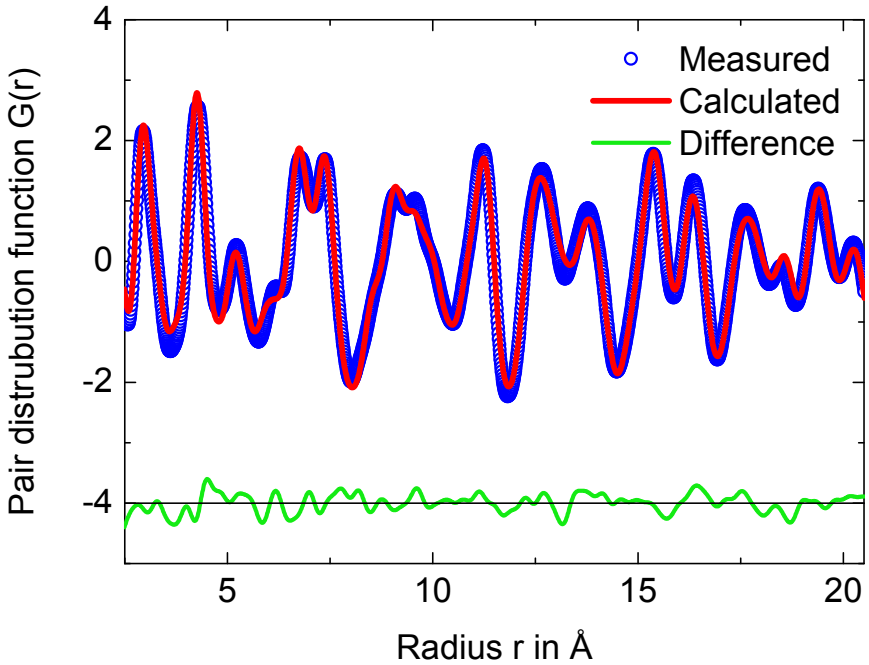

Figure 3.12.: Rhombohedral fit of the pair-distribution function G(r) for r = 2.5 - 20.7 Å for crystalline $GeSb_2Te_4$ annealed at 150 °C. Parameters of the fit are lattice constant a=4.2857 Å, angle $\alpha = 59.67°$ and ADP = 0.5185. Fitting this range leads to a cubic like rhombohedral cell with an angle close to 60°. The atomic displacement parameter (ADP) allows a displacement only along the [1 1 1] direction.

The chosen model of the crystal structure of $GeSb_2Te_4$ only allowed an atomic displacement along [1 1 1] direction, which leads to a splitting of the 6 nearest neighbor bonds into three shorter and three longer ones. This lowers the number of free parameters besides the small box of only two atom sites. This has the disadvantage that more complex atomic displacements can not be represented. However, fitting a larger number of atoms and displacing these atoms freely has not worked out; these fits were not stable and the program normally ended up in the same χ^2 minimum.

3.6.2. Displacement model from DFT calculations

In order to test a more sophisticated structural model, mainly in the short to medium range order, data from density functional theory (DFT) calculations [85] were compared to the data of this study. Lencer [14] calculated the local structure for different non-binary phase-change

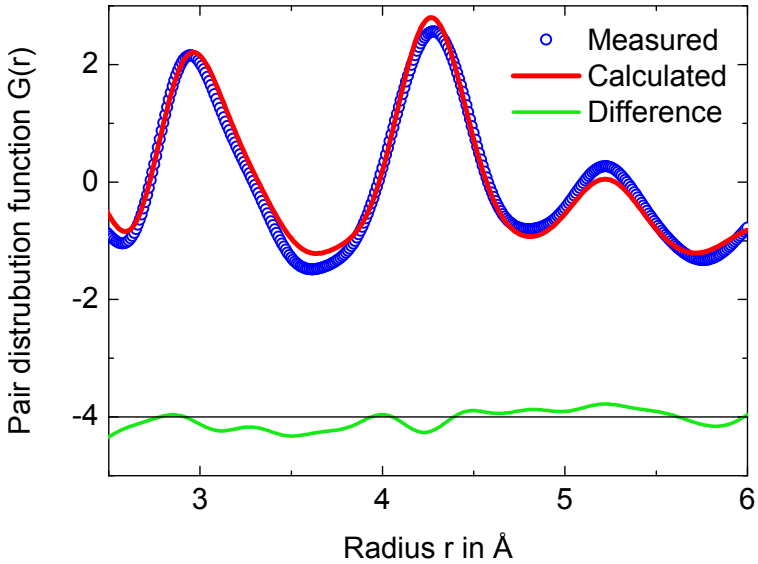

(a)

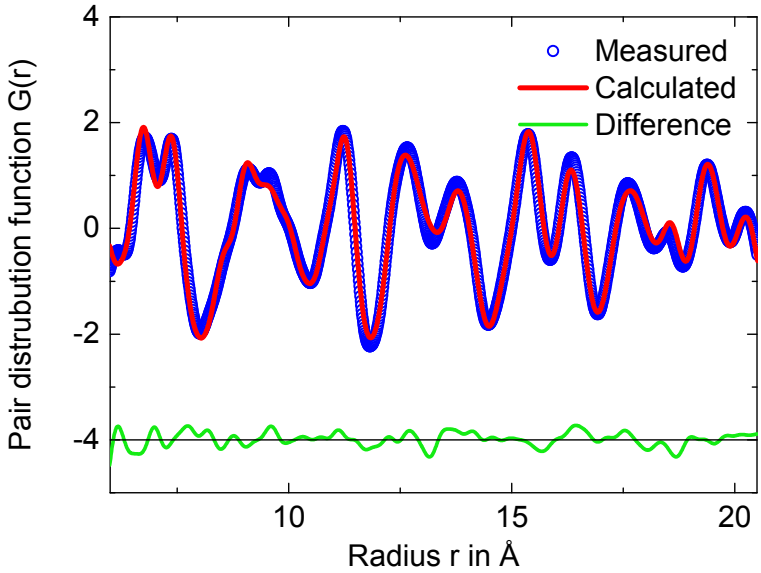

(b)

Figure 3.13.: Comparison between the short to medium range order and the long range order in crystalline $GeSb_2Te_4$ annealed at 150°C. The rhombohedral distortion is much larger in the short to medium range order. The displacement along [1 1 1] is not effected by the change in fitting range within its error margin. **(a)** In the short to medium range order (from 2.5 - 6 Å), the rhombohedral distortion is much clearer as compared to 3.12, as can be seen from the angle α= 58.83° . **(b)** In the long range order r = 6 - 20 Å the rhombohedral distortion is avaraged out, as can be seen from the value α = 59.71°.

Table 3.2.: Fit parameters for rhombohedral $GeSb_2Te_4$ model. The fit has been performed with different ranges. Listed are the lattice constant a, rhombohedral angle α, displacement parameter ADP and R_w value of the fit. Compared to GeTe, the values are more dependent on the fitting range. Even though the errors are larger as well, the differences are significant with respect to the errors. Fitting the long range order leads to values in agreement with literature [17]. The rhombohedral angle of the short to medium range order fit (r = 2.5 - 6 Å) shows a significant deviation from 60°, thus the short to medium range order shows a rhombohedral distortion that averages out in the long range.

r-range	2.5 - 20.7 Å	2.5 - 6 Å	6 - 20.7 Å
lattice constant a (Å)	4.286 ± 0.013	4.360 ± 0.047	4.283 ± 0.014
angle α (°)	59.67 ± 0.28	58.83 ± 0.95	59.71 ± 0.3
ADP	0.519 ± 0.002	0.520 ± 0.002	0.518 ± 0.004
R_w	0.146	0.140	0.135

materials. His attention was primarily focussed on the volume (or pressure) dependence of the structure. By varying the lattice constant of a 56-atom DFT box, he showed that the displacement of the atoms is reduced with smaller lattice constants (equivalent to higher pressure). In addition, a displacement pattern depending on the local environment was identified. A 3+3-type splitting (corresponding to a [1 1 1]-type distortion) was found to be likely if the fourth shell contained no vacancies (see figure 3.15), that is to say if the surrounding is GeTe-like, the displacement pattern is also GeTe-like (along [1 1 1]).

To test the validity of this displacement model, the coordinates of a 56 atom DFT box taken from Lencer [14] were put into the structural model for $GeSb_2Te_4$ in PDFgui. The only parameter fitted was the box dimension, as DFT overestimates bond length when using GGA potentials, see figure 3.14. The agreement of the fit was rather uncorrelated to the fitting range. The R_w values differed only between $R_w = 0.126$ for the short to medium range and $R_w = 0.118$ for the long range order. In figure 3.14, the short range order shows a better agreement to the fit than the rhombohedral model does.

With this model the differences in peak shape for the nearest neighbor in the G(r) between GeTe and $GeSb_2Te_4$ seen in figure 3.11 can be understood. A clear double peak is visible in GeTe, corresponding to the 3+3-type splitting, whereas one broad peak is observed for $GeSb_2Te_4$. The latter consists of both 3+3-type splitting and a further displacement pattern in the vicinity of the vacancies.

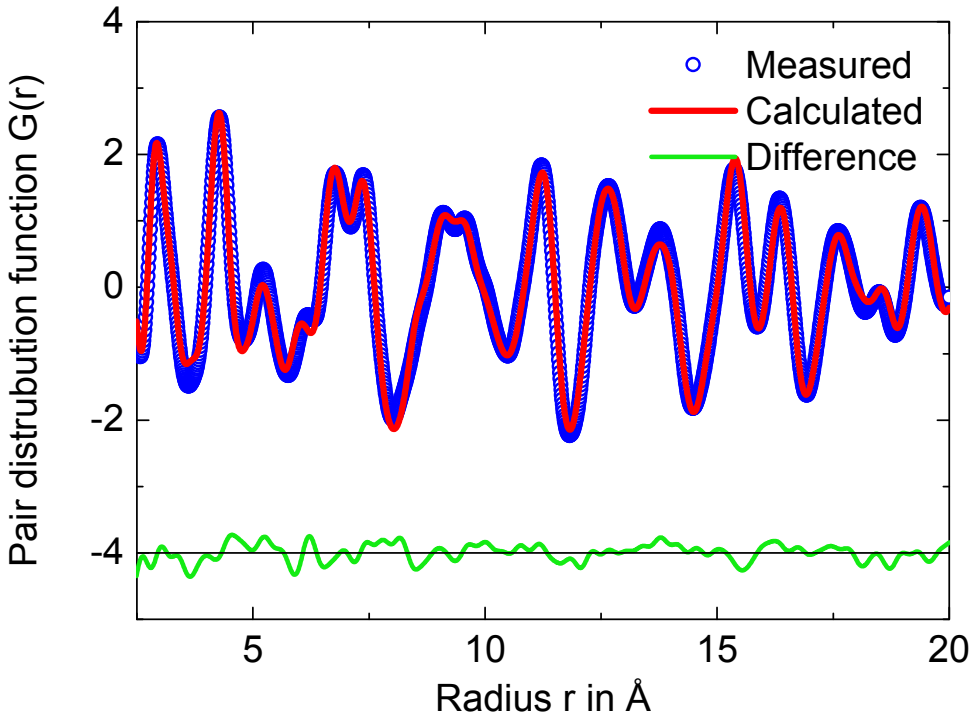

Figure 3.14.: Comparison of DFT data with the experimental data. The relative coordinates of the 56 atom box remained unchanged, only the box size was fitted (DFT calculations from Lencer [14]). With a value $R_w = 0.124$, the agreement between the fit and the data is better than for the simple rhombohedral model. Particularly the model for the short range order appears improved. The displacement pattern of the DFT calculation is displayed in 3.15.

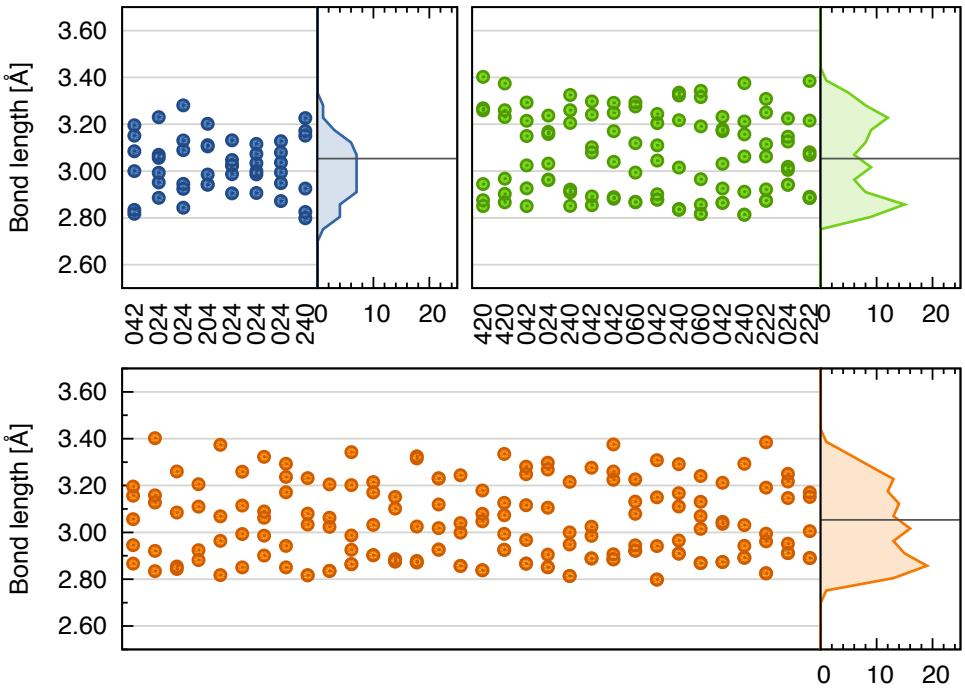

Figure 3.15.: Displacement pattern in $GeSb_2Te_4$ calculated by DFT. Bond length distribution plotted for Ge (blue), Sb (green), and Te (orange) for a 56-cell of $GeSb_2Te_4$. Horizontal lines indicate the respective unique bond lengths expected for undistorted rocksalt structures. The three digit numbers on the x-axis describe the local environment of Ge and Sb. XYZ means there are X Ge-, Y Sb-atoms, and Z vacancies in the fourth shell (atom behind the nearest neighbor). Lencer [14] found the occurrence of a 3+3-type splitting (corresponding to a [1 1 1]-type distortion) to be likely if Z = 0. The calculation was performed with a lattice constant of a = 6.107 Å. [14].

3.7. Annealing effects on structure of $GeSb_2Te_4$

In this section, the annealing-dependent changes in the short-to-medium range order of the rhombohedral model for $GeSb_2Te_4$ will be analyzed. Especially with respect to the disorder-induced localization in chapter 2, it is very interesting to see which changes in bonding might be responsible for the metal-to-insulator transition.

The pair-distribution function G(r) is plotted for the short to medium range order in figure 3.16. The differences between the annealing steps are not easily evaluated as they are so small. One needs to keep in mind that the transition temperature from cubic to hexagonal is at 225 °C. This transition is only visible in the small shoulder at 3.8 Å corresponding to the shortening of the Te-Te distances across the vacancy layers that form in the hexagonal phase. Therefore it can be concluded that the bond lengths do not change significantly on annealing. This is inline with results gained from EXAFS measurements, where only a small increase in bond length is observed [86].

To take a closer look at the differences in the pair-distribution function on annealing, fits with the previously introduced rhombohedral model (see section 3.6.1) were performed starting with the 150 °C annealed sample. In the following annealing stages, refined values of the previous annealing step was sequentially used as input parameters. The refined parameters in these fits were the lattice constant a, the rhombohedral angle α and the atomic displacement parameter ADP along [1 1 1]. The evolution of the parameters and the corresponding errors is shown in figure 3.17.

As expected from the small changes in the G(r) on annealing (Fig. 3.16), the changes of the fit parameters are not significant, particularly if the error bars are taken into account. Both lattice constant a and rhombohedral angle α do not change significantly or even systematically on annealing. The correlation of the parameters for lattice constant a and angle α reduces the significance of the change in these parameters for the 225 °C annealing step. The atomic displacement along [1 1 1], however, is reduced continuously from ADP = 0.520 ± 0.002 to ADP = 0.512 ± 0.004 on annealing to 275°C. DFT calculations of Zhang [87] have shown that a reduction of displacement is energetically favorable.

Further fits were performed in order to test the assumption of the annealing dependent behavior of lattice constant angle and displacement (dashed lines in fig. 3.17). A change on annealing can be excluded for lattice constant a and angle α as the error of the slope for both is negligible compared to the error. The reduction of the displacement, however, has an error

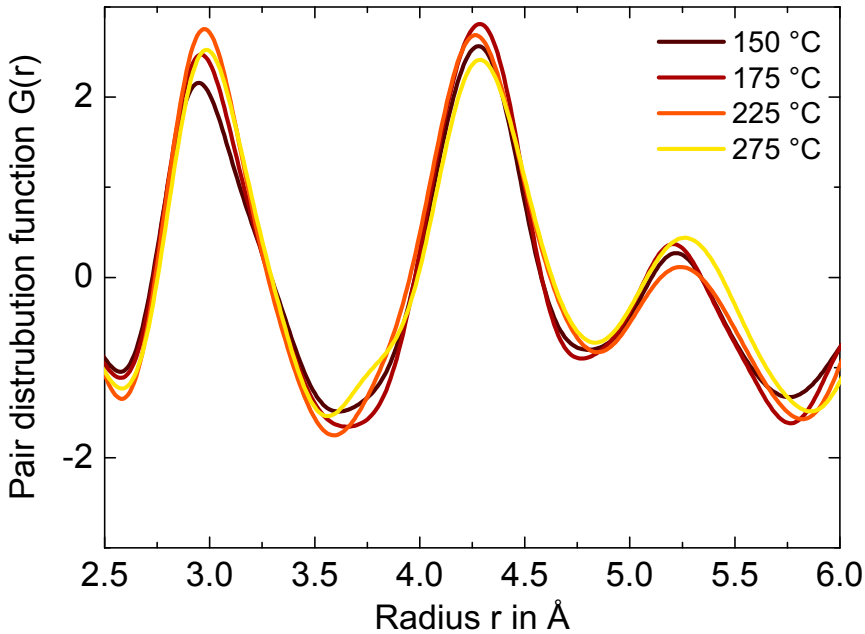

Figure 3.16.: Annealing effect on short to medium range order PDF of $GeSb_2Te_4$. The differences between the annealing temperatures are small, so trends are difficult to foretell. The differences between the annealing temperatures are remarkably small if we consider the temperature of 225 °C at transition from cubic to hexagonal phase. Obviously, the transition does not affect the short to medium range order.

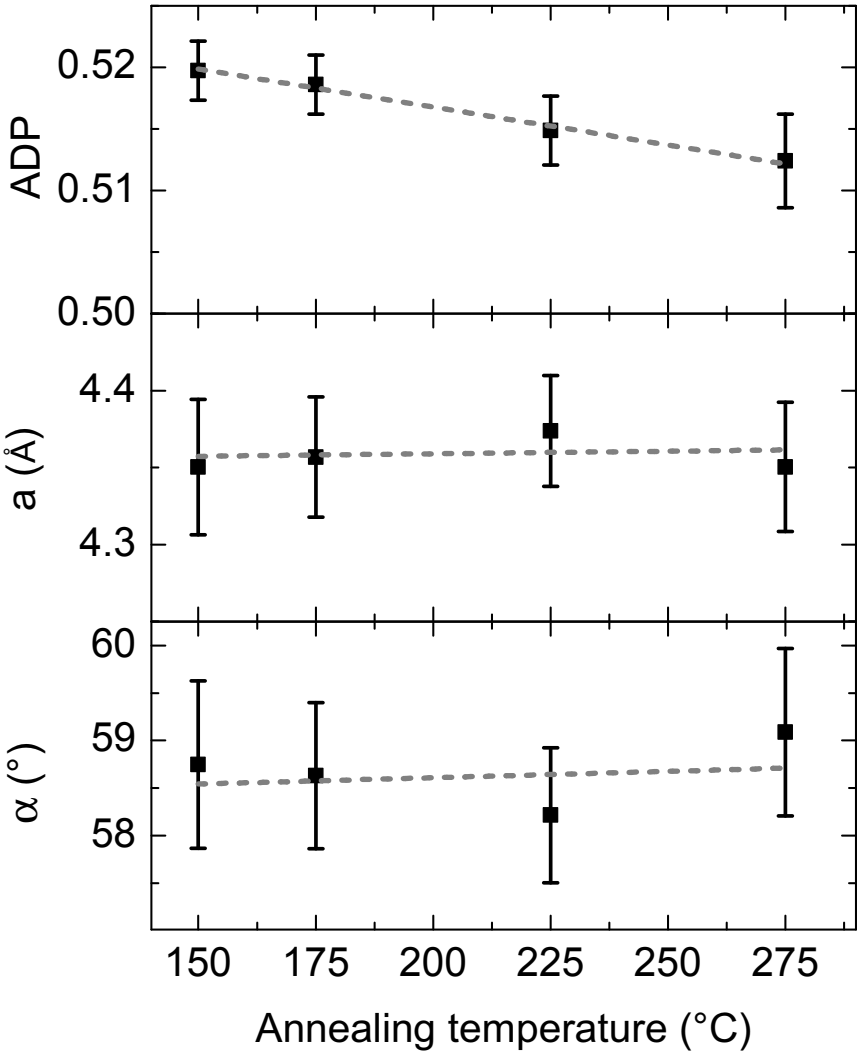

Figure 3.17.: Neutron PDF fit parameters of $GeSb_2Te_4$ on annealing. Changes on annealing shown from top to bottom: atomic displacement along [1 1 1] ADP, lattice constant a, and rhombohedral angle α. Both lattice constant and angle show no trend within the error margin. The atomic displacement is distinctly reduced with increasing annealing temperature. Linear fits to the data were performed (dashed lines) as they serve as indication for the temperature dependance. For both a and α, the error is larger than the slope by more than a factor of three. The slope of the fit for the displacement ADP has an error of about 7%. In a local picture the distortion can be seen as a displacement of the octahedral coordinated Ge/Sb atoms in such a way to form 3 shorter and 3 longer bonds. This is consistent with the reduction of the disorder induced localization described in chapter 2

Table 3.3.: Linear fit parameters for annealing dependence of $GeSb_2Te_4$. Linear fits to the data in figure 3.17 have been performed. The slope for the lattice constant and the angle vanishes with respect to the error and confirms that these values do not change on annealing. Nevertheless the displacement is significantly reduced on annealing: the error on the slope is less than 10 %.

	slope	intercept
ADP	- $(6.169 \pm 0.446) \cdot 10^{-5}$	0.529 ± 0.001
lattice constant a	$(3.3 \pm 15.4) \cdot 10^{-5}$	4.352 ± 0.003
rhombohedral angle α	$(1.3 \pm 4.9) \cdot 10^{-3}$	58.34 ± 1.04

of only about 7%. We may conclude for the rhombohedral model that a reduction of atomic displacement along [1 1 1] dominates the lowering of the disorder induced localization in $GeSb_2Te_4$.

3.8. Summary of Crystallographic Analysis of Disorder

The crystal structure of GeTe and $GeSb_2Te_4$ were analyzed using the neutron pair-distribution method. It is a local probing method and well suited to determine the local structure rather than the average structure determined by normal scattering experiments.

GeTe crystallizes in a rhombohedral structure with a lattice constant a = 4.291 Å, an angle $\alpha = 58.49°$ and an atomic displacement ADP = 0.529. The displacement of Ge along the [1 1 1] direction leads to a 3+3-type splitting. Literature values for GeTe determined by coherent scattering claim the same results. It can therefore be concluded that for GeTe the local and the average structure are the same.

The crystal phase of $GeSb_2Te_4$ is generally assumed to be a distorted NaCl-like phase and can be modeled successfully using a rhombohedral structure. For a rhombohedral angle of $\alpha = 60°$ these two structures are the same. The local and the average structures of $GeSb_2Te_4$ differ, in contrast to GeTe: the rhombohedral distortion is larger for the short to medium range order than for the long range order.

$GeSb_2Te_4$ also shows an atomic displacement away from the symmetry lattice sites. It

can be modeled with a distortion along [1 1 1], but a more complex model based on DFT calculations describes the structure better. In the DFT based model, the distortion pattern depends on the amount of vacancies in the fourth shell around the corresponding atom.

For $Ge_2Sb_2Te_5$, large displacements of Ge have already been shown by Shamoto *et al.* [19] with neutron PDF measurements. These data were analyzed with PDFfit [88], the predecessor program package of PDFfit2.

The annealing dependent changes were analyzed with respect to the disorder induced localization in $GeSb_2Te_4$ discussed in chapter 2. It could be shown that the displacement of Ge/Sb is reduced on annealing, which results in a reduction of disorder. As the MIT observed in $GeSb_2Te_4$ is disorder driven, the reduction of displacement is likely to be a relevant for the observed MIT.

CHAPTER 4

Electrical Switching in Phase-Change Materials

In the previous chapters it has been shown that phase-change materials are an extraordinary material class offering multiple chances to study interesting physical phenomena. In the following chapter, however, the focus will lie more on application of phase-change materials as electronic data storage. Two different aspects of storing information in a phase-change memory cell are addressed. First, after a introduction in the basic principles of a phase-change memory cell, a new approach of storing information with disorder encoded $GeSb_2Te_4$ memory will be presented. Second the limitations of the switching speed in state of the art memory cells will be tested for GeTe.

Data storage is, of course, one of the key features of a personal computer, but the demands on the kind of storage vary for different applications. While long-term data storage is the most important feature for applications like archiving data, for others, speed is the ultimate challenge. For example SRAM close to the processor, speed is most important, but storage times are needed on a µs timescale only. As speed and volatility are the two main competing properties[1] for the design of data storage, different types of storage are nowadays used for personal computers. The aim is to combine advantages and to overcome limitations of the different types. Any new memory class will have to find its own niche within the existing application range. Another approach is to try to replace an existing type with a similar one of higher speed, higher volatility, or reduced production costs.

Phase-change materials could provide [89] data retention of years [90] and speed below 100 ns [91]. They could therefore enter the memory market in between high speed but

[1] Energy consumption may also be important, especially for mobile devices.

volatile DRAM and non-volatile but low speed Flash memory. In order to examine the options, switching speed was tested with state-of-the-art nanometer-scaled phase-change memory devices. In addition, possibilities of new multi-level states were explored, namely storing multiple logical bits in one physical memory cell [92].

4.1. Working principle of phase-change memory

Phase-change memory does not store its data in a charge or magnetic state, but encoded in a structural state. The two states are the amorphous and the crystalline state that differ significantly in resistivity (see figure 2.3). The basic operations of a phase-change random-access memory (PCRAM) are displayed in figure 4.1. The figure shows a two dimensional cut through a phase-change memory cell in a bottom heater geometry [93]. The active phase-change material is sandwiched in between a small bottom electrode and a larger top electrode. The bottom electrode is often referred to as heater, because due to the design of the two electrodes most of the Joule heating is within the bottom electrode and in its vicinity. The two write operations SET/RESET are sketched in figure 4.1, top part. (1) To write an amorphous region (RESET) into the crystalline phase-change material, a high voltage pulse is applied, which results in a partial melting of the material. A subsequent quenching of the molten phase into the amorphous phase leads to the so-called *RESET state*. (2) To recrystallize the amorphous region (SET) and, therefore, to erase the bit, a moderate voltage pulse has to be applied. This causes the phase-change material to heat above the glass transition temperatures, which, in turn, leads to a crystallization of the cell (*Set state*). Both RESET state (3) and SET state (4) can easily be sensed via a low voltage pulse due to their large contrast in resistance.

Erasing the amorphous region in the SET operation is generally accepted to be the time-limiting operation (see [2]). It is a complex step: The amorphous cell has a resistance in the MΩ regime, and a current of a few mA is needed to heat the cell above the glass-transition temperature. So one would expect that a voltage of kV is required to produce the necessary temperature, in accordance with Ohms law. However, the threshold effect in amorphous semiconductors, discovered by Ovshinsky [94] in 1968, is also involved. The threshold effect describes a highly non-linear current-voltage dependence. On applying a voltage to the phase-change memory cell the current rises slowly as expected by Ohms law. After reaching the threshold voltage, the amorphous phase-change material changes from igh resistive *amorphous off-state* to a low resistive *amorphous on-state* and the current rises significantly.

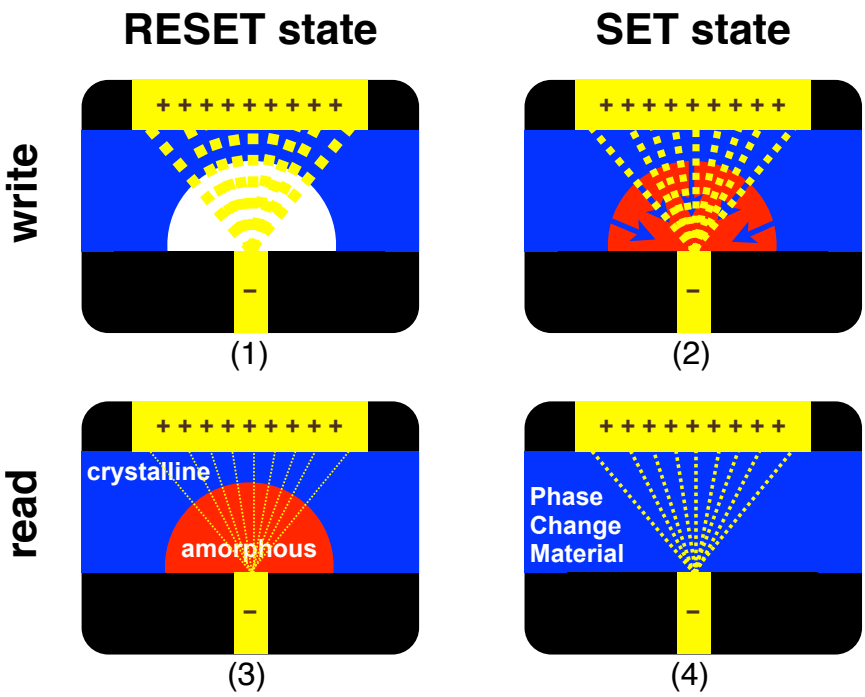

Figure 4.1.: Working principle of a phase-change memory cell shown in a cross section. RESET and SET state are written with a high (1) or a medium voltage pulse (2), respectively. Both can easily be sensed with a low pulse (3) & (4).

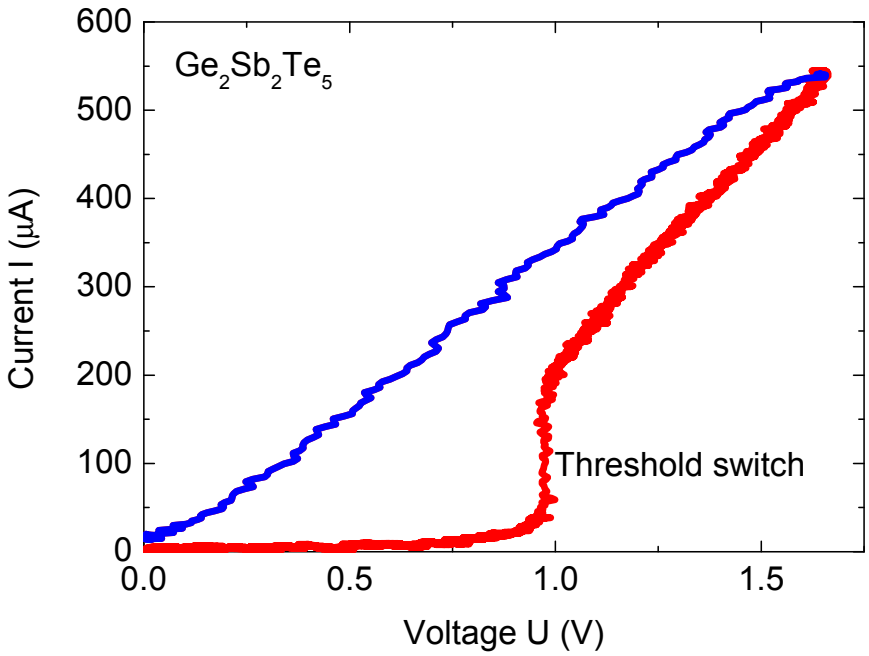

Figure 4.2.: Threshold switch in $Ge_2Sb_2Te_5$. Shown is an I-V curve of an amorphous (RESET) bottom contact cell with $Ge_2Sb_2Te_5$ as active phase-change material. For voltages below the threshold voltage only a neglect able current flows though the cell due to the high resistance of the amorphous off-state. After reaching the threshold voltage, the phase-change material switches to the low resistive amorphous on-state. This can be seen by the sudden increase in current. Due to this increase in current, the temperature of the cell is raised above the crystallization temperature, so the cell is crystallized (memory switch). From [3]

.

Due to this effect, even voltage pulses with a few V can cause currents in the mA regime, which will lead to a crystallization of the cell. The microscopic mechanism of this process is still under scientific discussion [95–98]. A recent study has used a different geometry to show that the threshold switch of phase-change cells is, indeed, a material-intrinsic property that depends on the local electric field [99].

4.2. Disorder encoded multi-level storage in phase-change memory

In multi-level storage, multiple logical bits are stored within one physical memory cell. Two states are normally used to encode the binary information 0 and 1 in one cell. In a multi-level cell, more than two states are used to store information, for example four different cell states to encode the information of two bits (00, 10, 10 and 11). Therefore multi-level storage offers the possibility to increase the storage density by a factor of two, or even more, simply by changing the logic of addressing the cells.

The GeTe phase-change memory cells discussed in the following sections show the possibility of using at least four different states for encoding information. The different states include a fully crystalline cell and three states with different sizes of the amorphous region. Two problems arise from using different amorphous spot sizes, the instability of very small amorphous regions, and the drift of the resistivity within the amorphous phase. The resistivity of the amorphous phase drifts to higher values with increasing duration [100–102]. Therefore, after some time, the resistance of a mid-state will no longer be distinguishable from a high-resistance state. These problems are illustrated for a bridge cell in figure 4.3, upper part.

Figure 4.3, lower part, shows one possible way out of this dilemma. Phase-change materials like $GeSb_2Te_4$ show a wide spread in resistivity within the crystalline phase. This spread depends on the prevalent degree of disorder (chapter 2). The disorder induced localization effect is a generic effect of all GeSbTe samples studied within this work. Therefore a memory cell based on a the degree of disorder, as proposed here, would be very tolerant for variations in stoichiometry. In general the precise control of the stoichiometry is essential in the semiconductor business, as the conductivities strongly depend on the doping level. In phase-change materials in general the properties do not depend on a stoichiometry variation within less than 1 %. This is especially true for materials along the pseudo-binary line between GeTe and $GeSb_2Te_4$.

If disorder in a phase-change memory cell could be controlled by using different SET

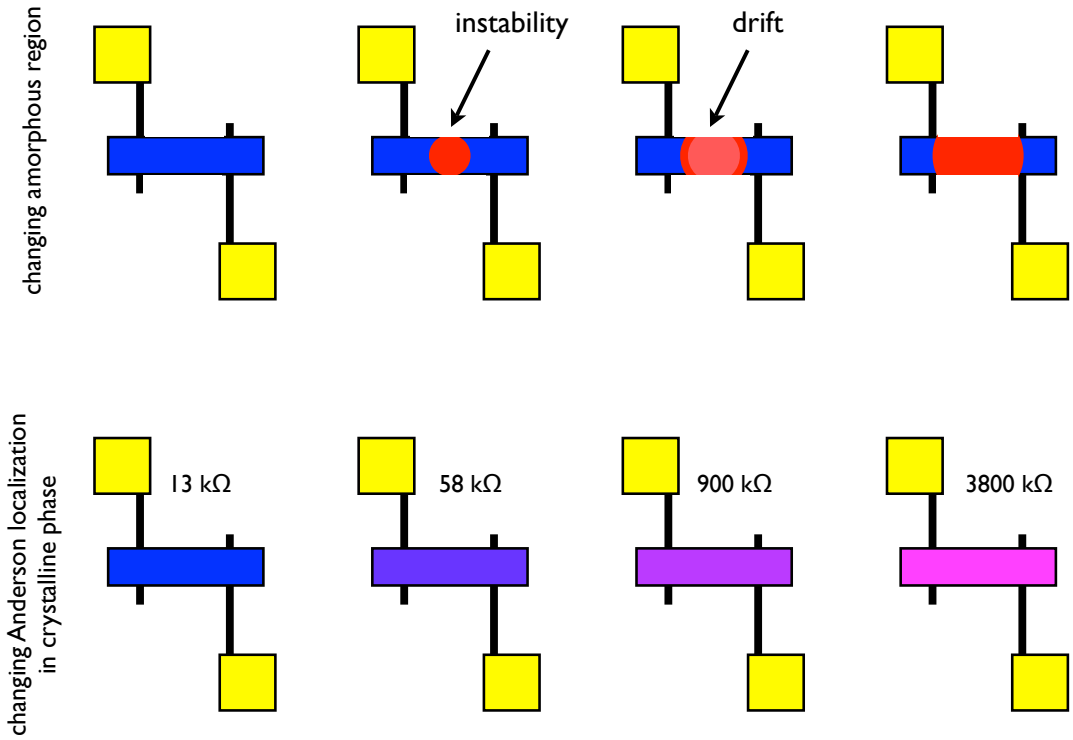

Figure 4.3.: Enabling multi-level PCRAM cells with a new approach. Instead of controlling the size of the amorphous region (instability and drift problems), one can control the resistance of the cell by the degree of disorder-induced localization. With cell dimensions of 135 x 45 x 3 nm, four levels between 13 kΩ and 3.8 MΩ are possible.

temperatures, for example, multi-level phase-change memory cells are conceivable that do not entail problems such as drift or instability.

4.3. Phase-change memory cell preparation

A cooperation with the former Qimonda AG, Dresden, allowed the preparation and study of phase-change memory cells in a bottom heater geometry. The analysis was carried out as a joint project with my colleague Gunnar Bruns [103]. Qimonda provided 300 mm base wafers containing pre-structured cells with contact pad pairs. One of each pair is connected to a TiN heater with a diameter of 60 nm via a buried Tungsten line (see figure 4.4 left). The wafers were shipped to Aachen, where the subsequent preparation steps were performed. The wafer was cleaved into single chips (see figure 4.4 center). The active phase-change

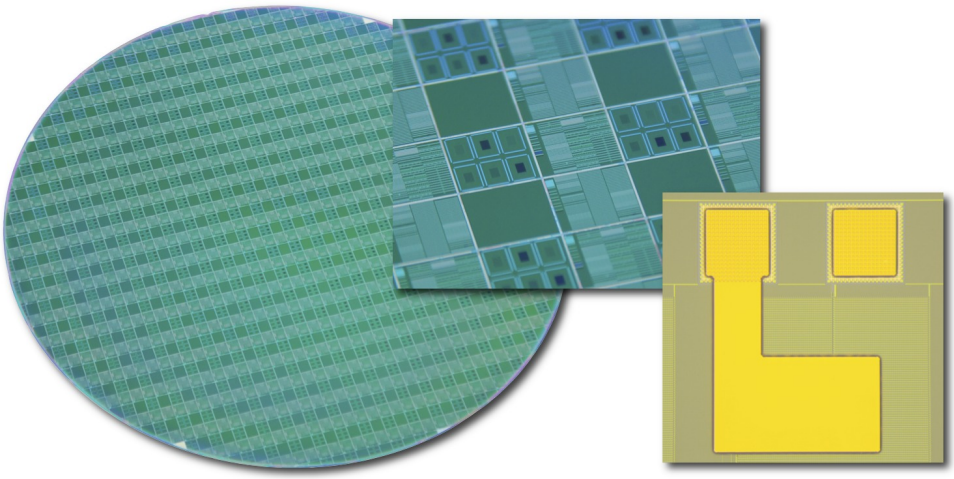

Figure 4.4.: PCRAM base wafer and single cell. In cooperation with Qimonda a 300 mm wafer was prestructured and subsequently shipped to RWTH Aachen, where single chips (center) were cleaved to finalize the PCRAM single bit cells with the active material and the top contact (right).

material and a Ti/TiN[2] top contact were deposited by sputtering. To separate top and bottom electrode contact pads, optical lithography with subsequent lift-off was used. The resulting L-shaped phase-change memory cell can be seen in figure 4.4 right.

After cleaving the 300 mm wafer into single chips, each containing 120 phase-change memory cells, the processing continued in the clean-room of the 2. Institute of Physics, RWTH Aachen. The chips were first cleaned using organic solvents (Acetone and Propanol) in an ultra-sonic bath. Photo resist with a thickness of 1.5 µm was applied with a spin coater. After baking the resist at 90 °C for 5 minutes, a Suss MicroTec mask aligner was used to expose the sample to UV light (Hg discharge lamp) through a patterned lithography mask. The exposed resist was removed in the developer bath. To ensure a good electrical contact between the 60 nm heater bottom contact and the active phase-change material, the heater was cleaned with Hydrofluoric acid (HF-dip). This removes any oxides that may have developed on the TiN and passivates the surface for a short period of time. With a narrow time window (less then 15 min) the sample was transfered into the sputtering tool at the 1. Institute of Physics, RWTH Aachen to deposit the active phase-change material and the Ti/TiN top electrode. The photo resist was removed with Acetone after sputtering,

[2]The Ti acts as an adhesion layer for the TiN.

and the L-shaped parts seen in figure 4.4 were left over. Subsequently, the phase-change memory cells were crystallized in a tube furnace under Argon atmosphere. Phase-change memory cells with GeTe as the active material and with a thickness of 20 nm were processed for this study.

Figure 4.5 shows an atomic force microscope image (AFM) of the bottom electrode heater. A Tungsten line appears at the top, buried under Silicon-nitride and connected to the bottom electrode pad. In the center of the image one can see an elliptical shape, which is a bit higher than the SiN. This is the bottom electrode heater. The other structures in 4.5 result from processing the wafer at Qimonda, Dresden. The HF-dip that was used to clean the TiN heater slightly changed its morphology and its surrounding structures. AFM scans of heater structures before and after the HF-dip revealed that the surrounding SiN was etched a little deeper than the TiN heater was (scans not shown). The heater structure in figure 4.5 gives the impression of a pillar. In fact, the heater resembles a flat hill rather than a pillar, as the x-y scale and z-scale are different.

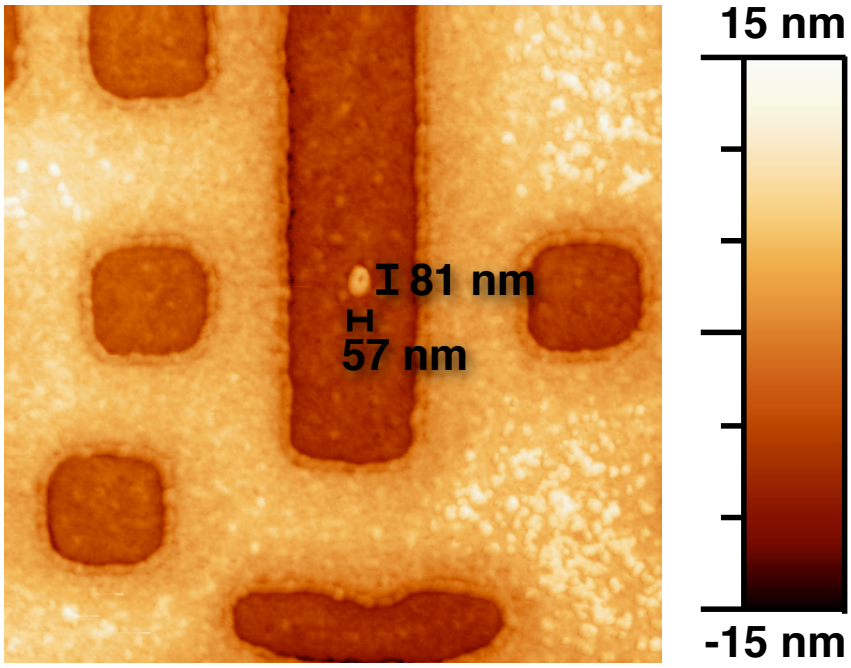

Figure 4.5.: Atomic force microscopy image of a bottom electrode (heater) of a PCRAM cell. The lowest metal line of the wafer (M0) reaches from top to the center. The bottom electrode with a diameter of about 60 nm is visible in the center. The other structures are supporting structures for the polishing process in the production of the heater electrode.

4.4. Pulsed Electrical Tester

The samples were measured with an electrical test setup, called Pulsed Electrical Tester (PET). This setup was designed and built by Schlockermann [104] and Bruns [103] within the framework of their PhD theses. The heart of the setup is a custom-designed printed circuit board with probing needles to contact a single phase-change memory cell. It is designed both to match the impedance of the memory cell, the oscilloscope, and the pulse generator. The printed circuit board also amplifies the signal with a low-noise amplifier in close proximity to the wafer. The printed circuit board was applied in combination with a 500 MHz oscilloscope and an electrical pulse generator, with shortest pulses of 1 ns plateau and 2 ns rise and fall times. In this setup, the PET allows highly accurate measurements of electrical cells. In addition, the setup can measure both the current through the cell and the voltage discharged by the pulse generator.

4.5. Electrical switching in GeTe

Phase-change memory cells with GeTe as an active material were used to test the switching speed of this material. As the SET (crystallization) process is the time-limiting process, this was analyzed in detail. For this purpose, test pulses with different pulse lengths were applied to a GeTe memory cell. The leading and trailing edges were kept constant at 2 ns each. As a starting point, the GeTe phase-change memory cell was re-initialized before each test pulse into a well-defined (high resistive) RESET state. The resistance was chosen so as to secure equal starting conditions for every test pulse. Figure 4.6 shows the results of these measurements. For all pulse lengths, a SET operation to cell resistances < 15 kΩ was successful for currents between 400 µA and 1.1 mA. Only long pulses (16 ns) were able to reach the lowest cell resistances of 3 kΩ. With currents exceeding 1.2 mA, the resistance was again in the MΩ range due to a re-amorphization of the cell. Long pulses heated the sample above the melting temperature and the short trailing edge resulted in a quenching of the sample to the amorphous state.

An observation not depicted in fig. 4.6 is that the pulse current does not only depend on the pulse voltage but also on the pulse length. Higher voltages were needed for shorter pulses to reach the SET current for crystallizing the cell. It would not have been possible to make the plot in figure 4.6 without the custom-made setup that allowed to measure the current during the pulse. This plot highlights the importance of the current. Furthermore,

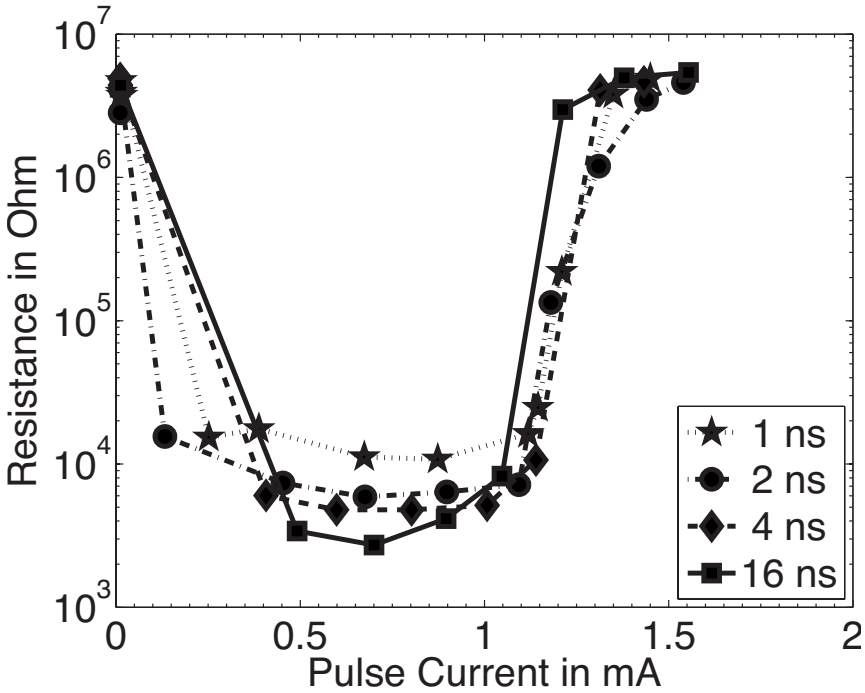

Figure 4.6.: SET window for switching GeTe. Cell resistance vs. pulse current for test pulses applied between 1 and 16 ns. All pulse lengths successfully SET and RESET the cell, while the minimum resistance was only reached for longer pulses [105].

figure 4.6 allows to derive a dependence of the RESET resistance on the pulse current for the 16 ns pulse. RESET resistances between 2 and 7 MΩ are possible with currents between 1.2 mA and 1.5 mA. Therefore multi-level storages with at least four memory states (2 bit) within one cell are conceivable.

A two-dimensional scan of pulse height (voltage) and pulse length was performed in order to investigate the parameters for a successful SET operation of GeTe in detail. Figure 4.7 shows the outcome of this test. Plotted is the plateau height (voltage) vs. the pulse length and in color code the resistance after the pulse. The initial high resistance in the MΩ range is not changed for low pulse heights or very short pulses. Pulses below a voltage of about 1 V do not change the cell state, because such pulses do not exceed the threshold voltage, and current flows are negligible. Pulses with voltages higher than 1 V and longer than 8 ns lead to a crystallization (SET) of the cell. This becomes visible if the resistance drops down to the kΩ range. Pulses of 1.6 V and above re-amorphized the cell thus leading to resistances in

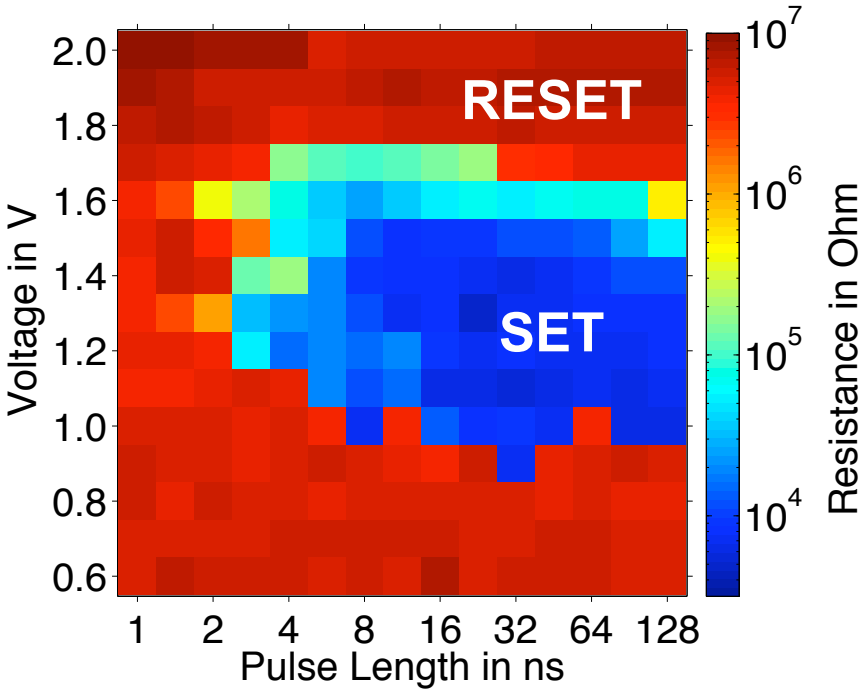

Figure 4.7.: Cell resistance after application of SET pulses with different amplitude and length. Before each pulse, the cell was re-initialized into a well-defined amorphous RESET state of 6 MΩ. Afterwards, the test pulse was applied as indicated by voltage and length. The color of each data point represents the cell resistance after the test pulse [105].

the MΩ range. In order to ensure a uniform and reproducible initial state before each test pulse, the cell was fully SET (3 kΩ) and subsequently RESET to the amorphous state with a resistance of 6 MΩ.

These extremely high switching speeds of 1-5 ns are especially remarkable within the context of earlier laser-induced switching experiments. Recrystallization speeds for GeTe were reported around 30 ns [106, 107]. To set these different results into the right perspective, a closer look at the crystallization mechanism is needed. In general, the recrystallization process is considered as a thermal process proceeding once a material is heated sufficiently long to elevated temperatures. Hence, nucleation and growth rates should be similar both for laser and current induced experiments. The observed difference in the experiments could therefore have its origin in a size effect. For laser experiments, the amorphous spots are typically around 1 µm in size. Here the amorphous region is dominated by the heater size, thus

20-60 nm. Phase-change materials are generally divided into different classes depending on their recrystallization mechanism [107], either growth-dominated or nucleation-dominated. In growth-dominated materials, the crystalline phase develops from the crystalline interface around the amorphous spot in the crystalline surrounding (mark). Recrystallization is governed by the growth of the crystalline phase. In contrast, nucleation-dominated materials form many different crystalline nuclei within the amorphous region. Laser experiments have looked for a dependency between the mark size of the amorphous region and the recrystallization speed in order to distinguish the two classes. Indeed, growth-dominated materials show a dependency, whereas nucleation-dominated materials show an independent recrystallization speed. It is possible that the domination of crystal growth from the crystalline rim causes the high crystallization speeds observed in the electrical cells[3]. If the switching time is dominated by the growth from the crystalline rim, this would lead to a inverse proportionality of the switching time and the diameter of the amorphous region. A larger amorphous diameter of the switchable volume will lead to an increase of the RESET resistance. To validate this hypothesis the SET speed was studied in dependence of the initial amorphous RESET state. The different levels of the RESET state are attributed to different sizes of the amorphous volume within the cell.

Figure 4.8 shows a systematic analysis of the parameters for the SET operation for different initial resistances. The bottom row shows the cell resistance after a test pulse as a function of the applied voltage, the middle row shows the same data as a function of the pulse current, whereas the top row indicates the initial resistance before each test pulse. A sketch of a two dimensional cut through the cell (top of figure 4.8) also indicates the assumed initial state of the cell. For this sketch, it was assumed that the initial states with lower resistance are caused by a smaller amorphous region. Figure 4.8 depicts a dependency of the SET speed on the initial resistance, as the initial state of 2 MΩ can be recrystallized with pulses as low as 1 ns. For the initial state of 6 MΩ the minimum pulse length for a SET operation increases to 16 ns. This supports the hypothesis of a growth-dominated recrystallization mechanism. Moreover, a clear trend of the threshold voltage becomes apparent. This trend can be seen in the pulse current plot of figure 4.8 in the increasing region that is not accessible at low current values with an increasing initial resistance. In the voltage plots of figure 4.8 the trend is visible in the increasing voltage that is needed to crystallize the increasing initial resistance. This supports the assumption of an increase of the amorphous volume for

[3]The TiN heater is an second interface to the amorphous region, which could facilitate crystallization

higher initial RESET states, as the threshold voltage is assumed to be a field effect [99]. An almost constant melting current of about 1.2 mA arises from the current plot and leads to re-amorphization. The voltage plot for short pulse lengths shows that higher voltages are needed to generate these currents. This dependence of the pulse current for short pulses has already been discussed for figure 4.6 and is confirmed here.

Growth-dominated materials in phase-change electrical cells lead to an increase of SET speed. This has been reported previously for $Ge_2Sb_2Te_5$ [108]. For GeTe, however, studies of laser-recrystallization of marks with µm sizes have observed a nucleation-dominated behavior [109]. This implies that the recrystallization mechanism can change with the size of the amorphous spot. This is plausible for 2 reasons. Firstly, with decreasing volume the number of nuclei needed to form within the amorphous region in order to crystallize it decreases and secondly, the interface-to-volume ratio increases.

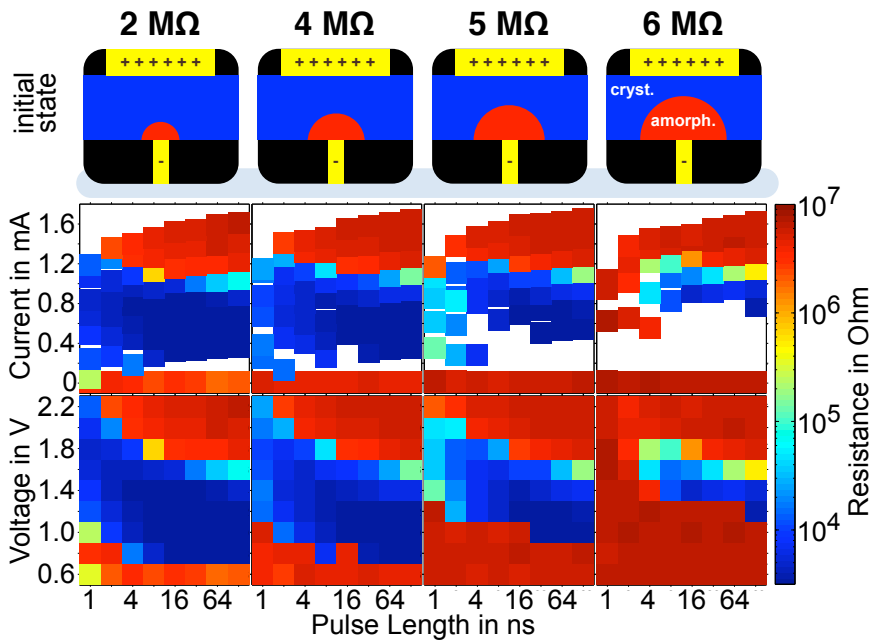

Figure 4.8.: Change of SET speed with initial RESET resistance. The crystallization behavior of GeTe was tested for four different RESET states. In the top part schematic cross sections of the initial state of the cell are displayed. The initial RESET states vary from 2 to 6 MΩ, which is attributed to different sizes of the amorphous region within the cell. The middle and the bottom part of the figure show the resistance after the test pulse for different pulse lengths. In the middle part these values are plotted for the current during the pulse, while for the bottom part the applied voltage is used. The pulse length needed to SET the memory cell is at 1 ns for the cell with a low initial RESET state, but increases with increasing initial resistances to values of 16 ns for the intial state of 6 mΩ. (Color code as in Fig. 4.7) [105].

4.6. Summary of electrical switching in phase-change materials

State-of-the-art phase-change memory cells with GeTe as an active material were produced in cooperation with Qimonda. With these 60 nm cells, we were able to demonstrate for the first time that switching speeds of 1-5 ns are possible with phase-change memory [105]. The study of cells with different initial RESET resistances showed an increase of switching speed for lower RESET state resistances. The threshold voltage showed lower values for the decreased RESET resistance. This allows the assumption that the variation in RESET resistance results from different sizes of the amorphous region. Therefore GeTe, assumed as a nucleation dominated material in laser experiments, shows signatures of a growth dominated material in our study. It was observed that the crystallization mechanism of GeTe changes on decreasing the switchable volume.

With respect to multi-level storage a new approach is proposed: It is based only on the crystalline phase and its resistivity change due to disorder induced localization. This tackles the problem of the non-stable resistivity of the amorphous phase over time.

We may conclude that phase-change materials show a path towards a non-volatile memory with dynamic random-access (DRAM) switching speeds.

CHAPTER 5

Summary and Outlook

In this study phase-change materials have been analyzed with respect to the resistance of the crystalline phase, the crystallographic origin of the resistance and their suitability as a universal memory.

In chapter 2, phase-change materials on the pseudo binary line such as $GeSb_2Te_4$ were shown to have a strong annealing dependence of the resistivity in the crystalline phase. This leads to a reduction of the resistivity of more than 3 orders of magnitude with increasing annealing temperature. Accompanied by this change, the electrical transport mechanism changes from non-metallic to metallic behavior. Low temperature as well as high temperature measurements reveal that this metal-to-insulator transition (MIT) is preserved in a range from 5 K to 600 K. Metal-to-insulator transitions are often caused by an increase in carrier concentration, which leads to an electron correlation based change in the conduction mechanism. The concept of the Mott transition has high predictive power for a variety of materials in all conductivity ranges. However, for the phase-change materials studied here the prediction of the critical carrier concentration by the Mott criterion fails. Hall measurements have revealed that the carrier concentration varies only little on annealing, while the carrier mobility increases drastically at the same time. Phase-change materials on the other hand show a high degree of disorder in the crystalline phase. Crystallization in a distorted NaCl-like phase with Te on one sublattice and Ge, Sb, and empty lattice sites on the other sublattice opens up multiple channels for disorder. The MIT observed in GeSbTe pseudo binary materials is characterized by a disorder induced localization of the charge carriers. This finding of a disorder induced MIT opens up new possibilities to study disordered systems both experimentally and theoretically. One could try to enhance the

disorder within a metallic phase-change material like GeTe or metallic $GeSb_2Te_4$ via ion bombardment to turn it into an insulator.

In chapter 3, the structural origin of the metal-to-insulator transition was analyzed. The origin was not found in a change of the long range order, as in materials like VO_2 [41]. Therefore the analysis focused on changes in the short to medium range order. To do so, neutron pair distribution technique (PDF) was chosen. Two materials were characterized: GeTe and $GeSb_2Te_4$. GeTe shows no strong annealing dependence of the resistivity and has metallic properties for all annealing temperatures. It crystallizes in a rhombohedral structure with a static displacement of Ge along the [1 1 1] direction. This structure is confirmed by the neutron PDF measurements. The rhombohedral model holds both qualitatively and quantitatively for fitting ranges in the short, medium, and long range order. A 3+3-type splitting of the nearest neighbor can be seen from the data, as expected for the displacement along the [1 1 1] direction.

For $GeSb_2Te_4$, two different aspects were analyzed in detail. The structure of $GeSb_2Te_4$ annealed just above the crystallization temperature was investigated first. For these annealing temperatures $GeSb_2Te_4$ is non-metallic. Long range order studies have proposed an NaCl-like cubic structure for this phase. The neutron PDF data evaluation, however, draws a different picture. For the long range data, the literature values were reproduced, but the short to medium range data differ. Especially a rhombohedral distortion was found for fitting distances below 6 Å. This distortion averages out in the long range.

$GeSb_2Te_4$ also shows a displacement pattern along the [1 1 1] direction, but it is not as clear as for GeTe. DFT studies have found a correlation between the local atomic arrangement and the local displacement pattern. It was found that a 3+3-type splitting of Ge or Sb is likely if there are no vacancies in the fourth shell around it. From the coordinates of this DFT calculation the corresponding PDF was calculated. The data match the calculations very good, indicating that such a displacement pattern is a good approximation. For $GeSb_2Te_4$, the annealing dependencies of the structural parameters lattice constant, rhombohedral angle α, and atomic displacement parameter ADP were investigated for the short to medium range order for samples annealed between 150 °C and 275 °C. On annealing, only the static displacement along [1 1 1] drops significantly, whereas the lattice constant and the rhombohedral angle remain constant. The reduced displacement leads to a better formation of resonant bonding and enhances the mobility of the charge carriers. This reduction in displacement is considered one key element responsible for the MIT observed in $GeSb_2Te_4$.

DFT calculations have shown that the distortion decreases under pressure [14]. It should therefore be possible to have a low-annealed (insulating) $GeSb_2Te_4$ sample switch between insulating and metallic state under the influence of moderate pressure. This switching should even be reversible.

The disorder-induced MIT inaugurates a new concept to store data within a phase-change memory cell. It offers a solution to the problem of a resistivity of the amorphous phase which is not stable over time. Using different degrees of disorder within the crystalline phase is a promising mechanism. The launching of PCRAM is delayed mainly due to the unsolved drift in the amorphous phase. This solution, using only crystalline phases, would accelerate the development of new mobile devices with superior speed and improved battery lifetime.

In chapter 4, the possibilities to use phase-change materials as non-volatile memories were evaluated with respect to the switching time. To this end, phase-change memory cells with GeTe as an active material were prepared in cooperation with Qimonda. With dimensions of 20 x 60 nm of the active material state of the art memory cells were available. The switching time for the SET state was analyzed in detail, as it is the time limiting operation of a PC-RAM cell. Switching times below 4 ns were found to be sufficient to operate the cells. Further analysis of the dependency of the switching speed on the initial RESET state shows an increase of switching speed down to 1 ns for decreasing RESET resistances. The change in the RESET resistance is attributed to a change of the amorphous volume in the cell. Therefore, the increasing switching speed is a sign for a growth dominated crystallization of GeTe from the crystalline surrounding. This is an interesting result, as GeTe is categorized as nucleation dominated from laser experiments. The analysis has shown that crystallization kinetics can change if the relevant size of the active material changes. The switching speeds found in GeTe are sufficiently high to be used as phase-change based memory devices. GeTe are therefore high potential contenders for the replacement of FLASH memory and especially of DRAM in mobile applications.

APPENDIX A

New stoichiometric frontiers

In order to apply the existing sputter tool to a wider range of stoichiometries, co-sputtering from two different compound targets was tested in this thesis. As a proof of principle GeTe and Sb_2Te_3 were co-sputtered to see if the deposited films resemble the material properties of a GeSbTe alloy. Therefore the existing sputtering tool was used with standard dynamic sputtering, that means multiple substrates rotate over the plasma of the target, leading to a coating layer by layer. In the co-sputtering geometry chosen in this work instead of from one target, from two targets with different stoichiometries was sputtered at the same time. This leeds to a sample with alternating layers of the compositions of the two targets. We did not simply aim at a multi-layer of GeTe and Sb_2Te_3. Instead, we wished to produce an isotropic film with both stoichiometries, intermixed as well as possible. To this end, the deposition rates of each target were lowered by lowering the sputtering power to 10 W. This lead to sputtering rates of 0.0497 nm/s for both materials (GeTe on Magnetron 3 and Sb_2Te_3 on Magnetron 2). The sample holder does 30 revolutions per minute, therefore the single layer of the multi-layer film will be in the order of 1 Å. With interatomic distances of about 3 Å the 'multi-layer' can be assumed as a well intermixed film. To calculate a ratio of the atomic rates deposited from each target, both the mass density and the average atomic weight had to be taken into account. The densities were determined by XRR to be 5.76 g/cm^3 for GeTe and 6.51 g/cm^3 for Sb_2Te_3. With the average atomic weight numbers the calculated stoichiometry is $Ge_{2.6}Sb_2Te_{5.6}$. With this method samples for van der Pauw resistivity, x-ray diffraction, x-ray reflectivity and FTIR measurements were prepared.

Figure A.1 shows the van der Pauw measurement of a 100 nm thick sample. The as deposited amorphous sample shows a resistivity of 820 Ωcm. This value lies in between

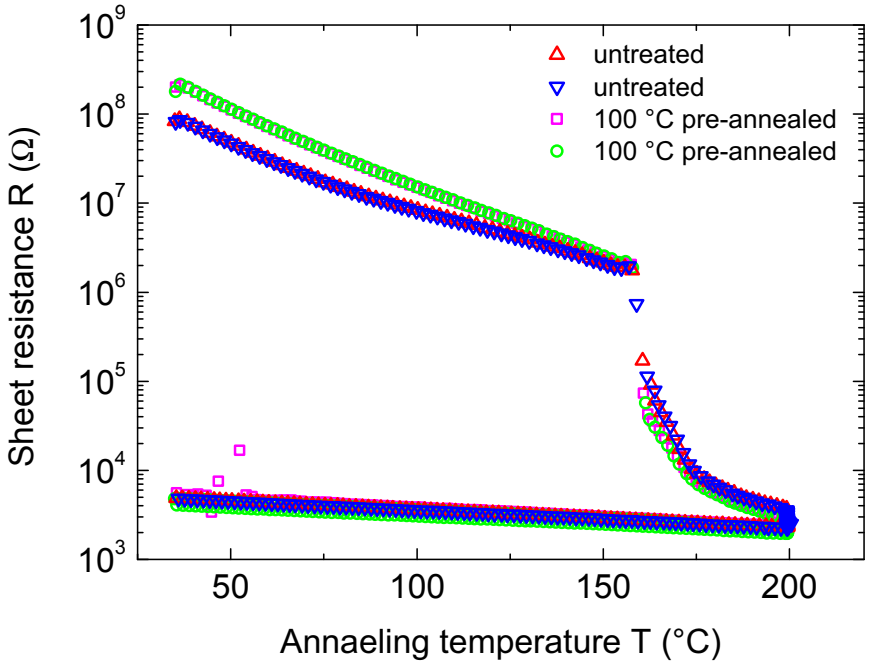

Figure A.1.: Temperature dependent sheet resistance of different co-sputtered GeTe-Sb_2Te_3 samples. Samples prepared with GeTe-Sb_2Te_3 co-sputtering with 10 W power for each target with a thickness of 100 nm. The calculated stoichiometry is $Ge_{2.6}Sb_2Te_{5.6}$, based on the single deposition rates of GeTe and Sb_2Te_3. The onset of the crystallization of 158 °C is a bit higher compared to $GeSb_2Te_4$ (143 °C) or $Ge_2Sb_2Te_5$ (147 °C) [53], as expected for a material closer to GeTe. Pre-annealing at 100 °C for 12 h showed an increase of the amorphous sheet resistance, as expected. The crystallization behavior, however, did not change.

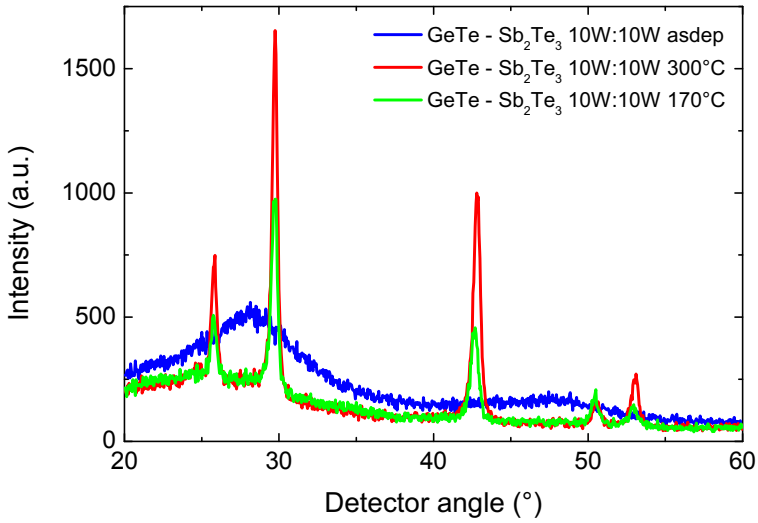

Figure A.2.: X-ray diffractogramm of a co-sputterd GeTe-Sb_2Te_3 sample. The as deposited sample shows no sharp peaks in the diffractogram, as was to be expected for an amorphous sample. Annealing to 170 °C and 300 °C leads to crystallization in a cubic phase with a lattice constant of a = 6.01 Å.

the values of amorphous $Ge_2Sb_2Te_5$ and GeTe with values of 170 Ωcm and 2400 Ωcm, respectively. Heating leads to a continuous decrease of the sheet resistance, as expected for a thermally activated semiconductor. At 158 °C the resistivity shows a steep drop due to the onsetting crystallization. Heating to 200 °C lowers the resistivity further. The negative slope of the resistivity (TCR) on cooling reveals non-metallic behavior. The room-temperature value of the resistivity of ρ = 0.048 Ωcm (conductivity σ = 20.8 S/cm) is in between the values for $GeSb_2Te_4$ annealed at 200 °C and 225 °C (see table 2.1). Pre-annealing for 12 h at 100 °C was tested for a better intermixture of the multi-layer film. It resulted in an increase of the amorphous resistivity to 2000 Ωcm, which can be attributed to the known effect of resistance drift in the amorphous phase (see i.e. [110]). Other than that, the pre-annealed samples show the same behavior as the as deposited.

X-ray diffraction was performed for as deposited samples as well as samples annealed to 170 °C and 300 °C for 30 minutes. The measurements were performed in gracing incidence geometry with an incident angle of ω = 1° and Cu K_α radiation. The results are shown in figure A.2. The as deposited samples shows no sharp diffraction peaks, thus the sample is amorphous. For both the 170 °C and the 300 °C annealed sample diffraction peaks of cubic phase with an lattice constant of a = 6.01 Å are visible. Interestingly for the co-sputtered

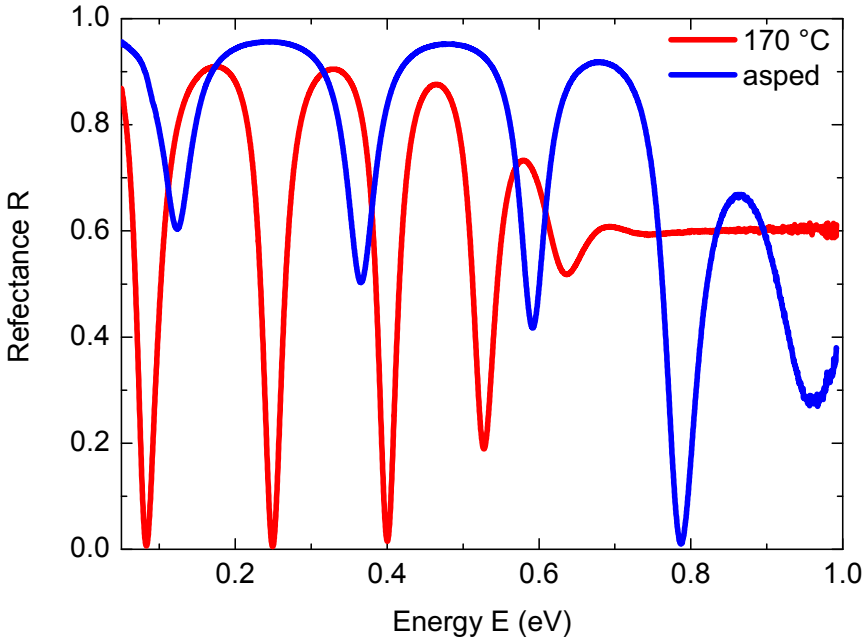

Figure A.3.: FTIR spectra of a co-sputterd GeTe-Sb_2Te_3 sample The FTIR spectra show the same features expected for a sample with a stoichiometry close to $Ge_1Sb_2Te_4$. The bandgap is lowered on crystallization, as can be seen by the dying-out of the oscillations at lower energies due to absorption. The shortening of the oscillation periods indicates a change in ϵ_{inf} which leads to a change of refractive index n. Measurement performed by Jost [111], compare [8]

film with stoichiometry $Ge_{2.6}Sb_2Te_{5.6}$ no cubic to hexagonal transition like in $GeSb_2Te_4$ or $Ge_2Sb_2Te_5$ is observed.

As a final proof FTIR measurements of the co-sputtered films with a thickness of 550 nm were performed. The results for the as deposited amorphous and an oven crystallized sample are shown in figure A.3. From the raw data two striking differences are visible; the interference fringes have a smaller spacing in the crystalline phase and damping of the oszillations at lower energies. The change in spacing of the interference fringes is caused by a change in refractive index, whereas a lowering of the band gap on crystallization leads to the earlier die out. Evaluation of the data with respect to the value of the optical dielectric constant ϵ_∞ leads to values of 19 and 39 for the amorphous and the crystalline, respectively. These values are a little bit higher than the values for $Ge_2Sb_2Te_5$ (compare [67]). The deviation might have its origin in the not exactly characterized film thickness of the

FTIR samples. Therefore we can conclude that the method of co-sputtering was successfully employed to the existing phase-change sputtering tool available at the institute. This new preparation technique was successfully employed by König [112] to preparing $GeTe_{1-x}Sb_x$ samples for her Diploma thesis.

APPENDIX B

Additional Plots

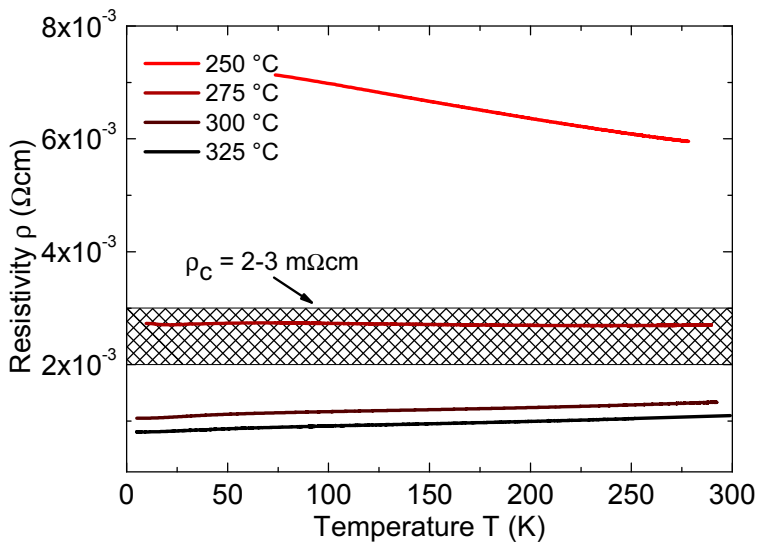

Figure B.1.: Resistivity at low temperatures of $GeSb_2Te_4$ samples annealed around the MIT. Samples annealed in the range from 250 °C to 325 °C are displayed. For an annealing temperature of 250 °C non-metallic, i.e. a negative TCR is observed. The resistivity of the samples annealed to high temperatures (300 °C and 325 °C) remains metallic in the whole range. The critical boundary resistivity between metallic and insulating behavior is valid in the whole temperature range. With no clear slope the sample annealed to 275 °C falls right into this transition regime. (Data taken by Volker [55].)

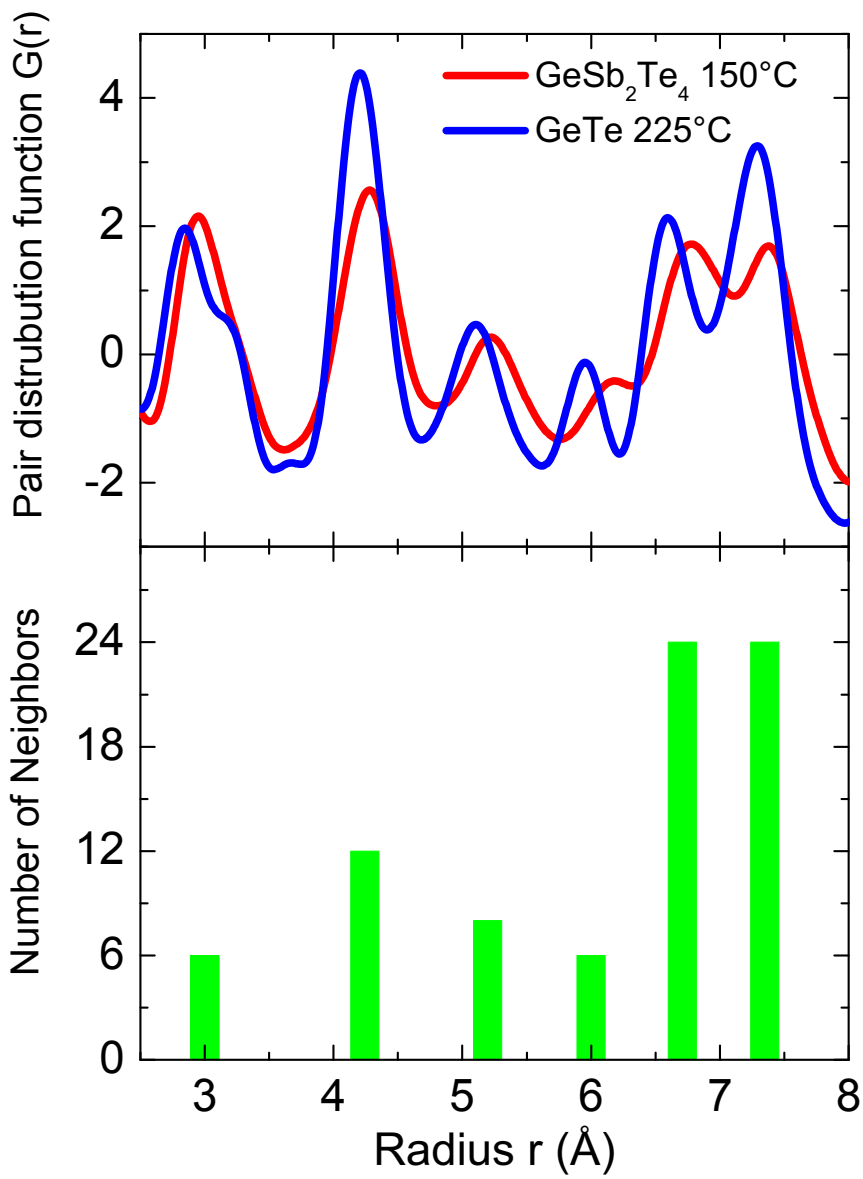

Figure B.2.: Comparison of the Neutron PDF data with the number of neighbors. Plotted are the Neutron DPF data of GeTe and $GeSb_2Te_4$, top part, and the calculated number of neighbors around an atom, assuming an perfect NaCl structure with a lattice constant of 6 Å. The comparison shows the nice agreement of the peak heights in the PDF data, supporting the validity of the NaCl like model.

Bibliography

[1] Armbrust, M., Fox, A., Griffith, R., Joseph, A. D., Katz, R., Konwinski, A., Lee, G., Patterson, D., Rabkin, A., Stoica, I. & Zaharia, M. A view of cloud computing. *Commun. ACM* **53**, 50–58 (2010). ISSN 0001-0782. doi:http://doi.acm.org/10.1145/1721654.1721672. URL `http://dx.doi.org/10.1145/1721654.1721672`.

[2] Wuttig, M. & Yamada, N. Phase-change materials for rewriteable data storage. *Nature Materials* **6** (11), 824–832 (2007). URL `http://dx.doi.org/10.1038/nmat2009`.

[3] Siegrist, T., Merkelbach, P. & Wuttig, M. Phase Change Materials: Challenges on the Path to a Universal Storage Device. *Annual Review of Condensed Matter Physics* **3** (2012).

[4] Panasonic (2011). URL `http://panasonic.co.jp/corp/news/official.data/data.dir/jn110404-1/jn110404-1.html`.

[5] Kolobov, A. V., Fons, P., Frenkel, A. I., Ankudinov, A. L., Tominaga, J. & Uruga, T. Understanding the phase-change mechanism of rewritable optical media. *Nature Materials* **3** (10), 703–708 (2004). URL `http://dx.doi.org/10.1038/nmat1215`.

[6] Welnic, W., Pamungkas, A., Detemple, R., Steimer, C., Blugel, S. & Wuttig, M. Unravelling the interplay of local structure and physical properties in phase-change materials. *Nature Materials* **5** (1), 56–62 (2006). ISSN 1476-1122. URL `http://dx.doi.org/10.1038/nmat1539`.

[7] Wełnic, W., Botti, S., Reining, L. & Wuttig, M. Origin of the Optical Contrast in Phase-Change Materials. *Phys. Rev. Lett.* **98** (23), 236403 (2007). URL `http://dx.doi.org/10.1103/PhysRevLett.98.236403`.

[8] Shportko, K., Kremers, S., Woda, M., Lencer, D., Robertson, J. & Wuttig, M. Resonant bonding in crystalline phase-change materials. *Nature Materials* **7** (8), 653–658 (2008). URL `http://dx.doi.org/10.1038/nmat2226`.

[9] Ashcroft, N. & Mermin, N. *Solid State Physics* (Saunders, Philadelphia, 1976).

[10] Huang, B. & Robertson, J. Bonding origin of optical contrast in phase-change memory materials. *Phys. Rev. B* **81** (8), 081204 (2010). doi:10.1103/PhysRevB.81.081204. URL `http://dx.doi.org/10.1103/PhysRevB.81.081204`.

[11] Yamada, N., Ohno, E., Nishiuchi, K., Akahira, N. & Takao, M. Rapid-phase transitions of GeTe-Sb[sub 2]Te[sub 3] pseudobinary amorphous thin films for an optical disk memory. *Journal of Applied Physics* **69** (5), 2849–2856 (1991). URL `http://dx.doi.org/10.1063/1.348620`.

[12] Lencer, D., Salinga, M., Grabowski, B., Hickel, T., Neugebauer, J. & Wuttig, M. A map for phase-change materials. *Nature Materials* **7** (12), 972–977 (2008). URL `http://dx.doi.org/10.1038/nmat2330`.

[13] Luo, M. & Wuttig, M. The dependence of crystal structure of Te-based phase-change materials on the number of valence electrons. *Adv. Mater.* **16** (5), 439–+ (2004). URL `http://dx.doi.org/10.1002/adma.200306077`.

[14] Lencer, D. *Design Rules, Local Structure and Lattice-Dynamics of Phase-Change Materials for Data Storage Applications.* Ph.D. thesis, RWTH Aachen University (2010).

[15] Littlewood, P. The crystal structure of IV-VI compounds. I. Classification and description. *J. Phys. C: Solid State Phys.* **13** (26), 4855–4873 (1980). ISSN 0022-3719. URL `http://dx.doi.org/10.1088/0022-3719/13/26/009`.

[16] Littlewood, P. The crystal structure of IV-VI compounds. II. A microscopic model for cubic/rhombohedral materials. *J. Phys. C: Solid State Phys.* **13** (26), 4875–4892 (1980). ISSN 0022-3719. URL `http://dx.doi.org/10.1088/0022-3719/13/26/010`.

[17] Matsunaga, T. & Yamada, N. Structural investigation of $GeSb_2Te_4$: A high-speed phase-change material. *Physical Review B* **69** (10), 104111 (2004). URL `http://dx.doi.org/10.1103/PhysRevB.69.104111`.

[18] Da Silva, J. L. F., Walsh, A. & Lee, H. Insights into the structure of the stable and metastable (GeTe)m(Sb2Te3)n compounds. *Physical Review B* **78** (22), 224111 (2008). doi:10.1103/PhysRevB.78.224111. URL http://dx.doi.org/10.1103/PhysRevB.78.224111.

[19] Shamoto, S., Yamada, N., Matsunaga, T., Proffen, T., Richardson, J., Chung, J. & Egami, T. Large displacement of germanium atoms in crystalline Ge2Sb2Te5. *Applied Physics Letters* **86** (8), 081904 (2005). URL http://dx.doi.org/10.1063/1.1861976.

[20] Fons, P., Kolobov, A. V., Krbal, M., Tominaga, J., Andrikopoulos, K. S., Yannopoulos, S. N., Voyiatzis, G. A. & Uruga, T. Phase transition in crystalline GeTe: Pitfalls of averaging effects. *Phys. Rev. B* **82** (15), 155209 (2010). URL http://dx.doi.org/10.1103/PhysRevB.82.155209.

[21] Goldak, J., Barrett, C., Innes, D. & Youdelis, W. Structure of Alpha GeTe. *The Journal of Chemical Physics* **44** (9), 3323–3325 (1966). URL http://dx.doi.org/doi:10.1063/1.1727231.

[22] Nonaka, T., Ohbayashi, G., Toriumi, Y. & Mori, Y. Crystal structure of GeTe and Ge2Sb2Te5 meta-stable phase. *Thin Solid Films* **370** (1-2), 258–261 (2000). URL http://dx.doi.org/10.1016/S0040-6090(99)01090-1.

[23] Rietveld, H. M. A profile refinement method for nuclear and magnetic structures. *Journal of Applied Crystallography* **2** (2), 65–71 (1969). doi:10.1107/S0021889869006558. URL http://dx.doi.org/10.1107/S0021889869006558.

[24] Braun, W., Shayduk, R., Flissikowski, T., Ramsteiner, M., Grahn, H. T., Riechert, H., Fons, P. & Kolobov, A. Epitaxy of Ge–Sb–Te phase-change memory alloys. *Appl. Phys. Lett.* **94** (4), 041902 (2009). ISSN 00036951. doi:DOI:10.1063/1.3072615. URL http://dx.doi.org/doi/10.1063/1.3072615.

[25] Schneider, M. N., Urban, P., Leineweber, A., Döblinger, M. & Oeckler, O. Influence of stress and strain on the kinetic stability and phase transitions of cubic- and pseudocubic Ge-Sb-Te materials. *Phys. Rev. B* **81** (18), 184102 (2010). URL http://dx.doi.org/10.1103/PhysRevB.81.184102.

[26] Wuttig, M., Lüsebrink, D., Wamwangi, D., Welnic, W., Gilleßen, M. & Dronskowski, R. The role of vacancies and local distortions in the design of new phase-change

materials. *Nature Materials* **6** (2), 122–128 (2007). URL http://dx.doi.org/10.1038/nmat1807.

[27] van Eijk, J., Bichara, C., Zaldena, P., Braun, C., Buller, S., Bensch, W. & Wuttig, M. Differences in local order of amorphous and crystalline $GeSb_2Te_4$ probed by X-RAY absorption spectroscopy. *submitted* (2011).

[28] Zalden, P., Bichara, C., van Eijk, J., Braun, C., Bensch, W. & Wuttig, M. Atomic structure of amorphous and crystallized Ge15Sb85. *Journal of Applied Physics* **107** (10), 104312 (2010). ISSN 00218979. URL http://dx.doi.org/doi/10.1063/1.3380667.

[29] Lencer, D., Salinga, M. & Wuttig, M. Design Rules for Phase-Change Materials in Data Storage Applications. *Advanced Materials* **23** (18), 2030–2058 (2011). ISSN 1521-4095. doi:10.1002/adma.201004255. URL http://dx.doi.org/10.1002/adma.201004255.

[30] van Eijk, J. M. *Structural Analysis of Phase-Change Materials using X-Ray Absorption Measurements*. Ph.D. thesis, RWTH Aachen University (2010).

[31] Shamoto, S., Kodama, K., Iikubo, S., Taguchi, T., Yamada, N. & Proffen, T. Local crystal structures of Ge(2)Sb(2)Te5 revealed by the atomic pair distribution function analysis. *Jpn J Appl Phys 1* **45** (11), 8789–8794 (2006). doi:10.1143/JJAP.45.87891.

[32] Shamoto, S., Yamada, N., Matsunaga, T. & Proffen, T. Structural study on optical recording materials Ge2Sb2+xTe5 and GeBi2Te4. *Physica B: Condensed Matter* **385-386** (Part 1), 574 – 577 (2006). URL http://dx.doi.org/10.1016/j.physb.2006.05.363. Proceedings of the Eighth International Conference on Neutron Scattering.

[33] Siegrist, T., Jost, P., Volker, H., Woda, M., Merkelbach, P., Schlockermann, C. & Wuttig, M. Disorder-induced localization in crystalline phase-change materials. *Nat Mater* **10** (3), 202–208 (2011). URL http://dx.doi.org/10.1038/NMAT2934.

[34] Bednorz, J. G. & Müller, K. A. Possible high T_C superconductivity in the Ba-La-Cu-O system. *Zeitschrift für Physik B Condensed Matter* **64**, 189–193 (1986). ISSN 0722-3277. URL http://dx.doi.org/10.1007/BF01303701. 10.1007/BF01303701.

[35] Klitzing, K. v., Dorda, G. & Pepper, M. New Method for High-Accuracy Determination of the Fine-Structure Constant Based on Quantized Hall Resistance. *Phys. Rev. Lett.* **45** (6), 494–497 (1980). URL http://dx.doi.org/10.1103/PhysRevLett.45.494.

[36] Kittel, C. *Einfürung in die Festkörperphysik* (R. Oldenburg, 1999), 12. edition.

[37] Ioffe, A. F. & Regel, A. R. *Progress in Semiconductors*, volume 4 (Heywood, 1960).

[38] Overhof, H. & Thomas, P. *Electronic Transport in Hydrogenated Amorphous Semiconductors* (Springer, 1989).

[39] Gunnarsson, O., Calandra, M. & Han, J. E. Colloquium: Saturation of electrical resistivity. *Rev. Mod. Phys.* **75** (4), 1085–1099 (2003). URL `http://dx.doi.org/10.1103/RevModPhys.75.1085`.

[40] Edwards, P. P., Ramakrishnan, T. V. & Rao, C. N. R. The Metal-Nonmetal Transition: A Global Perspective. *The Journal of Physical Chemistry* **99** (15), 5228–5239 (1995). URL `http://dx.doi.org/10.1021/j100015a002`.

[41] Bongers, P. Anisotropy of the electrical conductivity of VO2 single crystals. *Solid State Communications* **3** (9), 275–277 (1965). URL `http://dx.doi.org/10.1016/0038-1098(65)90032-3`.

[42] Rosevear, W. H. & Paul, W. Hall Effect in V*O*2 near the Semiconductor-to-Metal Transition. *Phys. Rev. B* **7** (5), 2109–2111 (1973). URL `http://dx.doi.org10.1103/PhysRevB.7.2109`.

[43] Mott, N. Review Lecture: Metal-Insulator Transitions. *Proceedings of the Royal Society of London. A. Mathematical and Physical Sciences* **382** (1782), 1–24 (1982). URL `http://dx.doi.org/10.1098/rspa.1982.0086`.

[44] Anderson, P. W. Absence of Diffusion in Certain Random Lattices. *Phys. Rev.* **109** (5), 1492–1505 (1958). URL `http://dx.doi.org/10.1103/PhysRev.109.1492`.

[45] Alexander, M. N. & Holcomb, D. F. Semiconductor-to-Metal Transition in N-Type Group 4 Semiconductors. *Rev. Mod. Phys.* **4** (4), 815–829 (1968). URL `http://dx.doi.org/10.1103/RevModPhys.40.815`.

[46] Gaymann, A., Geserich, H. P. & vonLohneysen, H. Temperature dependence of the far-infrared reflectance spectra of Si2:P near the metal-insulator transition. *Phys. Rev. B* **52** (23), 16486–16493 (1995). URL `http://dx.doi.org/10.1103/PhysRevB.41.5152`.

[47] Rosenbaum, T. F., Thomas, G. A. & Paalanen, M. A. Critical-Behavior of Si:P at the Metal-Insulator-Transition. *Phys. Rev. Lett.* **72** (13), 2121–2121 (1994). URL http://dx.doi.org/10.1103/PhysRevLett.72.2121.

[48] Belitz, D. & Kirkpatrick, T. R. The Anderson-Mott Transition. *Rev. Mod. Phys.* **66** (2), 261–390 (1994). URL http://dx.doi.org/10.1103/RevModPhys.66.261.

[49] Lee, P. A. & Ramakrishnan, T. V. Disordered Electronic Systems. *Rev. Mod. Phys.* **57** (2), 287–337 (1985). URL http://dx.doi.org/10.1103/RevModPhys.57.287.

[50] Baranovski, S. (Editor). *Charge Transport in Disordered Solids with Application in Electronics* (John Wiley, 2006). URL http://dx.doi.org/10.1002/0470095067.

[51] Abrahams, E., Kravchenko, S. V. & Sarachik, M. P. Metallic behavior and related phenomena in two dimensions. *Rev. Mod. Phys.* **73** (2), 251–266 (2001). URL http://dx.doi.org/10.1103/RevModPhys.73.251.

[52] Mott, N. F. The transition to the metallic state. *Philosophical Magazine* **3** (30), 287–309 (1961). URL http:/dx.doi.org/10.1080/14786436108243318.

[53] Woda, M. *Electrical transport in crystalline phase change materials.* Ph.D. thesis, RWTH Aachen University (2010).

[54] van der Pauw, L. A method of measuring specific resistivity and Hall effect of discs of arbitrary shape. *Philips Res. Rep* **13** (1), 1–9 (1958).

[55] Volker, H. Ph.D. thesis, RWTH Aachen University (2012).

[56] Mott, N. Conduction in glasses containing transition metal ions. *Journal of Non-Crystalline Solids* **1** (1), 1 – 17 (1968). URL http://dx.doi.org/10.1016/0022-3093(68)90002-1.

[57] Shklovskii, B. I. & Efros, A. L. *Electronic Properties of Doped Semiconductors* (Springer, 1984).

[58] Mott, N. F. Conduction in non-crystalline materials. *Philosophical Magazine* **19** (160), 835–852 (1969). URL http://dx.doi.org/10.1080/14786436908216338.

[59] Collaboration: Authors and editors of the volumes III/17G-41D: VO2: resistivity, conductivity, photoconductivity. Madelung, O., Rössler, U., Schulz, M. (ed.). SpringerMaterials - The Landolt-Börnstein Database (http://www.springermaterials.com). DOI: 10.1007/10681735_334 ().

[60] Collaboration: Authors and editors of the volumes III/17G-41D: VO2: Hall mobility. Madelung, O., Rössler, U., Schulz, M. (ed.). SpringerMaterials - The Landolt-Börnstein Database (http://www.springermaterials.com). DOI: 10.1007/10681735_336 ().

[61] Als-Nielsen, J. & McMorrow, D. *Elements of Modern X-Ray Physics* (Wiley, 2001).

[62] Stern, E. A., Bouldin, C. E., von Roedern, B. & Azoulay, J. Incipient amorphous-to-crystalline transition in Ge. *Phys. Rev. B* **27** (10), 6557–6560 (1983). URL `http://dx.doi.org/10.1103/PhysRevB.27.6557`.

[63] Laptyeva, G. *Quantitative TEM analysis of crystalline and amorphous GeTe-based chalcogenides*. Ph.D. thesis, RWTH Aachen University (2009).

[64] Prokhorov, E., Trapaga, G. & González-Hernández, J. Structural and electrical properties of Ge[sub 1]Sb[sub 2]Te[sub 4] face centered cubic phase. *Journal of Applied Physics* **104** (10), 103712 (2008). URL `http://dx.doi.org/10.1063/1.3021462`.

[65] Warren, B. *X-Ray Diffraction* (Addison-Wesley Publishing Co., 1969).

[66] Sheng, P., Abeles, B. & Arie, Y. Hopping Conductivity in Granular Metals. *Phys. Rev. Lett.* **31** (1), 44–47 (1973). URL `http://dx.doi.org/10.1103/PhysRevLett.31.44`.

[67] Kremers, S. *Optische Eigenschaften von Phasenwechselmaterialien*. Ph.D. thesis, RWTH Aachen University (2009).

[68] Lee, B.-S., Abelson, J. R., Bishop, S. G., Kang, D.-H., ki Cheong, B. & Kim, K.-B. Investigation of the optical and electronic properties of Ge2Sb2Te5 phase change material in its amorphous, cubic, and hexagonal phases. *Journal of Applied Physics* **97** (9), 093509 (2005). ISSN 00218979. URL `http://dx.doi.org/10.1063/1.1884248`.

[69] Tung, Y. W. & Cohen, M. L. Relativistic Band Structure and Electronic Properties of SnTe, GeTe, and PbTe. *Phys. Rev.* **180** (3), 823–826 (1969). URL `http://dx.doi.org/10.1103/PhysRev.180.823`.

[70] Bahl, S. K. & Chopra, K. L. Amorphous versus Crystalline GeTe Films. III. Electrical Properties and Band Structure. *Journal of Applied Physics* **41** (5), 2196–2212 (1970). URL http://dx.doi.org/10.1063/1.1659189.

[71] Martinez, G., Schlüter, M. & Cohen, M. L. Electronic structure of PbSe and PbTe. I. Band structures, densities of states, and effective masses. *Phys. Rev. B* **11** (2), 651–659 (1975). URL http://dx.doi.org/10.1103/PhysRevB.11.651.

[72] Bahl, S. K. & Chopra, K. L. Amorphous Versus Crystalline GeTe Films. II. Optical Properties. *Journal of Applied Physics* **40** (12), 4940–4947 (1969). URL http://dx.doi.org/10.1063/1.1657318.

[73] Mott, N. F. Electrons in disordered structures. *Advances in Physics* **16**, 49–144 (1967). URL http://dx.doi.org/10.1080/00018738500101771.

[74] Lencer, D. private communication (2010).

[75] Edwards, P. & Sienko, M. Universality aspects of the metal-nonmetal transition in condensed media. *Physical Review B* **17** (6), 2575–2581 (1978). URL http://dx.doi.org/10.1103/PhysRevB.17.2575.

[76] Egami, T. & Billinge, S. J. L. *Underneath the Bragg Peaks: Structural Analysis of Complex Materials* (Elsevier Science, Oxford, 2004).

[77] Fischer, H., Barnes, A. & Salmon, P. Neutron and x-ray diffraction studies of liquids and glasses. *Rep Prog Phys* **69** (1), 233–299 (2006). URL http://dx.doi.org/10.1088/0034-4885/69/1/R05.

[78] Squires, G. L. *Introduction to the theory of thermal neutron scattering* (Cambridge University Press, 1978).

[79] Sears, V. F. Neutron scattering lengths and cross sections. *Neutron News* **3** (26) (1992). URL http://www.ncnr.nist.gov/resources/n-lengths/.

[80] Chieux, P. Introduction to accurate structure factor measurements of disordered materials by neutron scattering. *Journal of Molecular Structure* **296** (3), 177 – 198 (1993). ISSN 0022-2860. doi:DOI:10.1016/0022-2860(93)80133-G. URL http://dx.doi.org/10.1016/0022-2860(93)80133-G.

[81] http://www.ill.eu/instruments-support/instruments-groups/instruments/d4/ (2011).

[82] Farrow, C., Juhas, P., Liu, J., Bryndin, D., Božin, E., Bloch, J., Proffen, T. & Billinge, S. PDFfit2 and PDFgui: computer programs for studying nanostructure in crystals. *Journal of Physics: Condensed Matter* **19**, 335219 (2007). doi:10.1088/0953-8984/19/33/335219. URL `http://dx.doi.org/10.1088/0953-8984/19/33/335219`.

[83] Matsunaga, T. Structural and electrical properties of optical phase-change materials GeTe and Ge8Sb2Te11. *SPring-8 Res Front 2005* (2006). URL `http://sciencelinks.jp/j-east/article/200703/000020070306A0968083.php`.

[84] Liu, X. Q., Li, X. B., Zhang, L., Cheng, Y. Q., Yan, Z. G., Xu, M., Han, X. D., Zhang, S. B., Zhang, Z. & Ma, E. New Structural Picture of the $Ge_2Sb_2Te_5$ Phase-Change Alloy. *Phys. Rev. Lett.* **106** (2), 025501 (2011). URL `http://dx.doi.org/10.1103/PhysRevLett.106.025501`.

[85] Martin, R. M. *Electronic Structure: Basic Theory and Practical Methods.* (Cambridge University Press, 2005). URL `http://dx.doi.org/10.1109/MCD.2006.1708382`.

[86] P., Z. . private communication (2011).

[87] Zhang, W. private communication (2011).

[88] Proffen, T. & Billinge, S. J. L. *PDFFIT*, a program for full profile structural refinement of the atomic pair distribution function. *Journal of Applied Crystallography* **32** (3), 572–575 (1999). URL `http://dx.doi.org/10.1107/S0021889899003532`.

[89] Wuttig, M. Phase-change materials: towards a universal memory? *Nature Materials* **4** (4), 347–52 (2005). URL `http://dx.doi.org/10.1038/nmat1359`.

[90] Pirovano, A., Redaelli, A., Pellizzer, F., Ottogalli, F., Tosi, M., Ielmini, D., Lacaita, A. & Bez, R. Reliability study of phase-change nonvolatile memories. *Device and Materials Reliability, IEEE Transactions on* **4** (3), 422 – 427 (2004). ISSN 1530-4388. URL `http://dx.doi.org/10.1109/TDMR.2004.836724`.

[91] Lankhorst, M. H. R., Ketelaars, B. W. S. M. M. & Wolters, R. A. M. Low-cost and nanoscale non-volatile memory concept for future silicon chips. *Nature Materials* **4** (4), 347–352 (2005). URL `http://dx.doi.org/10.1038/nmat1350`.

[92] Nirschl, T., Philipp, J., Happ, T. & Burr, G. Write Strategies for 2 and 4-bit Multi-Level Phase-Change Memory. *Electron Devices Meeting* (2007). URL http://ieeexplore.ieee.org/xpls/abs_all.jsp?arnumber=4418973.

[93] Lai, S. & Lowrey, T. OUM-A 180 nm Non-Volatile Memory Cell Element Technology for Stand Alone and Embedded Applications. *Electron Devices Meeting* (2001). URL http://dx.doi.org/10.1109/IEDM.2001.979636.

[94] Ovshinsky, S. R. Reversible Electrical Switching Phenomena in Disordered Structures. *Phys. Rev. Lett.* **21** (20), 1450–1453 (1968). URL http://dx.doi.org/10.1103/PhysRevLett.21.1450.

[95] Adler, D., Henisch, H. K. & Mott, S. N. The mechanism of threshold switching in amorphous alloys. *Rev. Mod. Phys.* **50** (2), 209–220 (1978). URL http://dx.doi.org/10.1103/RevModPhys.50.209.

[96] Adler, D., Shur, M. S., Silver, M. & Ovshinsky, S. R. Threshold switching in chalcogenide-glass thin films. *Journal Of Applied Physics* **51** (6), 3289–3309 (1980). URL http://dx.doi.org/10.1063/1.328036.

[97] Emin, D. Current-driven threshold switching of a small polaron semiconductor to a metastable conductor. *Phys. Rev. B* **74** (3), 035206 (2006). URL hrrp://dx.doi.org/10.1103/PhysRevB.74.035206.

[98] Ielmini, D. & Zhang, Y. G. Analytical model for subthreshold conduction and threshold switching in chalcogenide-based memory devices. *Journal Of Applied Physics* **102** (5), 054517 (2007). URL http://dx.doi.org/10.1063/1.2773688.

[99] Krebs, D., Raoux, S., Rettner, C. T., Burr, G. W., Salinga, M. & Wuttig, M. Threshold field of phase change memory materials measured using phase change bridge devices. *Applied Physics Letters* **95** (8), 082101 (2009). URL http://dx.doi.org/10.1063/1.3210792.

[100] Ielmini, D., Lacaita, A. L. & Mantegazza, D. Recovery and Drift Dynamics of Resistance and Threshold Voltages in Phase-Change Memories. *Electron Devices, IEEE Transactions on* **54** (2), 308 –315 (2007). ISSN 0018-9383. URL http://dx.doi.org/10.1109/TED.2006.888752.

[101] Karpov, I. V., Mitra, M., Kau, D., Spadini, G., Kryukov, Y. A. & Karpov, V. G. Fundamental drift of parameters in chalcogenide phase change memory. *Journal of Applied Physics* **102** (12), 124503 (2007). URL http://dx.doi.org/10.1063/1.2825650.

[102] Pirovano, A., Lacaita, A., Pellizzer, F., Kostylev, S., Benvenuti, A. & Bez, R. Low-field amorphous state resistance and threshold voltage drift in chalcogenide materials. *Electron Devices, IEEE Transactions on* **51** (5), 714 – 719 (2004). ISSN 0018-9383. URL http://dx.doi.org/10.1109/TED.2004.825805.

[103] Bruns, G. *Electronic switching in phase-change materials.* Ph.D. thesis, RWTH Aachen University (2011).

[104] Schlockermann, C. Ph.D. thesis, RWTH Aachen University (2011).

[105] Bruns, G., Merkelbach, P., Schlockermann, C., Salinga, M., Wuttig, M., Happ, T. D., Philipp, J. B. & Kund, M. Nanosecond switching in GeTe phase change memory cells. *Applied Physics Letters* **95** (4), 043108 (2009). URL http://dx.doi.org/10.1063/1.3191670.

[106] Chen, M., Rubin, K. & Barton, R. Compound materials for reversible, phase-change optical data storage. *Applied Physics Letters* **49** (9), 502–504 (1986). URL http://dx.doi.org/10.1063/1.97617.

[107] Coombs, J. H., Jongenelis, A. P. J. M., van Es-Spiekman, W. & Jacobs, B. A. J. Laser induced crystallization phenomena in GeTe based alloys. II. Composition dependence of nucleation and growth. *Journal of Applied Physics* **78** (8), 4918–4928 (1995). URL http://dx.doi.org/10.1063/1.359780.

[108] Wang, W. J., Shi, L. P., Zhao, R., Lim, K. G., Lee, H. K., Chong, T. C. & Wu, Y. H. Fast phase transitions induced by picosecond electrical pulses on phase change memory cells. *Applied Physics Letters* **93** (4), 043121 (2008). URL http://dx.doi.org/10.1063/1.2963196.

[109] Kalb, J., Spaepen, F. & Wuttig, M. Kinetics of crystal nucleation in undercooled droplets of Sb- and Te-based alloys used for phase change recording. *Journal of Applied Physics* **98** (5), 054910 (2005). URL http://dx.doi.org/10.1063/1.2037870.

[110] Boniardi, M., Redaelli, A., Pirovano, A., Tortorelli, I., Ielmini, D. & Pellizzer, F. A physics-based model of electrical conduction decrease with time in amorphous

Ge[sub 2]Sb[sub 2]Te[sub 5]. *Journal of Applied Physics* **105** (8), 084506 (2009). URL http://dx.doi.org/10.1063/1.3109063.

[111] Jost, P. Ph.D. thesis, RWTH Aachen University (2012).

[112] König, A. Antimony-based alloys: Investigating characteristic properties of phase change materials. Diplomarbeit, RWTH Aachen University (2010).

Acknowledgements

Während meiner Dissertation haben mir viele Menschen stets zur Seite gestanden und mich unterstützt. Dafür möchte ich an dieser Stelle ganz herzlich danken.
Zunächst bedanke ich mich bei Prof. Dr. Matthias Wuttig, der es mir ermöglicht hat an diesem spannenden Thema zu arbeiten. Seine Fähigkeit Menschen für neue, spannende Felder der Physik zu begeistern hat mich sehr motiviert.
Bei Prof. Dr. Theo Siegrist möchte ich mich sowohl für die fruchtbaren wissenschaftlichen Diskussionen im Bereich der Kristallstruktur und Röntgenmessungen bedanken als auch für die Übernahme des Koreferats.
Unseren Partnern des Qimonda-Projekts danke ich sehr für die gemeinsame spannende Arbeit. Die wöchentlichen Telefonkonferenzen mit Michael Kund, Jan Boris Philipp und Thomas Happ waren ein gutes Beispiel für eine beide Seiten bereichernde Industriekooperation und sorgten für eine stetig steigende Lernkurve.
Auch die Arbeit am Jules-et-Jim Projekt mit dem Anderson-Team, war außerordentlich bereichernd für mich. Für die professionelle Zusammenarbeit möchte ich vor allem Peter Jost, Hanno Volker, Michael Woda und Stephan Kremers ganz herzlich danken.
Special thanks to Henry Fischer for the excellent support during the beamtimes at the ILL in Grenoble. Also I would like to thank the other participants of the experiments Marc Johnson, Céline Otjacques, Wojtek Welnic, Peter Zalden and Gunnar Bruns for the inspiring working atmosphere.
Ich danke Dominic Lencer und ganz besonders Peter Jost für viele anregende Gespräche rund um Struktur und Transport in ungeordneten Systemen.
Speziell meine Lithographische Arbeit im Reinraum des II. Physkalischen Instituts wäre ohne die fachkundige Beratung durch Nicolas Müsgens nicht möglich gewesen.
Bedanken möchte ich mich ferner bei meinen Freunden und Kollegen am 1. Physikalischen Institut für die stets angenehme Arbeitsatmosphäre. Besonders meinen Kollegen Gunnar

Bruns, Daniel Wamwangi und Peter Zalden danke ich für schöne Jahre gemeinsam im Büro. Sie haben mich über drei Jahre durch die Höhen und Tiefen meiner Arbeit begleitet. Viele fruchtbare Diskussionen haben meine Arbeit bereichert.
Frau Elbert, Sarah Schlenter und Günther Kluck-Ehlen danke ich für die lückenlose Unterstützung rund um alle bürokratischen Hürden des Alltags an der Hochschule. Ebenso möchte ich mich bei Oliver Lehmann für den Support rund um die PC-Infrastruktur, und Stephan Hermes sowie Sebastian Mohrhenn für die technische Unterstützung im Laboralltag bedanken.
Zu guter letzt möchte ich mich auch für das Korrekturlesen dieser Arbeit bei meiner Tante Dr. Anna Maria Ertel, sowie Peter Jost, Peter Zalden, Gunnar Bruns und Philip Schulz bedanken. Mein ganz besonderer Dank gilt meiner Frau Marie, die mich mit ihrer Fürsorge durch alle Höhen und Tiefen meiner Arbeit unterstützt und begleitet hat.

Lebenslauf

Persönliche Daten

Philipp Johannes Merkelbach
Geb. am 09. September 1981 in Köln
verheiratet, deutsch

Studium und Ausbildung

08/1988–07/1992	Gemeinschaftsgrundschule Wittenbergstraße, Bergisch Gladbach
08/1992–06/2001	Otto Hahn Gymnasium
06/2001	Abitur
08/2001–05/2002	Zivildienst im Caritasverband für den Rheinisch-Bergischen Kreis
10/2002–01/2008	Studium der Physik an der RWTH Aachen
09/2004	Vordiplom Physik an der RWTH Aachen
11/2006–12/2007	Diplomarbeit am I. Physikalischen Institut IA bei Prof. Dr. M. Wuttig
01/2008	Diplom in Physik an der RWTH Aachen, Note: sehr gut Schwerpunkt: Festkörperphysik, Nebenfach: Geophysik
02/2008-08/2011	Wissenschaftlicher Mitarbeiter, 1. Physikalisches Institut (IA), RWTH Aachen

Wissenschaftliche Publikationen

Nanosecond switching in GeTe phase change memory cells
G. Bruns, P. Merkelbach, C. Schlockermann, M. Salinga, M. Wuttig, T. D. Happ, J. B. Philipp and M. Kund
APPLIED PHYSICS LETTERS **96** (4), 043108 (2009) DOI: 10.1063/1.3191670

Scanning tunneling microscopy and spectroscopy of the phase change alloy $GeSb_2Te_4$
D. Subramaniam, C. Pauly, M. Liebmann, M. Woda, P. Rausch, P. Merkelbach, M. Wuttig, and M. Morgenstern
APPLIED PHYSICS LETTERS **95** (10), 103110 (2009) DOI: 10.1063/1.3211991

Disorder-induced localization in crystalline phase-change materials
T. Siegrist, P. Jost, H. Volker, M. Woda, P. Merkelbach, C. Schlockermann and M. Wuttig
NATURE MATERIALS **10**, 202-208 (2011) DOI: 10.1038/NMAT2934

Thin Films of Ge–Sb–Te-Based Phase Change Materials: Microstructure and in Situ Transformation
J. Tomforde, W. Bensch, L. Kienle, V. Duppel, P. Merkelbach and M. Wuttig
CHEMESTRY OF MATERIALS, (2011) DOI: 10.1021/cm200835a

Phase Change Materials: Challenges on the Path to a Universal Storage Device
T. Siegrist, P. Merkelbach and M. Wuttig
ANNUAL REVIEW OF CONDENSED MATTER PHYSICS
Forthcoming - Volume 3, 2012

Konferenzbeiträge (Auszüge)

Structural Properties of Metastable State of Phase-Change Materials Investigated by Synchrotron Radiation,
P. Merkelbach, M. Wuttig et. al.
DPG FRÜHJAHRSTAGUNG DES ARBEITSKREISES FESTKÖRPERPHYSIK, Poster, Berlin, 2008

Employing advanced characterization tools for the study of phase change materials,
C. Schlockermann, G. Bruns, P. Merkelbach, H. Volker, M. Salinga, M. Wuttig
EUROPEAN\PHASE CHANGE AND OVONICS SYMPOSIUM,
Talk, Aachen, 2009

Phase Change RAM: Non-volatile switching at DRAM speeds,
P. Merkelbach, M. Wuttig et. al.
DPG FRÜHJAHRSTAGUNG DES ARBEITSKREISES FESTKÖRPERPHYSIK,
Poster, Regensburg, 2010

Controlling Charge Transport in Phase Change Materials,
T. Siegrist, M. Woda, S. Kremers, P. Jost, P. Merkelbach, P. Rausch, M. Wuttig
MRS SPRING MEETING,
Talk, San Francisco, 2010

Controlling Charge Transport in Crystalline Phase Change Materials,
M. Wuttig, T. Siegrist, M. Woda, S. Kremers, P. Merkelbach, and P. Jost
EUROPEAN\PHASE CHANGE AND OVONICS SYMPOSIUM,
Talk, Milano, 2010

Aachen, November 30, 2011

Hiermit versichere ich, dass ich die vorliegende Arbeit selbstständig verfasst und nur die angegebenen Quellen und Hilfsmittel benutzt habe.